UNSTEADY AERODYNAMICS OF STATIONARY AND PLUNGING SYMMETRIC AIRFOILS AT LOW REYNOLDS NUMBERS

A THESIS SUBMITTED TO
THE GRADUATE SCHOOL OF NATURAL AND APPLIED SCIENCES
OF
MIDDLE EAST TECHNICAL UNIVERSITY

BY

KIFA PEERZADA

IN PARTIAL FULFILLMENT OF THE REQUIREMENTS
FOR
THE DEGREE OF MASTER OF SCIENCE
IN
AEROSPACE ENGINEERING

JANUARY 2023

Approval of the thesis:

UNSTEADY AERODYNAMICS OF STATIONARY AND PLUNGING AIRFOILS AT LOW REYNOLDS NUMBERS

submitted by **KIFA PEERZADA** in partial fulfillment of the requirements for the degree of **Master of Science** i**n Aerospace Engineering, Middle East Technical University** by,

Prof. Dr. Halil Kalıpçılar
Dean, Graduate School of **Natural and Applied Sciences** _____

Prof. Dr**.** Serkan Özgen
Head of the Department, **Aerospace Engineering** _____

Prof. Dr. Dilek Funda Kurtuluş
Supervisor, **Aerospace Engineering, METU** _____

Examining Committee Members:

Assoc. Prof. Dr. Nilay Sezer Uzol
Aerospace Engineering, METU _____

Prof. Dr. Dilek Funda Kurtuluş
Supervisor, Aerospace Engineering, METU _____

Assist. Prof. Dr. Özge Başkan Perçin
Aerospace Engineering, METU _____

Assoc. Prof. Dr. Ali Emre Turgut
Mechanical Engineering, METU _____

Assist. Prof. Dr. Kutluk Bilge Arıkan
Mechanical Engineering, TED University _____

Date: 10.01.2023

I hereby declare that all information in this document has been obtained and presented in accordance with academic rules and ethical conduct. I also declare that, as required by these rules and conduct, I have fully cited and referenced all material and results that are not original to this work.

Name, Last name: Kifa Peerzada

Signature:

ABSTRACT

UNSTEADY AERODYNAMICS OF PLUNGING AND STATIONARY SYMMETRIC AIRFOILS AT LOW REYNOLDS NUMBERS

Peerzada, Kifa
Master of Science, Aerospace Engineering
Supervisor: Prof. Dr. Dilek Funda Kurtuluş

January 2023, 110 pages

The unsteady behavior of the flow around a symmetric NACA 0014 airfoil is analyzed taking into consideration an oscillating motion in a sinusoidal pure-plunge mode as well as the stationary condition. Numerical simulations are performed by incorporating the two-dimensional unsteady, incompressible Navier-Stokes equation at Reynolds number (Re) = 10^4. The flow is visualized at the following two angle of attacks: 0° and 4°. The flow is assumed to be laminar at this Reynolds number. Flow properties such as: flow pattern, unsteady vortex shedding and aerodynamic coefficients are observed for the following cases: plunging airfoil and stationary airfoil. The impact of thickness to chord ratio (t/c), angle of attack (α), Reynolds number (*Re)* and effect of reduced frequency *(k)* is examined and discussed in detail. Additionally, the flow behavior is also analyzed for NACA 0012 at the same flow parameters for Reynolds numbers (*Re*) from 10^3 to 10^4. Using the literature data as a reference, a comparison of the obtained results has been performed to ensure that the results are valid.

Keywords: Unsteady aerodynamics, micro air vehicles, low Reynolds number, numerical simulation, plunge motion.

ÖZ

DÜŞÜK REYNOLDS SAYILARINDA SABİT VE DALMA HAREKETİ YAPAN SİMETRİK KANAT PROFİLLERİNİN ZAMANA BAĞLI AERODİNAMİĞİ

Peerzada, Kifa
Yüksek Lisans, Havacılık ve Uzay Mühendisliği
Tez Yöneticisi: Prof. Dr. Dilek Funda Kurtuluş

Ocak 2023, 110 sayfa

Simetrik kanat profili NACA 0014 etrafındaki akışın zamana bağlı davranışı, sabit kanat durumunun yanı sıra sinüzoidal saf dalma modunda salınım hareketi dikkate alınarak da analiz edilmiştir. Reynolds sayısı Re = 10000'de iki boyutlu zamana bağlı sıkıştırılamaz Navier-Stokes denklemleri kullanılarak sayısal simülasyonlar gerçekleştirilmiştir. Akış 0° ve 4° hücum açılarında sunulmuştur. Bu Reynolds sayısında akış laminer olarak kabul edilmiştir. Sabit kanat profili ve saf dalma hareketinde akış modeli, zamana bağlı girdap konturları ve aerodinamik katsayılar gibi akış özellikleri gözlemlenmiştir. Hem saf dalma durumu hem de sabit kanat için hücum açısının etkisi ayrıntılı olarak incelenmiş ve tartışılmıştır. Ek olarak, Re=1000’ den 10000’e kadar için aynı akış parametrelerinde NACA 0012 için akış davranışı da analiz edilmiştir. Sonuçlar ayrıca doğrulama amaçlı literatürde mevcut olan veriler ile de karşılaştırılmıştır.

Anahtar Kelimeler: Mikro hava araçları, kararsız aerodinamik, düşük Reynolds sayısı, sayısal simülasyon, dalma hareketi

To my family

ACKNOWLEDGMENTS

I wish to express my deepest gratitude to my supervisor Prof. Dr. Dilek Funda Kurtulus for her guidance, advice, criticism, encouragement, and insight throughout the course of this research.

I would like to extend my sincere gratitude to my father Shahid Mehmood Peerzada, my mother Arjumand Tahseen Naqueeb, and my brother Naveed Peerzada for their constant love, support and encouragement throughout this researching and drafting process.

I would also like to thank my other family members and friends for their support and encouragement.

TABLE OF CONTENTS

LIST OF TABLES

TABLES

LIST OF FIGURES

FIGURES

LIST OF SYMBOLS

SYMBOLS

Re = Reynolds Number

α = Angle of attack (geometric)

Φ = Plunge phase angle, deg

H = Plunge amplitude

k = Reduced frequency ωc/U_{inf}

C = Airfoil chord

f = Flapping frequency, Hz

X = Distance in axial direction

Y = Distance in lateral direction

t^* = Non-dimensional time

UDF = User defined function

CHAPTER 1

INTRODUCTION

Nature has always fascinated and inspired humans throughout the history, as proved time and again by the history of humankind. The magnificent nature all around compelled humans to contemplate over their surroundings and developed a strong desire to understand the laws of nature. Humans have been taking their inspiration from nature in practically every sphere of life.

Similarly, the desire to fly like birds and insects paved the way for developing something similar which in turn led to the study and creation of modern-day micro air vehicles, aircrafts, and helicopters.

1.1 Background

Lift and thrust are generated by flapping the wings of birds and insects. Fish also move by flapping their tails. With their wings and fins, these species execute several kinematic movements of plunging (heaving), pitching, banking, and stroke-reversals ([1], [2]).

Since they operate at a low speed and have a small scale of length, most insects fly at Reynolds numbers of 10^3-10^4 and most birds at Reynolds numbers of 10^4-10^5 [1]. The Reynolds number for species like hummingbirds is Re = O (10^4), while in case of small insects, like fruit flies or honeybees, Re = O (10^2 – 10^3) [3].

It has been a longstanding tradition in engineering to look to nature for inspiration with the intention of creating bio-inspired miniature machines. Research in recent years has primarily been devoted to assessing the kinematics, physical parameters, and flow behaviour of flapping motion observed in nature (such as insects flying and fish swimming) at low Reynolds number (Re) regimes as a means to develop autonomous vehicles based on bio-inspired principles ([4] - [6]).

A flapping wing micro air vehicle (MAV), which mimics the flight of birds and insects, has a favourable design for low Reynolds number regimes in comparison to a fixed wing. In last few decades, it has become increasingly imperative to understand the unsteady phenomena associated with low Reynolds number flows. Its purpose lies in the development of fundamentally improved methods for designing and controlling MAVs ([7], [8]).

At low Reynolds numbers and steady external conditions, flapping airfoils have an unsteady behaviour that may help us better understand the vortex shedding phenomenon they experience during this flight regime. In most cases, these flapping motions are modelled analytically using quasi-steady approaches [9].

1.2 Research on flapping wings: A brief history

It is believed that Knoller [10] and Betz [11] provided the first elementary justification for thrust generated because of flapping wings. Considering that most natural species perform this motion in combination with plunging and pitching, it has been suggested that flapping is an amalgamation of plunging and pitching by Jones et al. [12]. The unsteady aerodynamic forces produced by wing motion, whether it takes place independently or in combination, result in oscillatory lift and thrust. When the flaps generate clockwise rotating vortices (von-Karman vortex-street) or counter-clockwise rotating vortices (reverse von-Karman vortex-street) in the wake, the drag or thrust force generated as a result [13].

In his wind tunnel experiment, Katzmayr [14] observed that an oscillating air flow produced thrust on the wing mounted in that flow. As a result of his work, Birnbaum [15] developed the first theory that successfully described the lift and thrust generated by flapping wings. Kuessner and Theodorsen [16] succeeded in eliminating Birnbaum's restriction on low-frequency oscillations in the following decades. In subsequent years, this Theodorsen-Kuessner oscillatory thin-airfoil approach emerged as a reliable method for analysing problems related to airfoil flutter. As a result, Garrick [17] analysed flapping wings using Theodorsen's theory, a theory that still serves as a classic reference work today.

The literature is very scarce with regard to analyses of unsteady flows around airfoils at low Reynolds numbers of order 10^3. These Re numbers result in highly nonlinear flows characterized by complex viscous phenomena. Numerous numerical simulations have been conducted by researchers under steady external conditions at Re = O (10^2–10^4), mostly at low angles of attack.

Kunz and Kroo [18] from Stanford University used the artificial compressibility method for their two-dimensional incompressible Navier-Stokes solver INS2D. An analysis of angles of attack less than 10° was conducted, evaluating Reynolds numbers between 1000 and 12000 based on thickness (between 2% and 10%), and various NACA profiles.

For Reynolds numbers between 400 and 6000 at small angles of attack, an artificially compressible pseudo-time integration method was used by Mateescu and Abdo [19] to solve Navier-Stokes equations. They achieved quite similar results to Kunz and Kroo [18].

At present, some literature also emphasizes perching maneuvers at low Reynolds numbers. Like the pitch-up problem, the angle of attack in the perching maneuver varies over a wide range. A constant pitch rate flow around a flat plate and an ellipse with a 10% thickness was studied by Ol et al. [20] at a constant pitch rate of 100 and 1000 for amplitudes of 0° to 40°. Understanding flow physics at steady conditions

will lead to an improved understanding of micro air vehicle applications, such as perching, gust response, maneuvering flight, and flapping wings. This will facilitate the control of the MAVs and allow the system to be modelled.

The formation of vortices and flow separation need to be understood comprehensively. Flows with low Reynolds numbers will separate at a mild adverse pressure gradient due to laminar flow. Furthermore, at wake of an airfoil with low Reynolds numbers, structural vibrations and noise generation are also responsible for the formation of coherent structures. A low Reynolds number airfoil has become a key component in the development of small wind turbines in recent years due to its aerodynamic properties [21].

Navier-Stokes calculations, made possible by computers several decades ago, have also been used to analyse flapping airfoil aerodynamics, allowing for the computation of significant viscous properties which were demonstrated by Tuncer and Platzer [22], Tuncer et al. [23], Tuncer and Platzer [24], and Isogai et al. [25].

Aerodynamics of MAVs and small UAVs are largely governed by Reynolds number effects. Lifting bodies perform worse as their Reynolds number decreases. It is necessary to understand the aerodynamics of low-speed airfoils precisely to develop flapping-wing micro air vehicles. It must be noted that the lift, drag, and pitching moment parameters of the NACA 0012 airfoil are examined using ANSYS Fluent at low Reynolds numbers of 1000. This is at 0° and 90° angles of attack ([26], [27]).

1.3 Motivation

The renewed interest in MAVs has sparked a new need for data collection and gathering information. This will enable us to advance in the field of MAVs in a more comprehensive manner. FWMAVs can hover and glide using the same system. Their Agile design provides high maneuverability. In addition, the greater plunge amplitude increases lift and also boosts thrust, as a result of the rise in plunge

amplitude. In view of the limited amount of experimental information available for NACA 0014 plunging airfoil, this study aims to provide flow visualization and flow characteristics near and downstream of plunging and stationary airfoils to improve our understanding of flow near and downstream of airfoils. A plunge motion code (udf file) is defined in Ansys Fluent and numerical simulation of the flow around NACA 0014 and NACA 0012 is performed.

CHAPTER 2

LITERATURE REVIEW

The growing interest in micro-air vehicles has made it necessary to improve our understanding of their aerodynamics. A reasonable place to start is to examine airfoil aerodynamics below 10,000 Reynolds numbers, also called ultra-low Reynolds numbers. With an incompressible Navier-Stokes solver, we examine how airfoil geometry affects performance. As micro-air vehicles gain popularity, improved aerodynamic knowledge is becoming increasingly important because of variations in terms of camber, thickness, as well as the leading and trailing edge shape.

Using numerical simulations, Kurtulus [28] examined the impact of airfoil thickness and incidence angle on the alternating vortex patterns on the symmetric airfoils with Re=1000. It is found that as the incidence angle increases, this alternating vortex pattern varies significantly in shape. In this study, the results are obtained with 1° increment from 0° to 41° and then with 10° increments from 40° to 180°. A 12% thick (NACA 0012) and 2% thick (NACA 0002) airfoil is examined for instantaneous and mean vortex patterns. In addition to the Strouhal number, the average lift, drag, and pitching moment coefficients are calculated; compared with those found in literature. A continuous vortex shedding pattern is observed behind NACA 0002 at Re=1000 and below 7 degree at NACA 0012 at Re=1000 in the airfoil's wake region. According to the wake structure, five different modes have been distinguished based on the instantaneous and mean vorticity fields as well as amplitude spectrum of the lift coefficients, velocity fields, instantaneous aerodynamic coefficients, mean aerodynamic force coefficients, and vortex spacings; both lateral and longitudinal . A noticeable increase in lateral spacing can

be observed at the downstream end of the vortex street and that the vortex street is also deviating from the horizontal line and tends to rise and fall instead of remaining horizontal. Increasing lateral spacing caused by the wake deflection results in an increase in spacing ratio (*b/a*).

For stationary airfoils, Kurtulus [29] explains that alternating vortex patterns are generated by the interactions between their upper and lower surfaces, producing time-dependent flow patterns. A symmetric airfoil is examined with an increasing incidence angle to study unsteady flow behavior. An overview of flow patterns at various angles of attack is presented in this paper. Numerical analysis of the vortex pattern generated around NACA 0012 at Re=1000 is conducted based on various angles of attack. A laminar flow and thick boundary layers are expected at this Reynolds number. Flow separation and unsteady vortex shedding is noticed particularly in case of small angles of attack. NACA 0012, for Re=1000, exhibits an unsteady vortex pattern at an angle of attack of 8°. As part of the spectrum analysis process, angles of attack of 0° to 90° are considered. For NACA 0012, the lift coefficient (C_l) amplitude spectrum peaks at 8° which is followed by oscillatory behaviour of the aerodynamic forces.

An angle of attack-based analysis of mean versus instantaneous aerodynamic coefficients is presented in this paper. This paper investigates the formation and separation of vortices from airfoils' upper surfaces by time-averaged analysis of pressures, friction coefficients and streamlines. In this case, 23° is observed to be the angle of attack at which the vortex splits. A vortex splitting up was observed at $\alpha = 41^{\circ}$ degrees in the current study. The drag coefficient increases with increasing wake width. It can be seen from the vortex pattern of $\alpha \gg 50°$ that vortices merge over a period of time before the shape of a singular Karman Vortex emerges in the wake.

Based on numerical simulations, Khalid et al [30] demonstrated that pitching and plunging motions are equivalent for flapping NACA0012 airfoils. At Reynolds number 10^3, incompressible Navier-Stokes equations are computed corresponding

to a wide range of Strouhal numbers. The trailing edge length scale is compared with pitching and plunging motions using the Strouhal number as a criterion. In both spectral and temporal domains, there is a good correlation between the aerodynamic coefficients. This paper discusses how falling or pitching airfoils produce aerodynamic force through a variety of mechanisms. These mechanisms include vortex shedding, mass addition, and the interaction of the leading edge vortices and the trailing edge vortices. In plunging airfoils, wake deflection results in a bias in lift coefficients at high Strouhal numbers. As a result of further investigation, it appears that the second harmonic of the fundamental frequency dominates in the lift spectrum. A typical observed phenomenon is strongly influenced by quadratic nonlinearity.

Low Strouhal numbers do exhibit wake deflection, but not to a significant extent.It was found that wake deflection does not depend solely on the starting position. Lower Strouhal numbers result in a deflection of the wake downward for upstrokes and vice versa. As Strouhal numbers increase, however, the pattern changes and becomes more prominent. The appearance of quadratic nonlinearity causes symmetry-breaking in nonlinear systems. In order to quantify this nonlinearity, the lift coefficient's first even harmonic has been used. According to the results, the wake deflection is primarily caused by quadratic nonlinearity.

Using angles of attack from 0° to 10° and increments of 1° for each simulation, Ahmed and Kurtulus' article [31] illustrates the flow around cambered airfoils that are relevant to Micro Air Vehicles (MAVs). Cambered airfoils and their effects at considerably low Reynolds numbers are examined by comparing aerodynamic coefficients between three different cambered airfoils, including NACA 1412, NACA 2412, and NACA 3412. It is evident from the analysis that with increasing camber, the mean lift coefficient increases by around 7-9% and the mean drag coefficient increases by around 2.5%. In the case of leading edges, the suction pressure decreases as the maximum camber increases. In order to better understand

how vortex structures behave for different cambered airfoils, instantaneous streamline structures have been studied at various angles of attack. The airfoils investigated for Re=1000 exhibit alternate vortex shedding at angles greater than 9°. In case of angles of attack less than 8°, the vorticity flow field is continuous. Flow separation position has also been analyzed using skin friction coefficients for cambered airfoils. It is clear that flow separation points shift towards the trailing edge of an airfoil as the camber of the airfoil increases. A higher angle of attack, however, results in shifts in flow separation points to the leading edge.

Using a numerical analysis of unsteady wind tunnel and ground interference effects in a time domain, it has been found that the transonic flutter characteristics of the NLR 7301 section within a wind tunnel are influenced by the NACA 0014 airfoil plunging near the ground plane, while thrust generation characteristics of the NLR 7301 section. The deformed grid, parallelized, multi-block, unsteady flow solver in this study [32] is employed in conjunction with a two-degree-of-freedom structural model. A porous-wall boundary condition represents the tunnel walls in this study for the purpose of analysing transonic flutter. An unsteady solution as well as a steady solution are significantly affected by the type of porous boundary condition. A significant difference between free-flight flutter behavior and that found in a porous wind tunnel can be attributed to the strongly dependent relationship between tunnel porosity and wall proximity. Using ground effect, this paper analyses the trailing edge boundary condition of the airfoil. Based on calculations, boundary conditions affect the solution only if the flow field is nonlinear, but not when parameters are averaged over oscillation cycles. Additionally, the turbulence model has the same effect on fully turbulent, unsteady computations. A laminar flow with no turbulence model, on the other hand, closely matches experimental data of low Reynolds numbers.

Using a turbine embedded underwater for energy harvesting, Johnson, Susan R [33], conducted research to determine which airfoil configuration produced the most thrust for a sailboat. A study of three different types of airfoils was conducted, namely single-element airfoils, two-element airfoils, and cloth sail airfoils. The analysis was performed using ANSYS CFX, a computational fluid dynamics program. It was observed that two main conclusions could be drawn. As a first conclusion, computational fluid dynamics does not agree with experimental findings regarding the drag over a NACA 0012 airfoil having only one element. Flow separation prediction led to an overestimation of drag in the case of angles of attack greater than eight degrees. Second, a sailboat with a two-element airfoil proved to be the most optimal configuration to maximize thrust. An airfoil with two elements outperformed a cloth or single element airfoil by a significant margin when lift over drag was compared across an angle of attack sweep.

The two-element airfoil is most suitable for hydroelectric sailboats due to its superior lift-to-drag ratio. The efficiency of airfoils with only one or two elements is almost half that of those with two elements. The two-element airfoil design also allows for a lot of deflection adjustments to be made to ensure that the sail set-up is according to the circumstances of the environment, which a single-element airfoil is not able to achieve. This simulation was not able to capture all the variables involved in modelling a cloth sail accurately. Cloth airfoils exhibit laminar and turbulent boundary layers. There is a difficulty in predicting the transition from a laminar boundary layer to a turbulent boundary layer when a sail changes shape due to the sailing conditions. The shape of the sail should be adjusted according to sailing conditions. Laminar boundary layers tend to transition smoothly into turbulent ones this way.

Lund [34] studied flapping wings experimentally and numerically. This vehicle is several times larger than the specifications for MAVs, despite being prompted by their development. This model was selected based on several factors including verifying a numerical code, displaying smoke, understanding flapping-wing

propulsion, low Reynolds numbers, and all these factors in turn lead to simplification of the assembly. A locally developed panel code, USPOT, was used for the numerical analysis. With three degrees of freedom, the code models two independently moving airfoils. The thrust and efficiency of two harmonically oscillating airfoils were calculated when they performed plunge-only motions. According to the numerical analysis, opposed-plunge flapping-wing thrust generally follows a similar pattern. As predicted by linear theory, thrust increases about proportionally in accordance with the square of frequency, as indicated by the code.

The experiment was carried out in the NPS 1.5 m x 1.5 m in-draft wind tunnel. The numerical flow was approximated with the help of an earlier developed long-span flapping-wing model which was supported by cables. This experiment employed a bi-wing configuration with wings that performed only plunge motion. Streamwise displacement caused by flapping in the model was indirectly used to calculate thrust. During computation, viscous boundary layer drag was minimized by subtracting steady state drag from thrust.

In this study, Jones' [35] previous work with the same model configuration was compared to the results of the current study. Various frequencies were used in the current study. There is an increase in thrust with velocity based both on linear theory and numerical codes. The experimental thrust measurements were compared directly with the numerical thrust measurements. Higher thrust is consistently predicted by the panel code compared to what was observed in the experiments. It is primarily because of separation, three-dimensional effects, and wing flex that experimental thrust differs from numerical thrust. However, experimental values produce the same results as numerical values.

According to Jones [35] several attempts were made at designing, manufacturing, and testing flapping-wing microair vehicles in order to refine and improve performance. With the new model, the model became more modular and reliable, with a heat sink that enabled higher motor loads without damaging the motor, using

micro-film instead of Japanese tissue wing skin in order to reduce weight, and using a closed-loop control system that operated at over 38Hz.

By using smoke-wires, streaks were produced uniformly at low flow speeds, making it possible to characterize some flow properties. Despite the fact that the angle of attack is zero, the leading-edge spar was exhibiting vortex shedding on both sides despite previous tests showing improved thrust from the current airfoil design. The flow was completely separated from the suction side of the airfoil throughout the flapping cycle at frequencies as small as 0.6 and Reynolds numbers below 24,000. Visualization showed that centerline flow remained planar even at high frequencies, and a panel code provided an accurate representation of wake topography. It was found, however, that the flow away from the centerline was highly three-dimensional, and changed with frequency significantly

A similar pattern was found in direct thrust measurements to previous studies, with the highest thrust at zero flight speed. The newly developed model, however, produced seven times more thrust than the previous study due to the much higher frequency offered by the closed-loop controller. In addition to hovering, the newly developed model overcame its own drag by 5.5 meters per second. Aeroelastic feathering was used on the wings of the model. Aeroelastic joints were found to have relatively small effects on thrust for a given velocity and frequency. However, more flexible wing mounts reduced the motor load, which allowed the model to achieve much higher frequencies and, consequently, result in increased thrust. Although more testing is needed to determine whether tip-plates improve performance, the current results suggest they do not.

Various conditions have been investigated in the study by Hamadani et al. [36] to determine how 2-D airfoils produce thrust during pure plunge movements. The varying airfoil shapes, the different Reynolds numbers (Re) and the reduced frequencies (k) are all part of the conditions described above. Three airfoils were examined in the present study: the NACA0014, ellipse, and flat plate airfoil, along with three different Re values: 1000, 10000, and 25000 for 2.0, 1.0, and 0.5 k values.

These parametric studies have been conducted with a constant thickness (t/c ratio) of 14% across all airfoils. In sinusoidal plunging motion, C_l and C_d vary sinusoidally, but the airfoil motion lags C_l and C_d, resulting in a time-averaged lift coefficient that is zero over the course of a single cycle, but a time-averaged drag coefficient that is negative and non-zero, resulting in thrust.

In the airfoil's wake, a Reverse Karman Vortex Street forms, which generates thrust. The drag coefficient value generated by the NACA0014 is much higher when compared to either the ellipse or flat plate. An airfoil with a large Δy variation is likely to exhibit larger pressure changes close to the leading edge, indicating that the shape effect plays a significant role in thrust generation. With increasing Re, the NACA0014 airfoil develops a negative time averaged drag coefficient. While the thrust generated by the other two airfoils remains high, the airfoil shape clearly dominates. By reducing *k*, the shape effect on the airfoil becomes less pronounced (or the unsteady effect becomes less noticeable) and thereby the time averaged drag coefficient (thrust) is reduced. There is an interesting fact that in all circumstances, the C_{dv} (drag generated by viscous forces), which is the main cause of negative drag (thrust), is very small, while pressure forces constitute the primary factor causing negative drag (thrust).

According to Young et al. [37], a compressible two-dimensional Navier-Stokes solver has been used for numerically simulating the flow over a sinusoidally oscillating NACA 0012 airfoil oscillating in plunge with Reynolds number 2×10^4. Visualizing the airfoil's wake is accomplished using numerical particle tracing. Assuming laminar flow, numerical simulations of wake structures are in close agreement with experimental wake visualizations. Strouhal number and reduced frequency *k* of the plunge oscillation both affect airfoil lift, thrust, and airfoil's wake structures at this Reynolds number. At frequencies below approximately k = 4, leading-edge separation dominates the production of aerodynamic forces, while at higher frequencies it becomes secondary. Until $k = 20$, it appears that trailing-edge

effects are primarily responsible for controlling frequency. It is clear from the results of aerodynamic force measurements at this Reynolds number that they differ significantly compared to their potential flow predictions at low plunge frequencies and large amplitudes, whereas these are consistent at high plunge frequencies and small amplitudes, indicating that leading-edge separation is a factor.

An N–S flow solver that can handle both laminar and turbulent flow conditions was used to simulate the two-dimensional NACA 0012 airfoils' wake oscillating sinusoidally during plunge. The freestream Mach number has an obvious influence on the forces predicted by the N–S code when validated against pitching airfoil simulations. The plunging airfoil results also demonstrate this. Despite this, reducing the Mach number has no significant impact on the wake structures captured during the simulations, except for the need for more grid refinement to identify matchups between the simulation and experiment. There is a distinct difference between the wake structures of plunging airfoils with and without leading-edge separation, as trailing-edge flows behave very differently. However, the aerodynamic forces are only substantially different when the leading-edge flow has been separated. Considering these findings, leading-edge effects play a crucial role in describing the forces generated at this Reynolds number due to plunging airfoils. Wake structures are strongly motivated by trailing-edge effects but lift and thrust are impacted to a lesser extent.

A new parallel solver is presented in this paper by Lianga et al. [38] that uses Correction Procedure via Reconstruction (CPR) to solve viscous flows on deforming and moving grids. To efficiently employ flux derivatives, it is shown that no explicit geometry conservation law is required for unstructured grids with quadrilateral cells; the free-stream conservation occurs implicitly. To validate CPR code, a moving inviscid vortex on moving grids as well as deformed grids is used as a reference case. As a result, the accuracy of orders is optimal. Afterwards, this method is utilized to investigate viscous flows on moving or deforming grids. CPR solves viscous flow

conditions that have moving boundaries more quickly and almost as accurately as the SD method.

In addition to experimental results, the proposed method has been verified with respect to the similar numerical methods. Moreover, the results of the validation show that the method can yield solutions with a high degree of accuracy. There is also the finding that the solver is close to linearly scalable. Further, NACA0014 airfoils had an average drag coefficient 25% higher than NACA0012 airfoils in plunge cases. The increase is reduced to 11% in plunge and pitch cases.

It is necessary to acquire a deeper comprehension of aerodynamics in a flow regime that has not been extensively studied so far if powered flight is to be achieved at ultra-low Reynolds numbers and at the microscale. The objective of this study by Kunz [39] aimed to examine the aerodynamics of this environment and apply the insights gained in analysing, designing, fabricating, and testing micro-rotors operating at a scale never before accomplished. Ultimately, these efforts have resulted in micro-rotorcraft that are both the state of the art and representative of what is yet to come in the realm of technology.

Using an incompressible Navier-Stokes solver, we investigate how airfoil geometry affects performance. The leading and trailing edges are studied for variations with respect to camber, thickness, and shape. According to the results, a decrease in Reynolds number is associated with an increase in maximum lift coefficient. Despite this, lift-to-drag ratio continues to decrease. Due to this, the power requirements for flight are more constrained than the lift requirements. It is possible to mitigate this performance penalty by carefully designing the airfoils. At ultra-low Reynolds numbers, geometry still has a profound impact on performance despite viscous fairing, contrary to the notion that it decreases the effectiveness of airfoils' geometry. Combining the flow solver with an optimizer further explores this design space. It has resulted in the first airfoils quantitatively designed for this flow regime and a

demonstration of the significant performance gains that can be achieved by employing unconventional camber lines.

Using modified classical rotor theory along with Navier-Stokes data, rotors with ultra-low Reynolds numbers have been produced. It incorporates both design and analysis optimization to predict performance. A variety of micro-rotor designs are predicted using these tools and compared to experimental data and three-dimensional Navier-Stokes analyses. Analyzing the experimental findings and comparing them with the analyses, there is some agreement on the parameters of thrust and power on a global scale. However, the distributions of these parameters at the spanwise level differ significantly, partly due to rotational and three-dimensional effects. At ultra-low Reynolds numbers, blade-element types of methods may not be applicable to detailed rotor design, but they may be useful for evaluating concept feasibility and developing initial designs for prototypes, postprocessing, and refinement. Several prototype rotorcrafts have been designed and tested so that controlled powered flight can be developed at the scale of centimetres. This has been done with a view to gaining a deeper understanding of both aerodynamics and system integration.

Osama [40] conducted a study that used laser Doppler velocimetry and flow visualization to study the flow over flapping airfoils at low speeds. A sinusoidal plunge NACA0014 airfoil near a ground plane, a sinusoidal plunge NACA0014 airfoil in a biplane configuration, and two sinusoidal plunge NACA0014 airfoils oscillating counterphase were the subjects of this study. The following factors that were considered in this research: The ratio of plunge amplitude to chord set over an airfoil was 0.4, the reduced frequency of oscillation was taken as 1.0, and the Reynolds number was taken as 8760 based on the chord of the airfoil.

To provide a detailed description of the flow characteristics that are created with this kind of flapping motion, the axial flow velocity has been measured under various conditions at multiple points in the flow field to obtain detailed information. The flapping cycle also included visualizations of instantaneous flow fields and time-

averaged flow fields. Furthermore, a laser range finder was utilized to measure the thrust generated by sinusoidal motion. It can be observed that both the leading and trailing edges of the airfoil shed vortex.

This present work included visualization of the flow around NACA0014. During the experiment, smoke was generated upstream of the wing, and for the purpose of visualizing the flow, still and video cameras were used to capture images of the flow. Through the design and construction of an easy tool, it was possible to adjust the angle of attack. Two main cases were studied using the flow visualization technique. Airfoil with angle of attack of 0° and 4° was first analyzed. Secondly, three different biplane configurations were examined.

Observation 1: zero angle of attack and the tunnel speed was set to $U_{\infty} = 2.24$ m/s, so the Reynolds number was 10,000. The upper surface of the airfoil showed a small separation area near the leading edge.

Observation 2: the tunnel speed remained the same, $U_{\infty} = 2.24$ m/s, but the angle of attack was increased to 4° and recorded flow around the airfoil using a video camera. The pictures were extracted from the recording using a grabber computer card. An airfoil's wake is illustrated by the extracted photographs showing how vortices develop and shed downstream.

Observation 3: To examine the biplane configurations, three different cases were considered. In all these cases, the speed of the tunnel was kept constant at $U_{\infty} = 2.24$ m/s and Re = 10,000.

Case 1: In this case, the wings were positioned so that there was a minimum distance between them. The presented consecutive frames were captured using a video camera at a time step of 1/30 of a second.

Case 2: The wings were positioned in this case so that they were at the maximum distance from one another.

Case 3: In this case, the falpping with fixed at $f = 5.6$ Hz and the corresponding reduced frequency; $k = 1$.

To capture flow characteristics in detail in the vicinity of the airfoil, the strobe light and frame rate of the video camera were altered during the experiment. When a frame speed of 1/60th of a second was selected for the frame rate, no details could be recorded. There was only a recording of average streamlines. Cameras were able to capture flow detail at 1/500 of a second when the frame rate was increased. Therefore, the flow was visually frozen with a strobe light. Due to this phenomenon, downstream vortices tend to look stationary. Strobe light frequencies were measured, and shedding frequency was computed.

The hybrid lattice Boltzmann method (HLBM), a type of method that incorporates both the standard lattice Boltzmann approach and a finite-volume approach that is unstructured, is used by Ilio et al. [41] in their simulation of two-dimensional flow around the NACA 0012 airfoil. This study aims towards quantifying computational method's robustness and numerical performance. The numerical solution to this problem is analysed under multiple angles of attack at 1000 Reynolds numbers using different angles of attack. After an estimation of the method's accuracy is provided, a convergence study is conducted. Furthermore, flow fields for zero angle of attack are computed at Reynolds numbers up to 10^4. The numerical simulations captured boundary layer separation, static stall, and other physical phenomena. The vortex shedding regime for a Reynolds number at 1000 begins at an angle of attack of roughly 8°, and the stall phenomenon occurs at an angle of attack of nearly 26°, the critical angle. In addition, airfoils with angles of attack exceeding 26° exhibit steep decline in lift forces. There is consistency between the results reported in the literature and the results obtained here. Drag and lift forces that are exerted upon the body are generally computed satisfactorily across all parameters, and the fluid flow phenomena involved appear well predicted. Grid refinement is performed on uniformly spaced components to make the model as numerically efficient as

possible. In comparison to off-lattice Boltzmann methods that use body-fitted meshes, the HLBM exhibits excellent performance near solid curved walls.

To be able to thoroughly understand the unique lift characteristics demonstrated by the NACA 0012 aerofoil at low Reynolds numbers, numerical investigations have been carried out by Pranesh et al. [42]. In this study, calculations were carried out at Re = 10,000–100,000 for various angles of attack and freestream turbulence intensity. This symmetrical aerofoil is characterized by a limited set of parameters. If positive angles of attack are applied to this aerofoil within this range, the net circulation around it will be negative, resulting in negative lift. In this paper, different flow regimes are identified as possible causes of the unusual behaviour of negative lift, and physical explanations are given for such behaviour. Different flow parameters are also discussed as possible causes of this unusual behaviour.

A lift coefficient for positive α is negative within a limited range near to 0°. It was determined that there are five flow regimes, of which the laminar separation case without turbulence transition and reattachment corresponds to the Cl– α dependence with its counter-intuitive behavior. In all cases involving negative lift coefficients, the Kutta condition was violated. Nevertheless, not all violations of the Kutta condition will lead to a negative lift. It is imperative to emphasize that, in addition to the separate region's shape, differences in boundary layer displacement thickness along the upper and lower surfaces produce significant negative camber within the separated region, which leads to increased negative circulation around the aerofoil.

A study by Naeem et al. [43] was conducted in which instantaneous wake structures being produced by a 2% thick NACA 0002 symmetric airfoil were numerically evaluated in two dimensions for a variety of angles of attack and Reynolds numbers starting from 100 and reaching up to 3000. The vortex structure of flow patterns is discussed as a basis for classifying flow patterns. The sudden variation of the mean aerodynamic coefficients due to transitions from one mode to another and switching between modes is connected with Reynolds-based bifurcations, as well as with

sudden changes in forces acting on the airfoil. In addition, an assessment of how wake patterns evolve over time and how they behave in the wake of airfoils was conducted. This was followed by an analysis of their impact on the airfoil's aerodynamic characteristics.

In case of low angles of attack ranging from 0 degree to 10 degree, Kurtulus [44] examined the unsteady vortex evolution of NACA 0012 airfoil using a numerical model with separation at its trailing edge. The Reynolds number in this case lies between 1000 and 4000. At its trailing edge, this flow is observed to have a laminar separation bubble, which has been discussed besides the main flow characteristics. An analysis of a detailed flow field, performed for a range of angles of attack and Reynolds numbers, has been able to provide insight into how the force evolves from a steady condition to a periodic state. The current study has also identified the angle that contributes to the creation of a laminar separation bubble as well as how that affects its behaviour. The formation angle of the LSB as well as the critical angle of attack tend to decrease with an increasing Reynolds number (1000 to 4000).

An analysis of the numerical simulation of wake formation patterns downstream is presented by Kurtulus [45] along with a comprehensive description of the vortices created downstream at a critical angle of attack pertaining to the NACA 0012 airfoil. These instantaneous vortices oscillate at low Reynolds numbers (1000 to 4000) in contrast with mean vortex pattern. In the event that the wake becomes unstable, it causes the original vortex to fragment downstream of the airfoil into alternate vortices as a result. Across the Reynolds number distribution examined, a decrease in critical angle occurs as Reynolds number increases. Consequently, lower Reynolds numbers lead to later separation. It is evident that multiple vortex rows form at $Re = 4000$. It is evident that multiple vortex rows form at $Re = 4000$. It is observed that the vortex cores of opposite signs are positioned approximately halfway between the vortices of the same sign at $Re = 1000$. According to the present study, six different regions are identified in the space generated by Kármán ratios and dislocation ratios.

Gunaydinoglu et al. [46] provide an approach to reconstructing pressure fields for laminar flow by utilizing planar particle image velocimetry measurements. This is a method for solving governing equations that rely on measured velocities as boundary conditions. Through the use of semi-implicit pressure-linked equations, the governing equations can be evaluated. This method begins by using a staggered grid of interpolation to construct a velocity field based on the measured velocity measurements. An initial pressure field is obtained by solving the continuity equation for incompressible flows as a pressure equation. A mass imbalance is calculated by solving the momentum equation by incorporating the pressure correction, then solving the momentum equation as a function of the pressure field. Although significant experimental discrepancies can be encountered, this method is capable of recreating pressure fields efficiently based on error-free velocity fields. With the least probable end-user involvement, the proposed method provides unobtrusive, global pressure measurements for flows that are laminar.

The study was carried out by Kurtulus [47] to examine the capabilities of artificial neural networks (ANNs) as an approach to modelling flapping motion dynamics that takes into account the unsteady coefficients of aerodynamic force. In this study, a neural network model is presented which was developed by relying on a multilayer perception (MLP) network and the Levenberg-Marquardt optimization algorithm was incorporated. There were two groups of flapping kinematics data that were analyzed for both training and testing of the artificial neural network that was built on the data. The ANN model demonstrated its ability to simulate unsteady flapping motion kinematics and associated aerodynamic forces by predicting both the lift coefficient and drag coefficient. Simulation and numerical results indicated identical trends for the force coefficients.

The study by Beker et al. [48], a four-bar flapping mechanism with one degree of freedom is presented, and the experimental force results are compared with the results from the theoretical analysis, FSI analysis and FEA analysis. In order to determine the inertial loads that are generated by the conceptual flapping wing

mechanism, theoretical, FEA and finite element analyses are carried out. An analysis of both tangential and centripetal forces encountered in the wing and linkages of Calliphora Erythocephala is used to derive a rigid-body dynamics formulation. Afterwards, the force is investigated for its contribution to lift. FEA calculates the total inertial forces along the lift direction by defining the dynamic implicit step. CFD and dynamic structural analysis are combined to determine the inertial forces in the lift direction in an FSI analysis. FSI analysis and FEA for flapping wings found a difference of 0.135mm tip deflection.

Senol et al. [49] conceptualize, construct, evaluate, and then compare the experimental results with those obtained from using a numerical solution for a flapping wing four-bar mechanism. An equation of motion for a flapping wing incorporating a double rocker, four-bar linkage arrangement with a single degree of freedom was introduced for kinematic analysis. An analysis of the aerodynamic forces at an instantaneous time is also performed using CFD. Upstrokes generate positive lift, while downstrokes generate negative lift. Hover cases have vortices of greater magnitude at the tip, as opposed to the root, which indicates that vortices are of paramount importance. In the vicinity of the tip, a remarkably pronounced vortex forms.

Using a bimorph piezoelectric material, Comez et al. [50] devised a setup that measured the displacements caused by flapping wings. The experimental study employed two separate wing models: a Rufous hummingbird and a rectangular flat plate. With respect to wing span, the rectangular wing is the same as the hummingbird wing model. Rufous hummingbird wings are the inspiration behind the first model. With the assistance of a function generator and an amplifier, PZT material provides the flapping wing motion. Piezoelectric material is treated with a single type of wave function between 0 and 20 Hz. Further, an instantaneous wing displacement measurement is carried out using a digital image correlation system (DIC).

The study by Hizli et al. [51] visualizes instantaneous flow over SD7003 and NACA0012 airfoil sections subject to sinusoidal pure pitching and plunging motions numerically through the use of CFD software Fluent 6.3 and experimentally through Particle Image Velocimetry (PIV) analysis. Among NACA0012 airfoil sections, purely plunging yields the highest mean lift coefficient, while purely pitching yields the lowest. Additionally, SD7003 airfoil sections that plunge produce the lowest mean drag coefficient and SD7003 airfoils that pitch produce the highest mean drag coefficient.

A SD7003 airfoil subjected to 0c (normal hover), 0.5c, and 1c vertical translation amplitudes was numerically investigated by Gunaydinoglu et al. [52]. Hovering aerodynamics in the presence of vertical translation is numerically investigated for constant Reynolds numbers as well as for reduced frequencies. In order to solve the laminar, incompressible and unsteady Navier-Stokes equations, a pressure-driven algorithm incorporating dynamic meshing is used along with a commercial pressure-based solver. In general, the Reynolds number and reduced frequency do not affect the trends in force and vortex fields; however, they lead to higher peak values in aerodynamic forces that are related to a given motion regardless of reduced frequency.

In their study, Kurtulus et al. [53] examine instantaneous vortex dynamics that result from potential flapping motion. For the purpose of investigating how unsteady aerodynamics and vortex formation affect flapping motion over the entire flapping cycle, a simplistic approach was employed. It prevents the use of quite intricate and challenging wing geometry and motions of real insects or birds. This analysis of PIV measurements and visualizations of laser-based sheets assists in identifying the various vortices generated by flapping motion. It was observed that the following distinct types of vortices were formed: Leading-Edge Vortex (LEV) generated near airfoil's leading edge, Translational Vortex (TV) created near the trailing edge during translation, and Rotational Stopping Vortex (RSV), which were generated during rotation at the airfoil's trailing edge.

Kurtulus et al. [54] were interested in finding the optimum parameters that generate the maximum lift through a numerical and analytical approach. A variety of different examples have been studied with different variables like angle of attack, incidence start position, and velocity initial location. Data on instantaneous drag coefficients and velocity are also used to estimate mean profile power coefficients. Lift values are observed to be positive throughout the motion after 30° angle of attack. With regard to the DNS code used during this study aiming to determine whether different parameters have an impact on aerodynamic force coefficients, the analytical model developed using Wagner and Küssner functions is comparable to the Rankine-Froude momentum jet theory in conjunction with the Duhamel Integral.

As part of this work by Kurtulus [55], a direct numerical simulation in combination with an experimental analysis gives insight into the vortex dynamics that originate from a moving wing. The analytical model is subsequently refined so that it is possible for the parameters of motion to be optimized in order to maximize force. A symmetrical airfoil is incorporated. With Reynolds numbers between 500 and 2000, the flow can be considered incompressible and laminar. To analyze the flow phenomenologically, visualization of laser sheet and particle image velocimetry results is carried out concurrently with the numerical simulation results. An independent method for modelling aerodynamic forces is presented using the Duhamel integral. A comparison is made between the results obtained by this method and those obtained by numerical simulations.

CHAPTER 3

METHODOLGY

A two-dimensional, incompressible Navier-Stokes equation has been solved in ANSYS-FLUENT [56], a commercial software based on finite volumes, to determine flow over NACA 0014 airfoil in both stationary mode and pure plunge mode and also NACA 0012 in stationary condition. A SIMPLE fully implicit algorithm is employed for this study. The coupling between pressure and velocity is implemented using a second order scheme, as well as all the discretization in terms of temporal and spatial dimensions. There is only one case in which a dynamic mesh is enabled, and this is when a pure plunge case is computed.

3.1 Governing Equations

The governing equations that have been employed in this current study are two-dimensional, incompressible, and laminar Navier-Stokes equations and can be described in the following way:

$$\vec{\nabla} \cdot \vec{V} = 0 \qquad (1)$$

$$\frac{\partial \vec{V}}{\partial t} + \left(\vec{V} \cdot \vec{\nabla}\right)\vec{V} = -\frac{1}{\rho}\vec{\nabla}p + v\nabla^2\vec{V} \qquad (2)$$

Here, $\vec{V}$ is the velocity vector, ρ is the fluid density, p is the pressure and v is the kinematic viscosity. As part of its conservation equation solutions, ANSYS Fluent

implements the finite volume method [56]. In this case, the SIMPLE-type fully implicit algorithm is implemented in order to achieve pressure-velocity coupling. In this scheme, a predictor-corrector pressure method is used in conjunction with pressure-velocity coupling. A second order implicit method has been used to approximate the transient solution. The solution is accurate to a second-order spatial and temporal order.

A symmetric airfoil is rotated with a corresponding angle of attack prior to grid formation from the quarter chord location. The field has two domains, one adjacent to the airfoil and another outside the inner domain, extending 15c downstream and upstream of the airfoil. There is a velocity inlet boundary condition specified for the outer domain's semi-circular region, and there is a pressure outlet boundary condition specified for the outer domain's opposite end.

The flow around NACA 0014 and NACA 0012 airfoil is obtained a various Reynolds number. The distribution of the thickness of NACA 4-digit airfoils, y_t , can be obtained by utilizing Equation 3 ([56],[57]) as follows:

$$y_t = \pm \frac{t/c}{0.2} \cdot \left(0.2969 \cdot \sqrt{x} - 0.1260 \cdot x - 0.3156 \cdot x^2 + 0.2843 \cdot x^3 - 0.1051 \cdot x^4\right) \quad (3)$$

Here, $x \in [01]$ is a measure of maximum thickness and t/c is a measure of maximum chord to thickness ratio, expressed in percentage last two digits of NACA 4-digit airfoils. A far field boundary lies 15c away from the airfoil. A symmetrical airfoil like NACA 0014 can be defined by its thickness distribution because the upper and lower surfaces are symmetrical.

The angle of attack is generally described as being positive in the clockwise direction. There are two main angles of attack that were considered in this study: 0° and 4°. In case of the pure plunge, the plunge phase angle (ϕ) is considered at different values and the plots are obtained and compared with the plots available in the literature. The pivot point of the NACA 0014 airfoil was located at a quarter chord location (0.25c) from the leading edge. The current study calculates the pitching moment relative to this pivot point.

3.2 Grid and time-refinement studies

In order to validate the analysis, it is necessary to refine the grid and time step and determine the optimal gird and time step for the present study. A detailed gird and time refinement is performed for NACA 0014 at two different angles of attack: 0° and 4° (Figure 3.3, Figure 3.4)

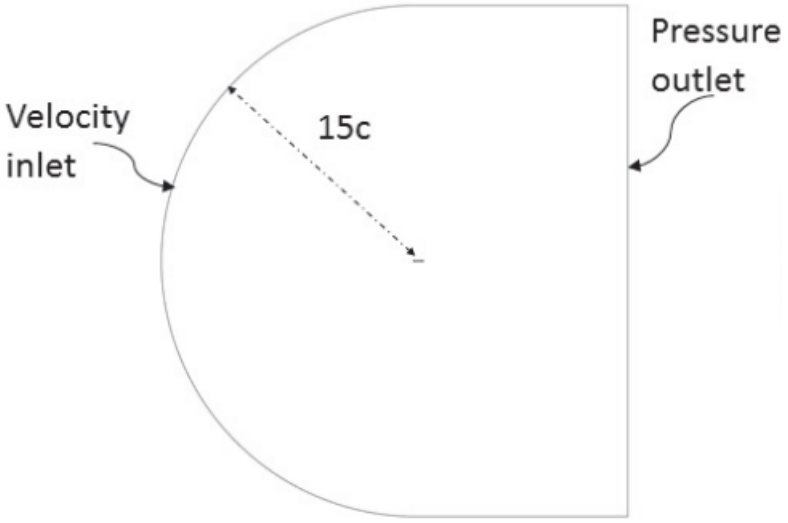

Figure 3.1: Computational domain

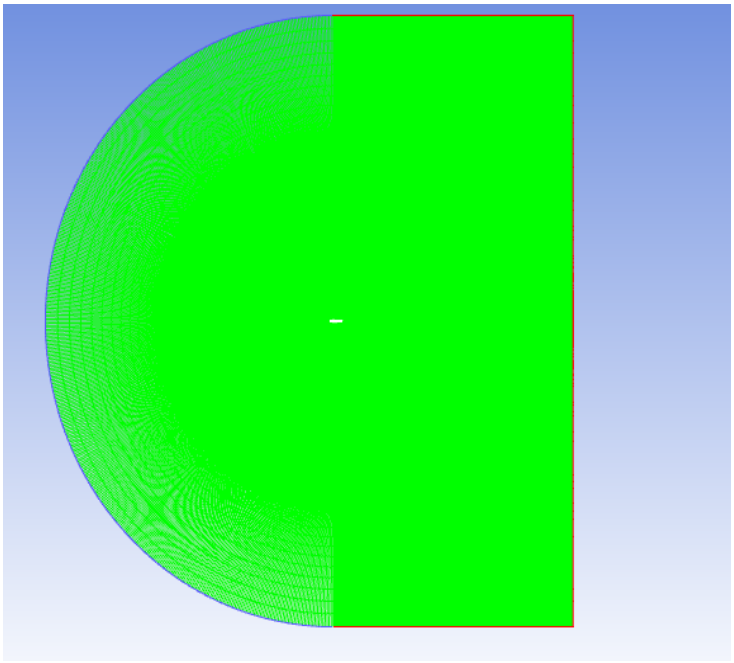

Figure 3.2: Computational domain for medium mesh

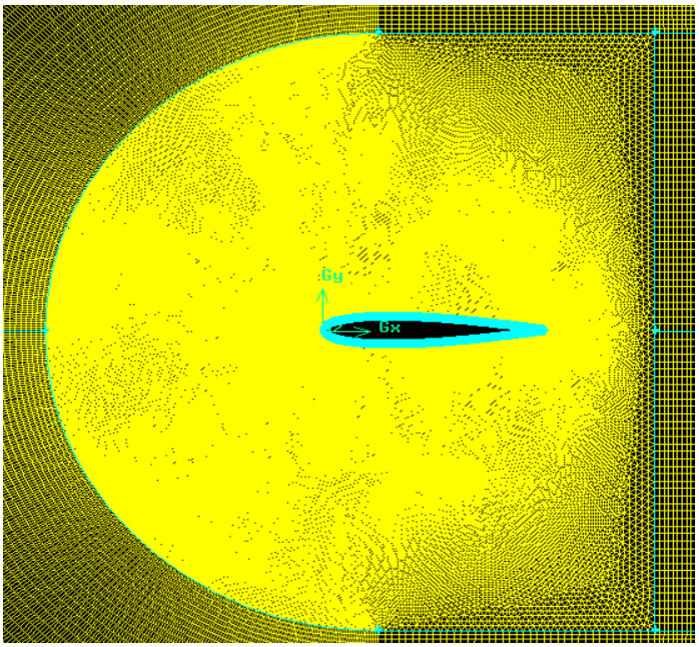

Figure 3.3: Meshed computational domain of NACA 0014, $\alpha = 0^{\circ}$

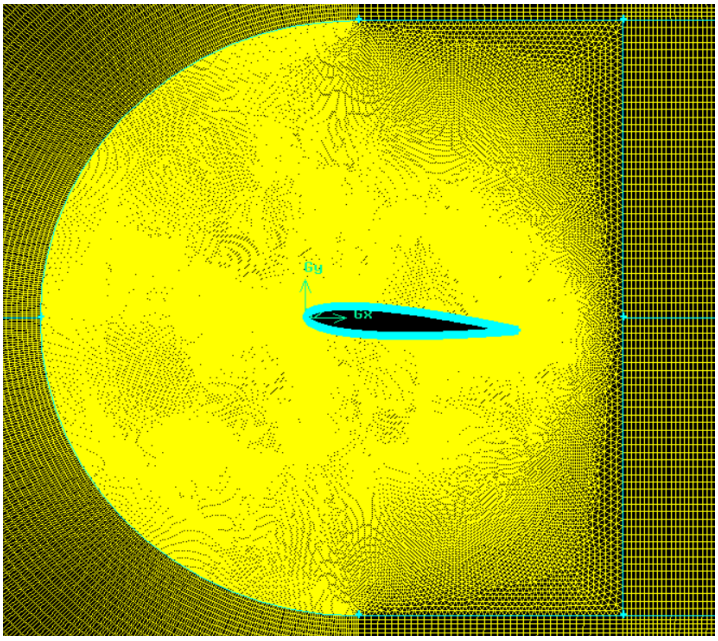

Figure 3.4: Meshed computational domain of NACA 0014, $\alpha = 4^{\circ}$

In case of grid refinement, three different meshes are used: coarse, medium and fine mesh. These meshes are created in GAMBIT grid generation software and then exported to ANSYS-FLUENT for performing simulations. The boundary layer of all three meshes has a first cell spacing of 0.0030c. There are two parts to the mesh around an airfoil, the inner domain, and the outer domain. At the upstream end of the boundary layer, a semi-circle with a radius of 1.5c is constructed centered on the c/4 location of the airfoil. At the downstream end, a rectangular region with a radius of 1.5c is constructed. In the inner domain, the grid is unstructured and triangular. A C-type structured mesh with a radius of 15c is used for the outer domain (Figure 3.1). Airfoils are rotated in the pre-processor program according to the desired angle of attack for the inner domain while the outer domain and wake region remain unchanged.

There are 204 nodes in the coarse mesh, 354 nodes in the medium mesh, and 562 nodes in the fine mesh. A summary of these details is provided in Table 3.1.

Table 3.1: Computational mesh for NACA 0014; $\alpha = 0^{\circ}$ and $\alpha = 4^{\circ}$

Domain	**Nodes around the airfoil**	**Total number of elements**
Coarse mesh	204	123594
Medium mesh	354	231814
Fine mesh	562	324589

The gird refinement is performed at the time interval of $\Delta t = 0.005$s. Simulations of instantaneous results are conducted for a time interval t and t^{*}refers to a non-dimensional time which is calculated as follows:

$t^{*} = \frac{t.U_{inf}}{c}$; $U_{\inf} = 2.28\, m/s$ free stream velocity; $c = 0.064m$ chord length of the airfoil . During the course of this study, grid refinement is perfomed for the pure-plunge case at $\alpha = 0^{\circ}, 4^{\circ}$. In case of pure-plunge, a udf file is complied using Fluent. This udf file is a code that decribe the pure-plunge motion of the airfoil. Additionally, gird refinement study is also perfomed at stationary condition for NACA 0014 at $\alpha = 0^{\circ}, 4^{\circ}$.

Figure 3.5 describes the plunge motion of NACA 0014 airfoil with respect to non-dimensional time. The motion is shown for one peroid. It can be observed from the figure that the airfoil has moved a maximum of 0.025c upwards and a minimum of

0.025c downwards during the pure-plunge motion descrbed in the figure. The plunge motion is a pure sinusoidal motion.

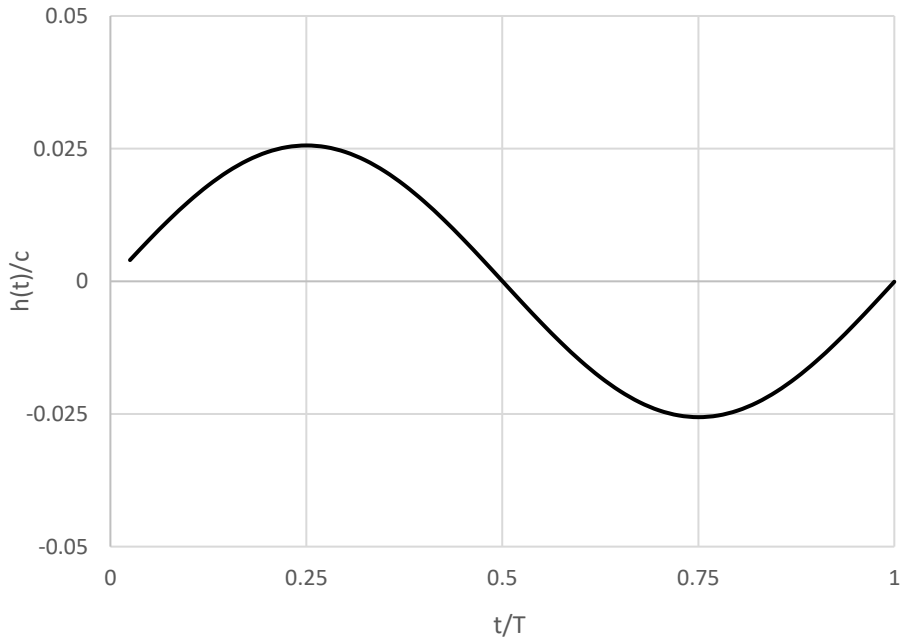

Figure 3.5: Plunge motion of NACA 0014 airfoil (plunging case) at $Re = 1 \times 10^4$ and $k = 1$

Grid refinement for pure-plunge case at $\alpha = 0^{\circ}, 4^{\circ}$:

In the grid refinement study, the aerodynamic coefficients for the medium and fine mesh are nearly identical, especially towards the end of the study. The results for all the three meshes converge around t^*=30s. Consequently, the following simulations were performed using a medium mesh, as the difference between a medium and fine mesh is minimal (Figure 3.6, 3.7).

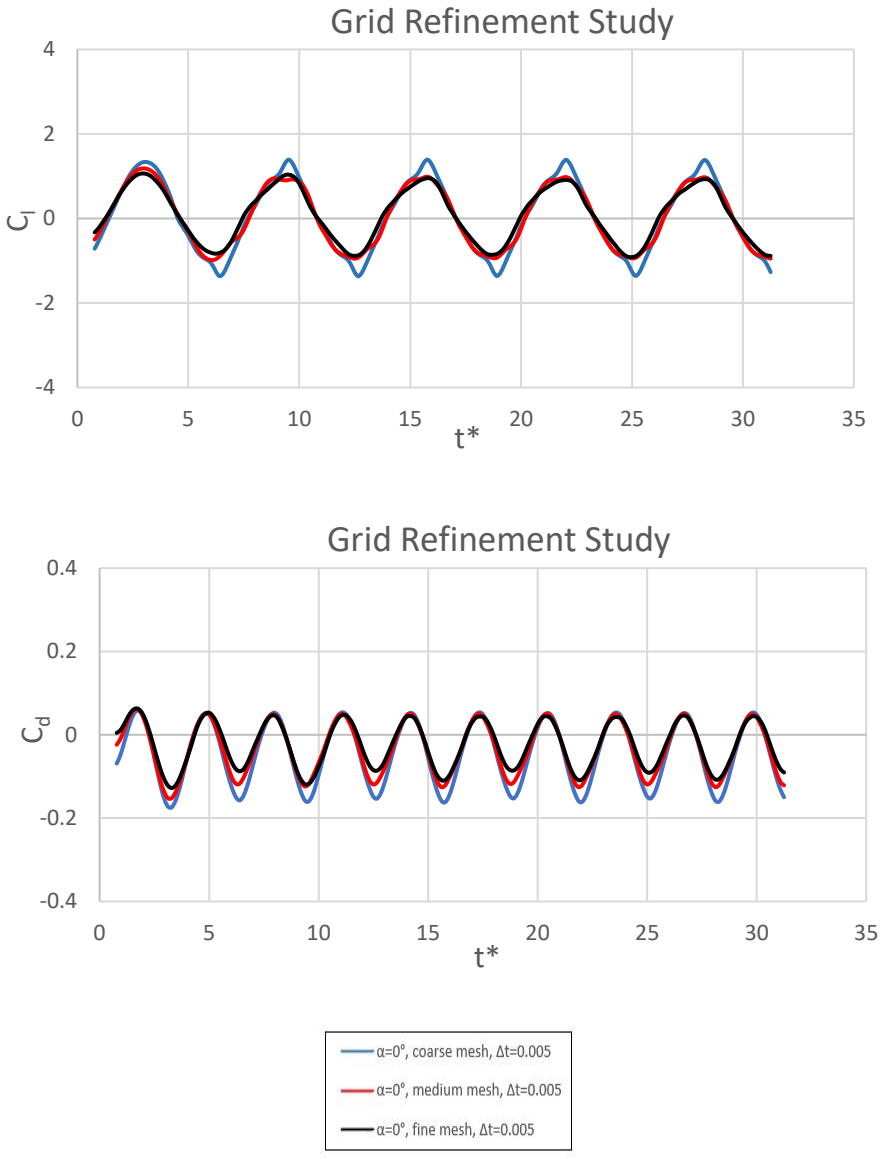

Figure 3.6: Instantaneous lift and drag coefficients for grid refinement study of NACA 0014 (pure-plunge case), $\alpha = 0^{\circ}$

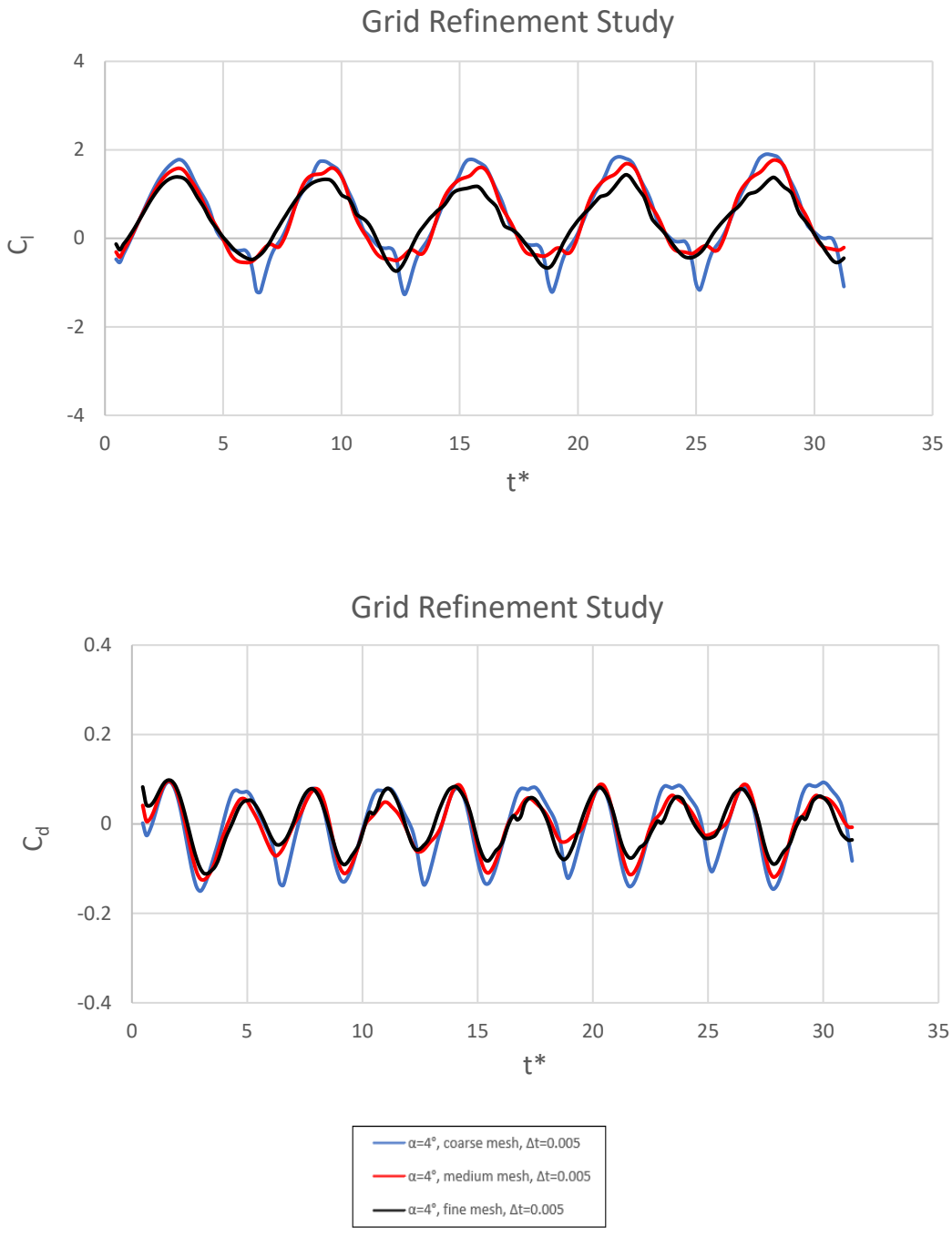

Figure 3.7: Instantaneous lift and drag coefficients for grid refinement study of NACA 0014 (pure-plunge case), $\alpha = 4^{\circ}$

Time refinement for pure-plunge case at $\alpha = 0^{\circ}, 4^{\circ}$:

The time refinement study has been performed on medium mesh for the following time increments (Δt): 0.008s, 0.005s and 0.004s. It is observed that the frequency and amplitude of the aerodynamic coefficients are very close at the intervals Δt=0.005 and Δt=0.004. Therefore, Δt=0.005 is the time interval used throughout this work. (Figure 3.8, 3.9)

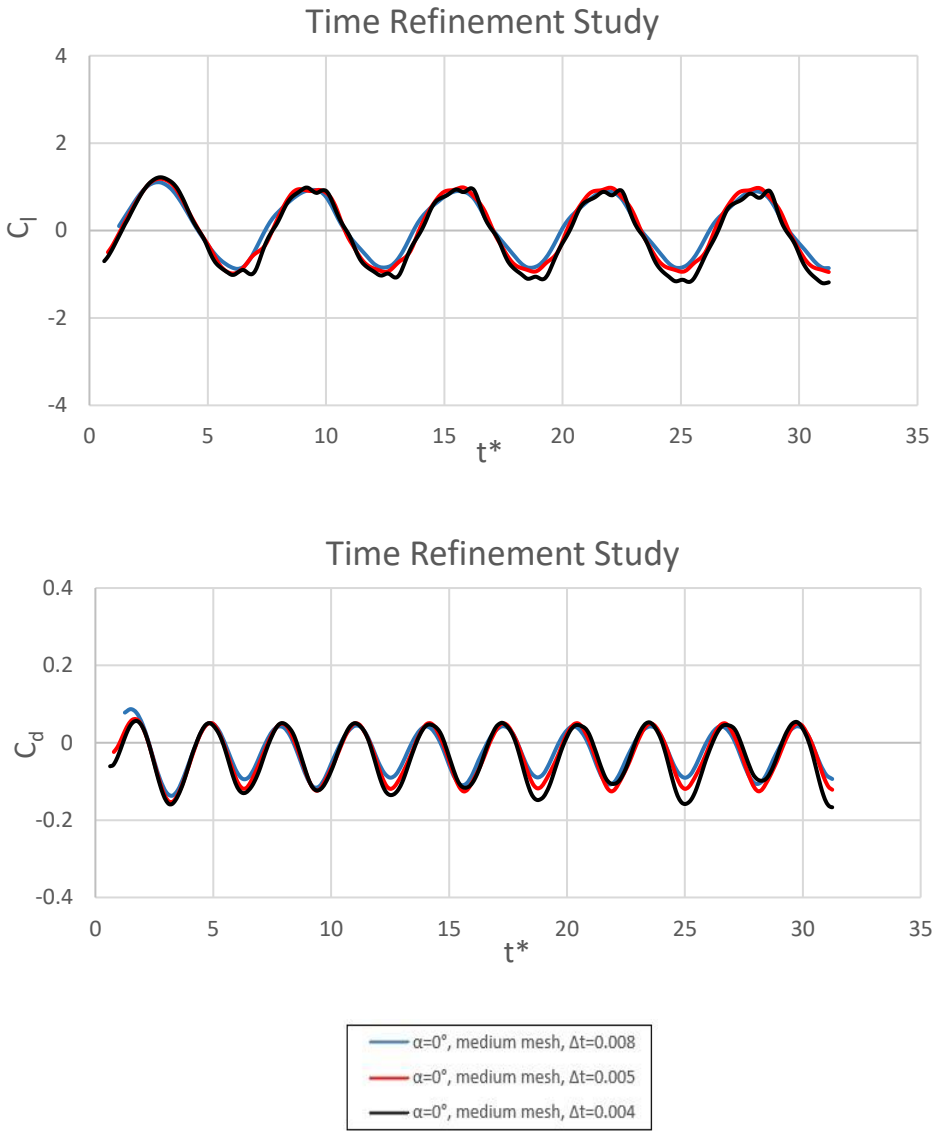

Figure 3.8: Instantaneous lift and drag coefficients for time refinement study study of NACA 0014 (pure-plunge case), $\alpha = 0^{\circ}$

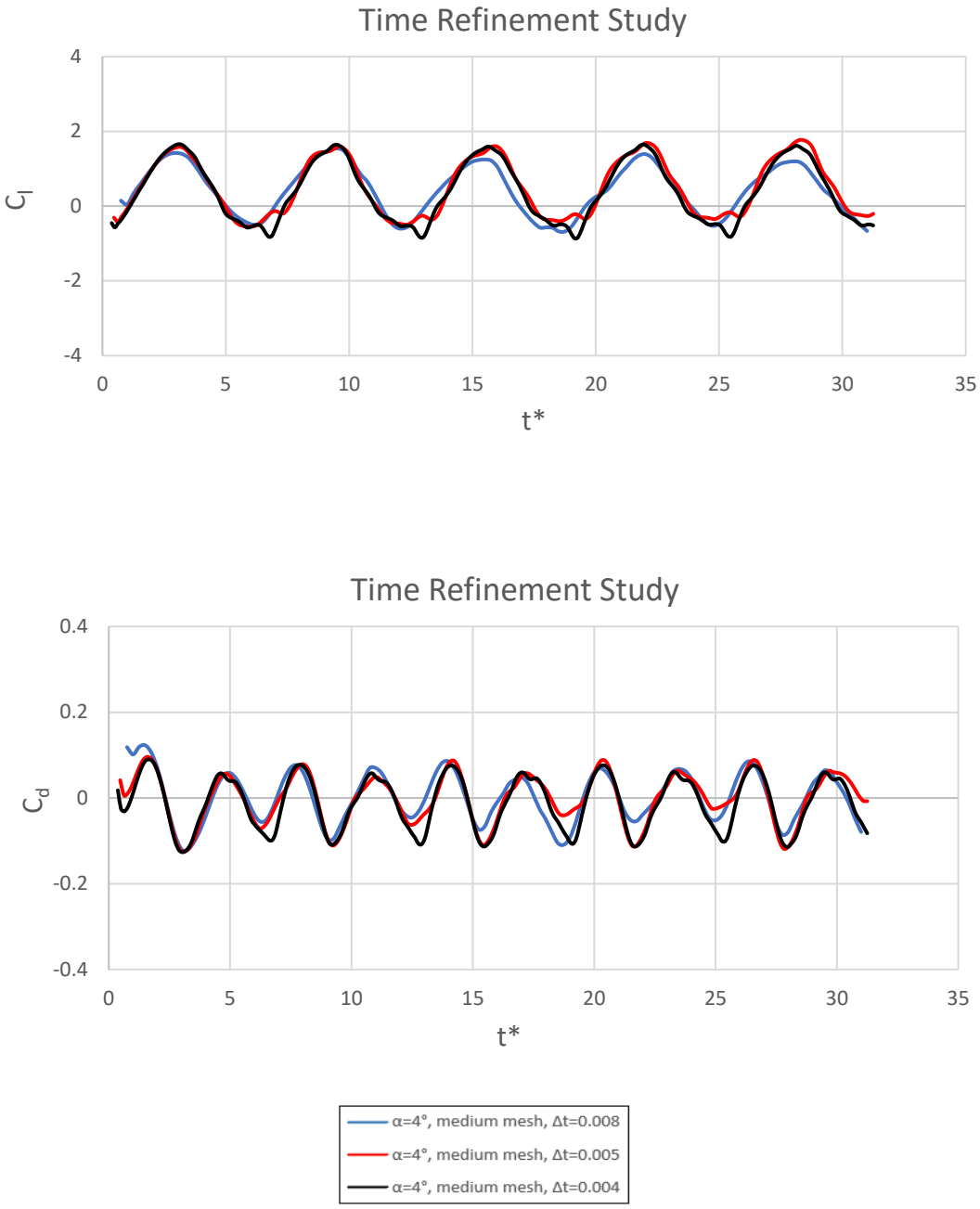

Figure 3.9: Instantaneous lift and drag coefficients for time refinement study of NACA 0014 (pure-plunge case), $\alpha = 4^{\circ}$

Grid refinement for stationary airfoil case at $\alpha = 0^{\circ}, 4^{\circ}$:

The grid refinement study clearly indicates that all three meshes have very similar aerodynamic coefficients. It is noteworthy, however, that all three meshes converge around t*=30s. Due to the small difference between the meshes, the subsequent simulations are performed using a medium mesh (Figure 3.10, 3.11).

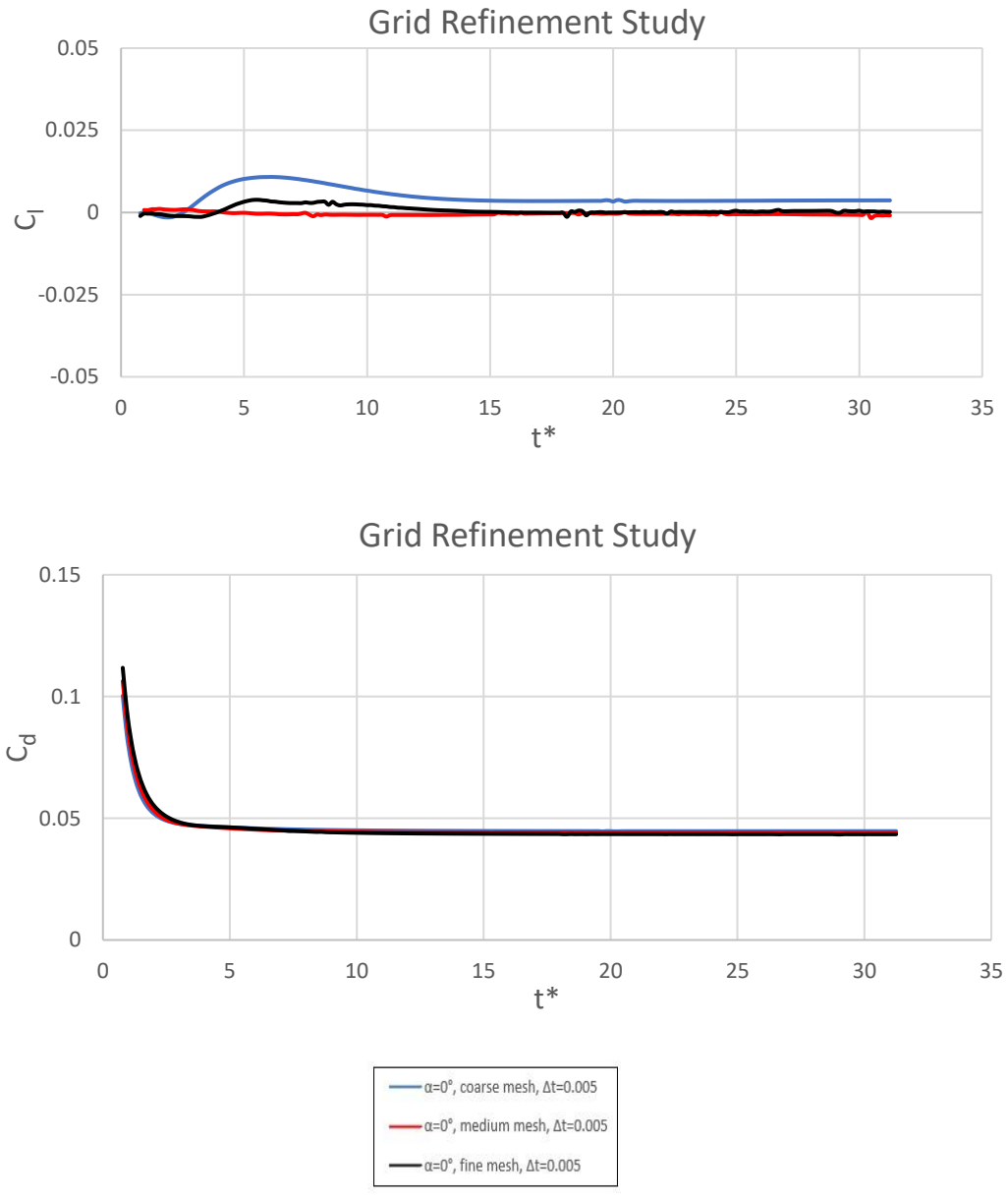

Figure 3.10: Instantaneous lift and drag coefficients for grid refinement study of NACA 0014 (stationary case), $\alpha = 0^{\circ}$

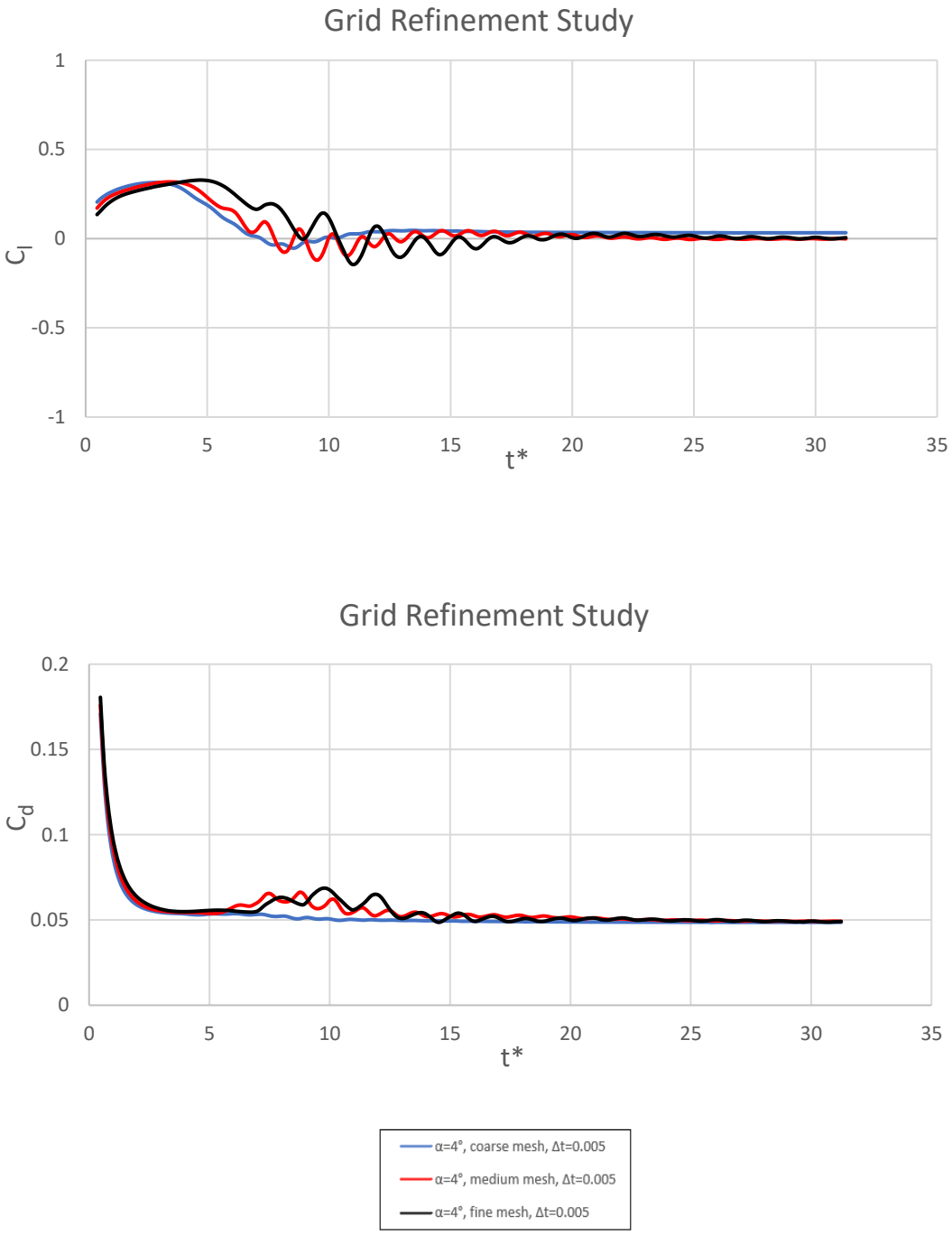

Figure 3.11: Instantaneous lift and drag coefficients for grid refinement study of NACA 0014 (stationary case), $\alpha = 4^{\circ}$

Time Refinement for stationary airfoil case at $\alpha = 0^{\circ}, 4^{\circ}$:

In this study, the time refinement study was conducted for three different time intervals on a medium mesh, namely Δt = 0.008s, 0.005s, and 0.004s. Based on the results obtained when comparing the results related to the aerodynamic coefficients at the intervals 0.005 and 0.004, we can conclude that the results are very close (Figure 3.12, 3.13). As a result, the time interval used throughout this study is Δt = 0.005s.

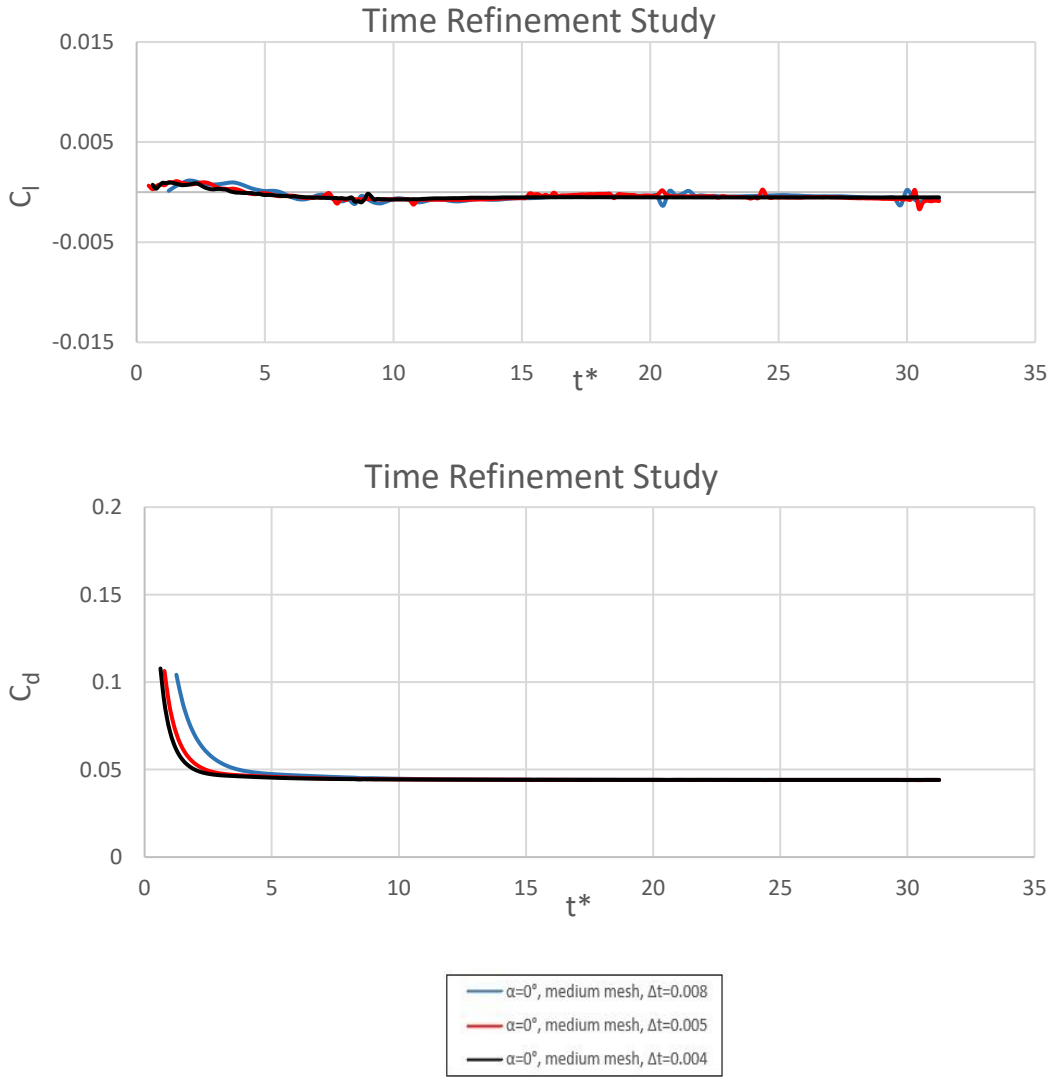

Figure 3.12: Instantaneous lift and drag coefficients for time refinement study of NACA 0014 (stationary case), $\alpha = 0^{\circ}$

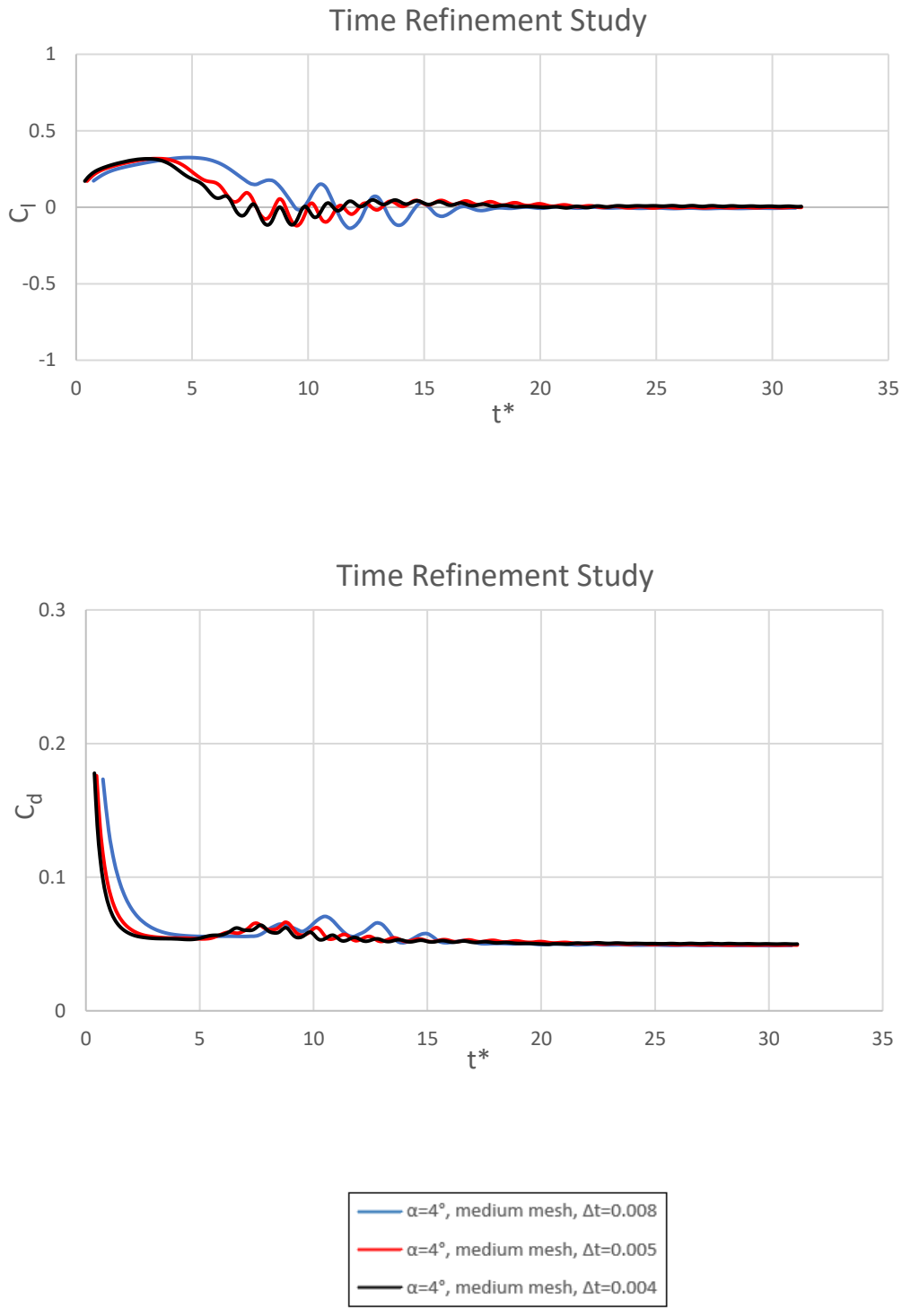

Figure 3.13: Instantaneous lift and drag coefficients for time refinement study of NACA 0014 (stationary case), $\alpha = 4^{\circ}$

3.3 Validation Study

It is necessary to conduct a validation study to verify the results of the current study. The mesh used for NACA 0012 is the same as in case of NACA 0014. The influence of Reynolds number on NACA 0012 has been evaluated through simulations at two different Reynolds numbers. Simulations of NACA 0012 at $Re = 1000$ are performed and the results are compared with those of Kurtulus [29]. Moreover, NACA 0012 is simulated at $Re = 10000$ in order to understand how Reynolds number affects the results.

In the case of NACA 0014, the results obtained from the present study are validated in accordance with findings from the study by Osama [40]. By comparing the present study with the literature review, this serves as a validation of the results of the present study.

3.3.1 Stationary NACA 0012 airfoil validation study at Re=1000

NACA 0012 in the present study is subjected to same boundary conditions and reference values as in the case of Kurtulus [29]. The mesh is the same as used for the NACA 0014. The results are simluated at two angles of attack: $\alpha = 0^{\circ}, 4^{\circ}$

Mean pressure coefficient distribution for NACA 0012 at $\alpha = 0^{\circ}, 4^{\circ}$ and Re =1000:

It is evident from Figure 3.14, that mean pressure coefficient distribution over the upper and lower surfaces of NACA 0012 airfoil at $\alpha = 0^{\circ}$ is in almost complete agreement between the present study and the literature [29].

It is observed from Figure 3.15, the computed trends in terms of mean pressure coefficient distribution over the upper and lower surfaces of NACA 0012 airfoil at $\alpha = 4^{\circ}$ of the present study are in good agreement with the literature's trends [29].

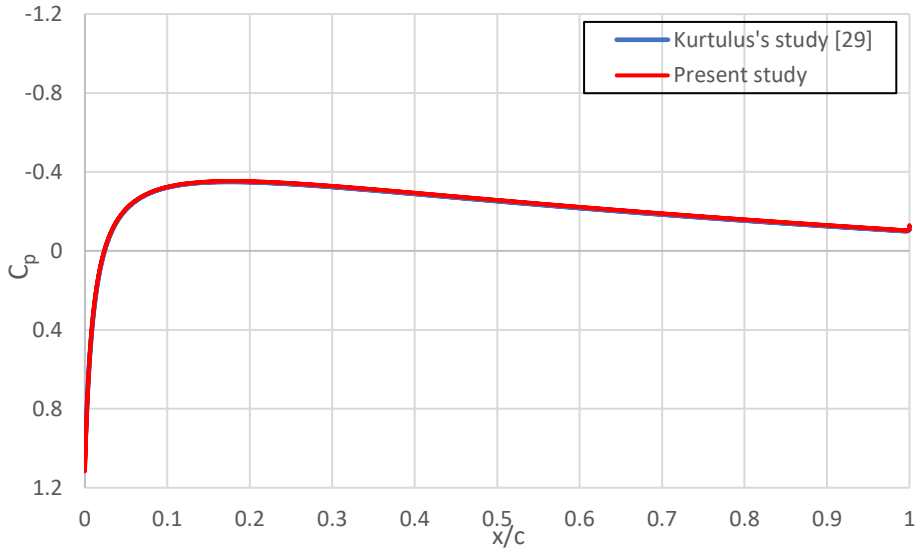

Figure 3.14: Mean pressure coefficient distribution over the upper and lower surfaces of the NACA 0012 airfoil at $\alpha = 0^{\circ}$

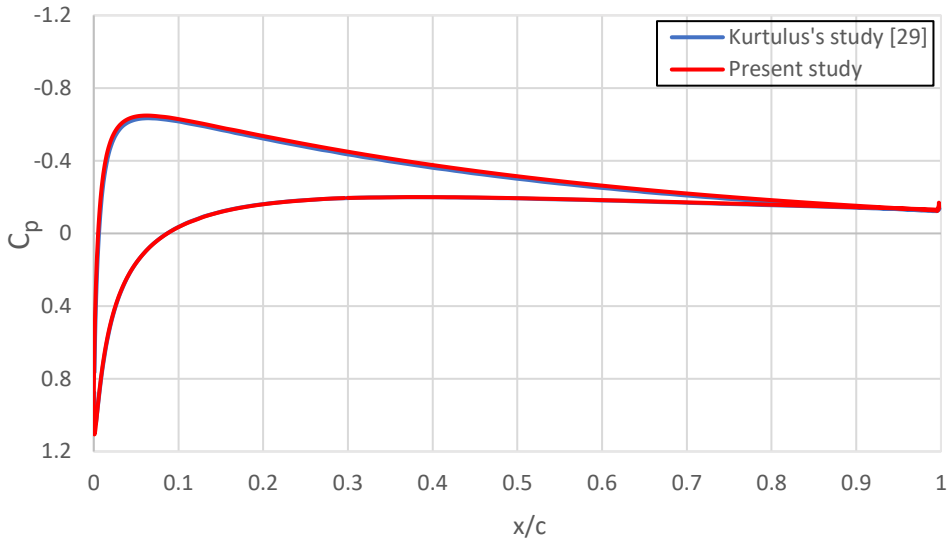

Figure 3.15: Mean pressure coefficient distribution over the upper and lower surfaces of the NACA 0012 airfoil at $\alpha = 4^{\circ}$

Mean skin friction coefficient distribution for NACA 0012 at $\alpha = 0^{\circ}, 4^{\circ}$ and $Re = 1000$:

A closer look at Figures 3.16 and 3.17 reveals that the distribution of skin friction coefficients found as a result of this study coincides in a very significant way with those found in literature. Moreover, the distribution of skin friction coefficients allows the separation point to be determined. It can be observed through the location of zero skin friction on a gradient with a negative slope. According to the result obtained for C_f, the separation point for $\alpha = 4^{\circ}$ at the airfoil's upper surface is roughly 0.8 (x/c) which is in accordance with Kurtulus [29] 's value (0.8(x/c)). (Figure 3.16)

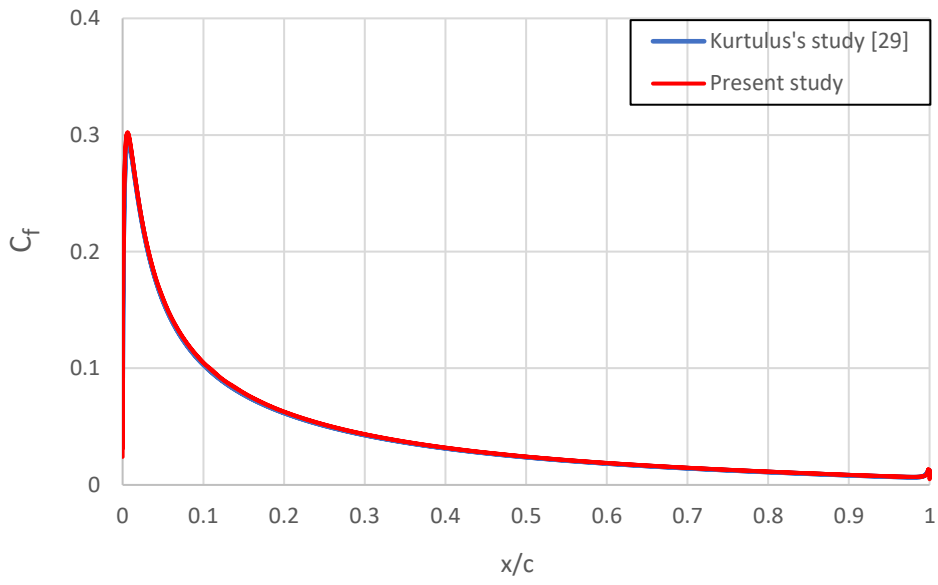

Figure 3.16: Mean skin friction coefficient distribution over the upper and lower surfaces of the NACA 0012 airfoil at $\alpha = 0^{\circ}$

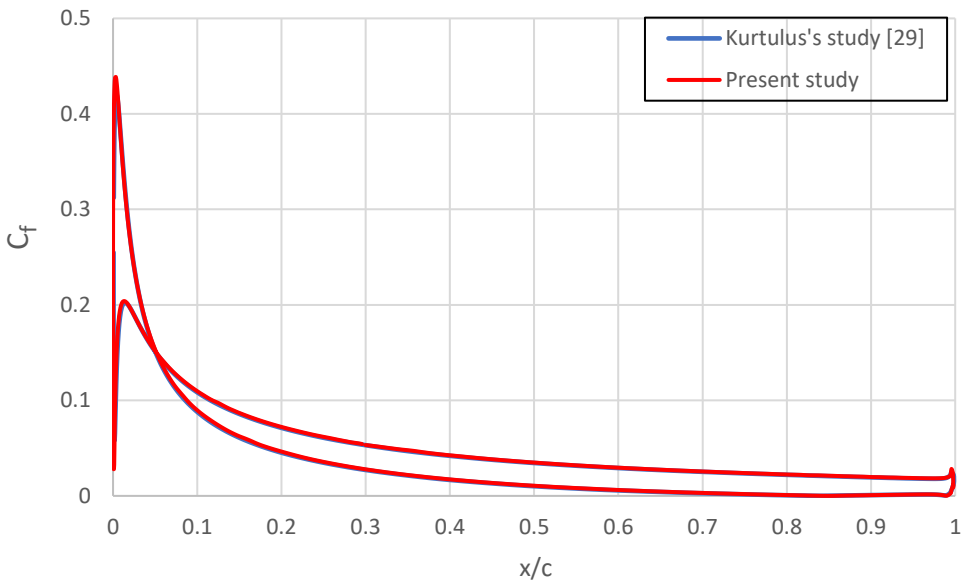

Figure 3.17: Mean skin friction coefficient distribution over the upper and lower surfaces of the NACA 0012 airfoil at $\alpha = 4^{\circ}$

3.3.2 Stationary NACA 0012 airfoil validation study at $Re = 10000$

For the purpose of validating the solution presented in this study, a comparison was made between the results of this study and the data obtained by Ilio et al. [41]. Using the Reynolds number as a parameter, Table 3.2 shows the drag coefficient values based on their relationship with the Reynolds number.

Table 3.2: Drag coefficient comparison between present study and literature data for NACA 0012 at $\alpha = 0^{\circ}$

Re	C_D		
	Present Study	HLBM [41]	XFOIL [41]
1000	0.120	0.119	0.119
10000	0.038	0.037	0.040

There is a reasonable agreement between the findings of the present study and the literature-based solutions obtained through previous studies, as shown in Table 3.2.

3.3.3 Pure-plunge NACA 0014 airfoil validation study at $Re = 10000$

In this section, pure plunge validation for NACA 0014 is computed at the two values of the reduced frequency i.e $k = 1,2$. An analysis of the present study and the literature is presented along with a detailed explanation of the results obtained in the present study.

Case 1: $k = 1$:

In this section, the flow around a single flapping wing in a pure plunge is computed. NACA 0014 is visualized at different plunge angles and compared with the results obtained by Osama et al [40]. The airfoil moves in pure sinusoidal plunging motion. There were four factors that were considered in this investigation: the plunge amplitude-to-airfoil chord ratio was 0.4, the reduced frequency of oscillation was 1.0, and the Reynolds number based on the airfoil chord fixed at 10000. Velocity and pressure contours are obtained and compared with those available in the literature (at $\alpha = 0^{\circ}$) in order to validate the present study results.

It can be seen from figures 3.18 and 3.19 that after the airfoil starts its downward stroke, the effective angle of attack of the airfoil increases ($\phi = 45^{\circ}$). With the airfoil's downward stroke, the stagnation point moves behind the leading edge to the lower surface. At the upper surface, the velocity increases causing the pressure to decrease slightly. A total of three vortices moved downstream along the lower surface, and two of them had already cleared the airfoil. Lower surface pressure is evidently greater than upper surface pressure. It must be mentioned that the plots obtained in the present study are quite in alignment with those obtained from the literature.

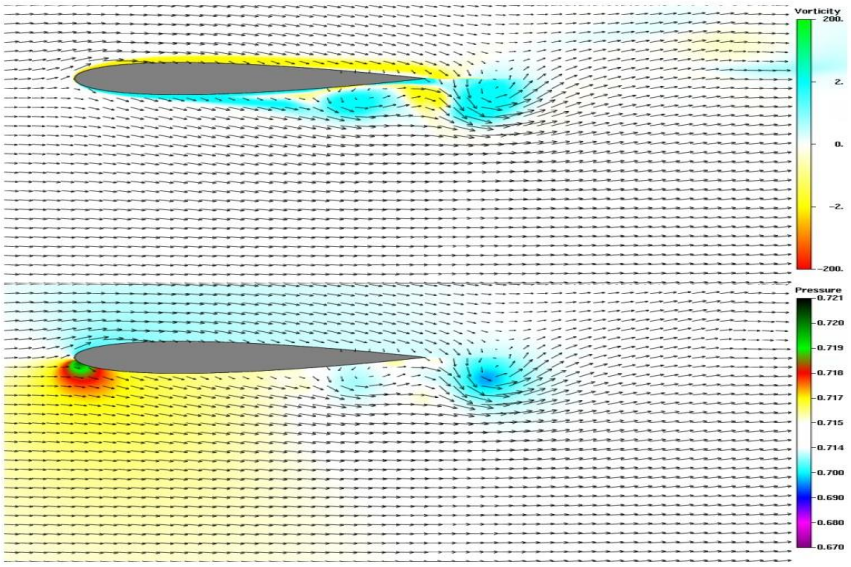

Figure 3.18: Vorticity and Pressure Around a Single Wing in Pure Plunge, NACA 0014, $\alpha = 0^{\circ}$, $M_{\infty} = 0.1$, k = 1, $Re_{\infty} = 10^{4}$, $\phi = 45^{\circ}$. [40]

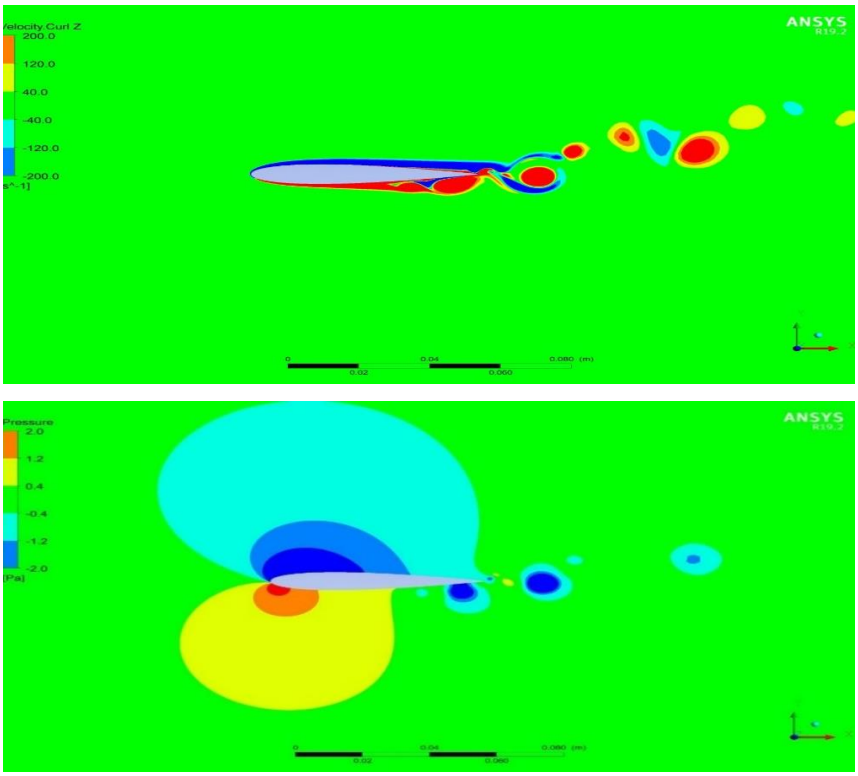

Figure 3.19: Vorticity and Pressure Around a Single Wing in Pure Plunge, NACA 0014, $\alpha = 0^{\circ}$, $M_{\infty} = 0.1$, k = 1, $Re_{\infty} = 10^{4}$, $\phi = 45^{\circ}$.

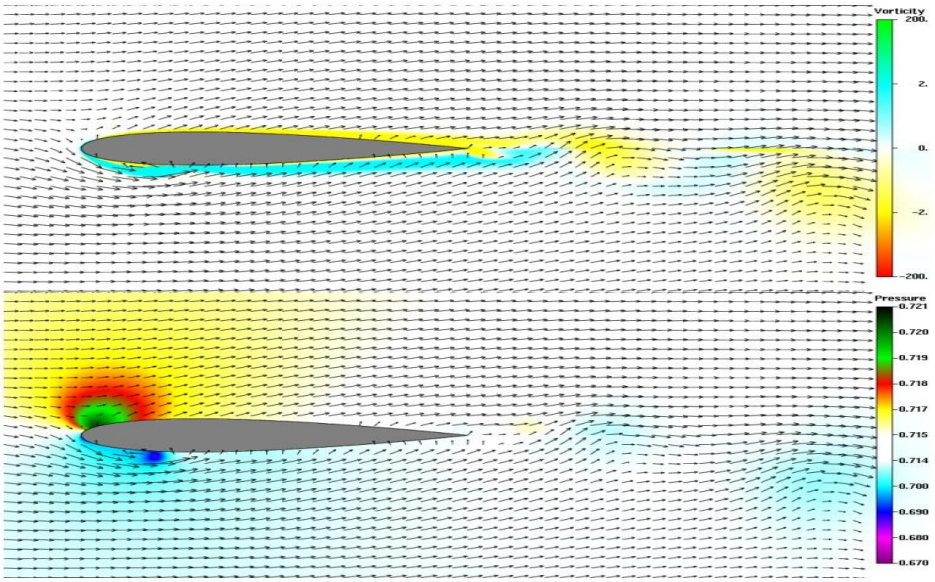

Figure 3.20: Vorticity and Pressure Around a Single Wing in Pure Plunge, NACA 0014, $\alpha = 0^{\circ}$, $M_{\infty} = 0.1$, k = 1, $Re_{\infty} = 10^{4}$, $\phi = 270^{\circ}$. [40]

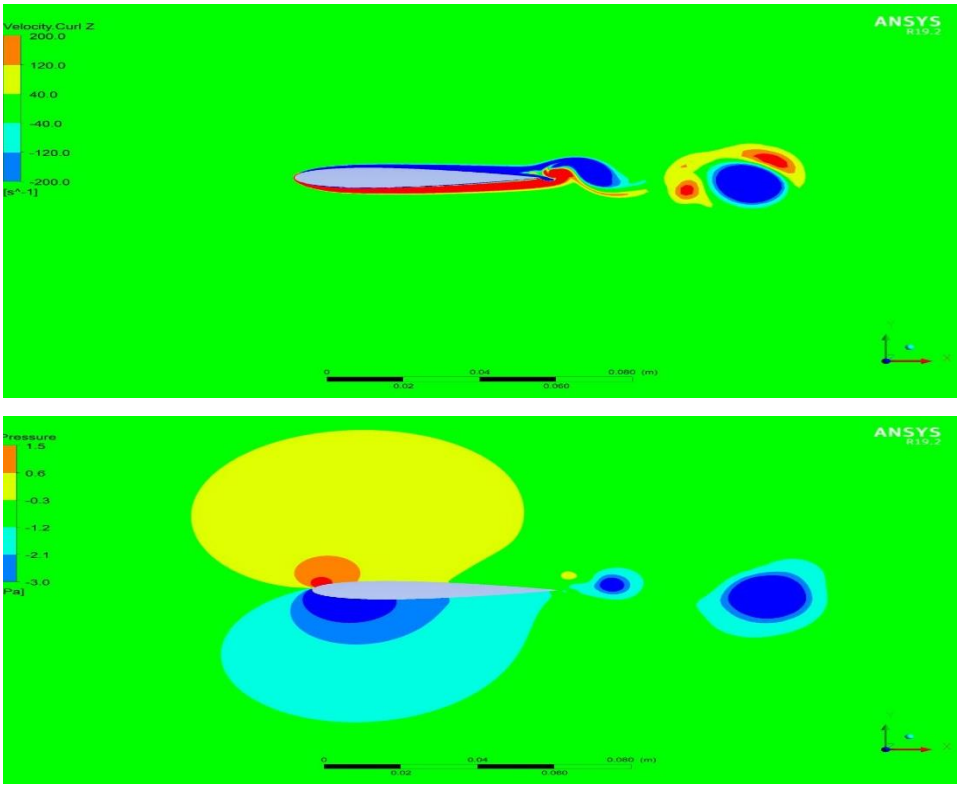

Figure 3.21: Vorticity and Pressure Around a Single Wing in Pure Plunge, NACA 0014, $\alpha = 0^{\circ}$, $M_{\infty} = 0.1$, k = 1, $Re_{\infty} = 10^{4}$, $\phi = 270^{\circ}$

During the upstroke, when the airfoil is approaching mid-flapping, $\phi = 270^{\circ}$. It is evident that in the case of Figures 3.20 and 3.21 that the negative effective angle of attack continues to increase. This results in the stagnation point on the upper surface moving downstream. Within the first quarter chord, the upper surface shows a well-developed high-pressure zone centered primarily on the stagnation point. When the lower surface's velocity increases, the pressure drops, leading to a vortex being generated and a pressure drop on the upper surface. It appears that the present study results and those found in the literature are quite similar.

Case 2: $k = 2$;

Using observations made by Tuncer et al. [58], a validation study is conducted to validate the present study. Except for the reduced frequency (k), all parameters and boundary conditions extracted from literature are the same as those used in this study. In this study, the value of k is changed from 1 to 2 because of the literature's reduced frequency. The purpose of this is to validate the present study using literature data.

A calculation of the unsteady drag coefficient is carried out at $k = 2$, and then the findings are examined and compared with what has already been published in the literature.

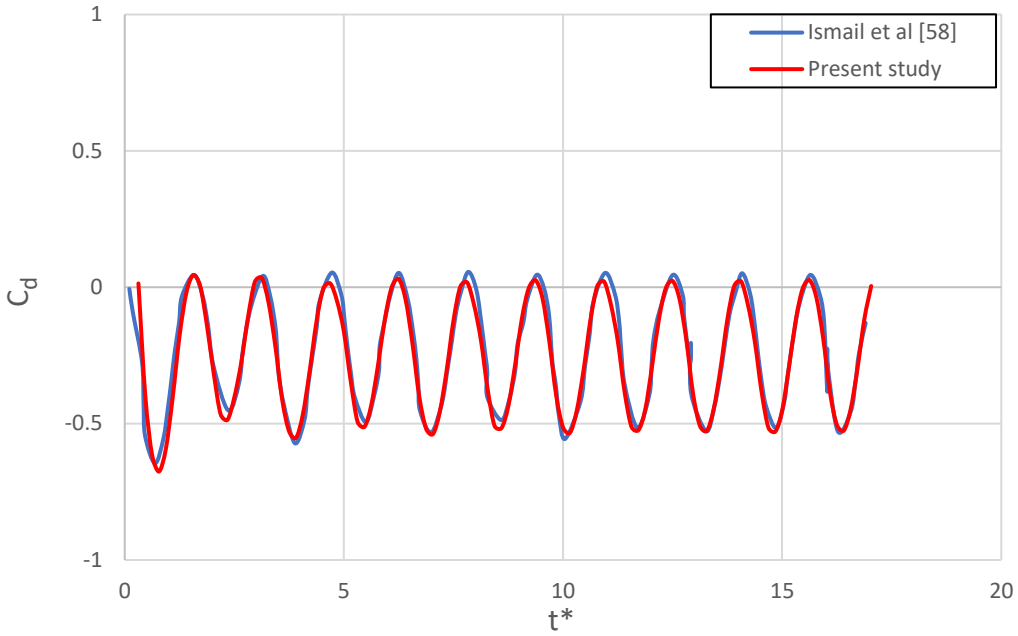

Figure 3.22: Unsteady drag coefficient computed at k = 2, h/c = 0.4, M = 0.1 and Re = 1×10^4

It can be observed from Figure 3.22 that the drag coefficient distribution calculated at $k = 2$ in the present study and the data extracted from the literature [58] are almost identical. In this way, the present study can be verified in terms of its validity.

CHAPTER 4

RESULTS AND DISSCUSSION

This section of the study analyses the effect of the thickness to chord ratio (*t/c*), effect of angle of attack (α), effect of Reynold's number (Re) and vortex shedding pattern for stationary case. Furthermore, effect of angle of attack (α), effect of Reynold's number (Re), effect of reduced frequency (k) and vortex shedding pattern is discussed for plunging case. A detailed explanation is provided for each parameter.

4.1 Effect of thickness to chord ratio (*t/c*)

An analysis of thickness to chord ratio (*t/c*) in terms of aerodynamic coefficients is presented. As far as flow parameters and reference values are concerned, they are the same for NACA 0012 as well as NACA 0014. The only difference is in the ratio of thickness to chord. The Reynolds number is the same for both configurations $(Re = 1 \times 10^4)$. In this section, we examine drag coefficient (C_d), mean pressure coefficient (C_p) and the mean friction coefficient (C_f). A comparison of these parameters is carried out from two angles of attack $(\alpha = 0^\circ, 4^\circ)$ and the trend observed is illustrated in the figures below.

It can be observed from Figures 4.1 and 4.2 that as the thickness to chord ratio increases, the drag coefficient also increase slightly. In case of $\alpha = 0^\circ$ and as well as for $\alpha = 4^\circ$ the value of drag coefficient (C_d) is slightly higher for NACA 0014 as compared to NACA 0012.

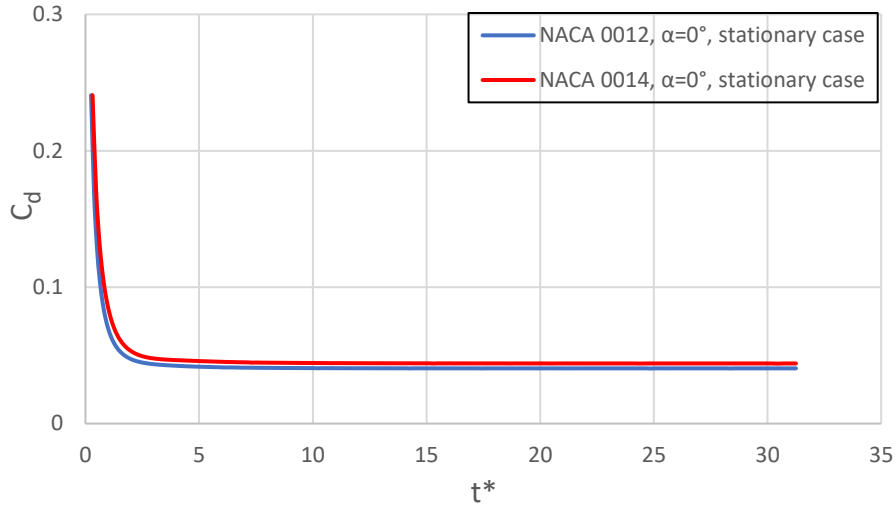

Figure 4. 1: Instantaneous lift coefficient of NACA 0012 and NACA 0014 at $\alpha = 0^{\circ}$, $Re = 1 \times 10^4$

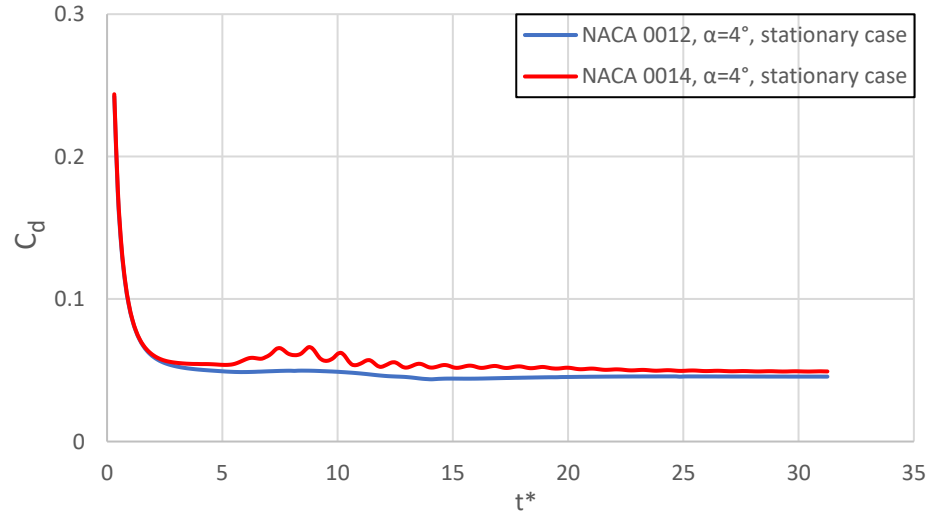

Figure 4. 2: Instantaneous lift coefficient of NACA 0012 and NACA 0014 at $\alpha = 4^{\circ}$, $Re = 1 \times 10^4$

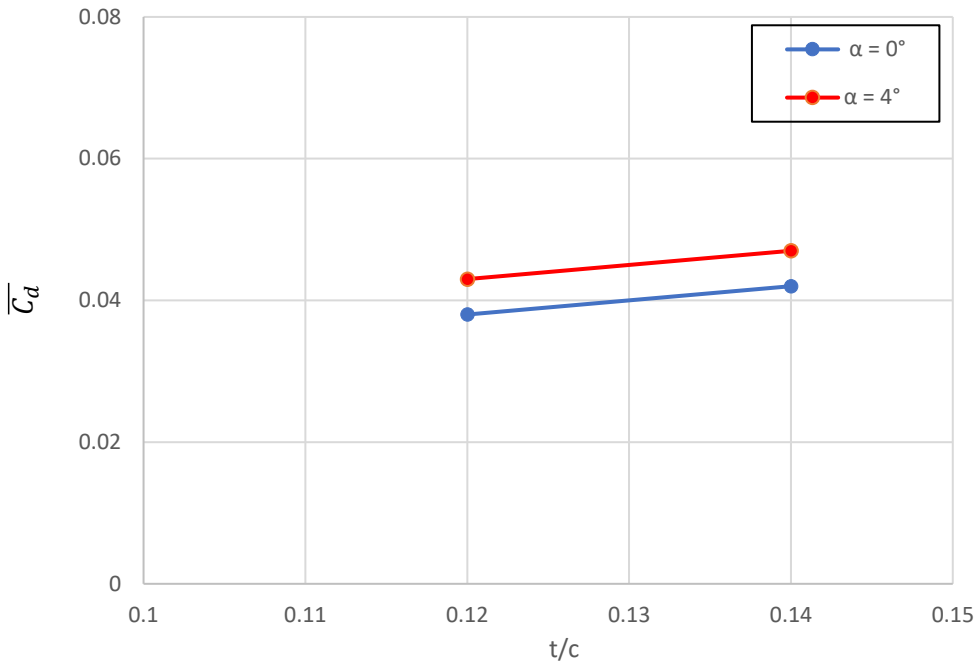

Figure 4. 3: Mean drag coefficient (C_d) for NACA 0012 and NACA 0014 at $\alpha = 0^{\circ}$& 4°, $Re = 1 \times 10^4$

For a more comprehensive and meaningful analysis of the effect of thickness to chord ratio (*t/c*) with respect to the mean drag coefficient (C_d), a comparison of $\overline{C_d}$ versus (*t/c*) is show in Fig 4.3 at $\alpha = 0^{\circ}$& 4°. It appears that as the (*t/c*) increases from 0.12 to 0.14, value of mean drag coefficient (C_d) also increases. Additionally, the value is higher in the case where the angle of attack is also greater. The value of the mean drag coefficient (C_d) for NACA 0014 is slighlty higher for both $\alpha = 0^{\circ}$ and $\alpha = 4^{\circ}$.

The mean pressure coefficient distribution trend for NACA 0012 and NACA 0014 at $\alpha = 0^{\circ}$ is quite similar when analyzed from Figure 4.4 as it is quite evident that the trends for each are quite similar. Although, as far as the leading edge and the trailing edge of the NACA 0014 are concerned, the negative pressure at both ends of the NACA 0014 is slightly higher than that observed at the leading edge an the trailing edge of NACA 0012.

Moreover, it is observed from Figure 4.5 that in the case of NACA 0012 at $\alpha = 4^{\circ}$, negative pressure at upper surface of the leading edge and positive pressure at the lower surface of the leading edge have a relatively higher value when compared to the value of NACA 0014 in terms of pressure at the upper surface and pressure at the lower surface of the airfoil.

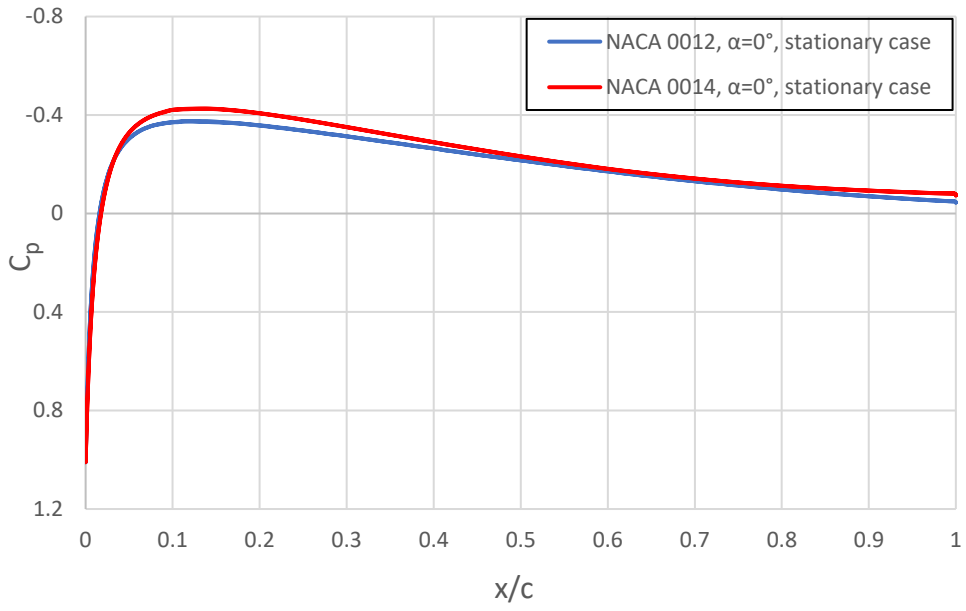

(a) Mean pressure coefficient distribution

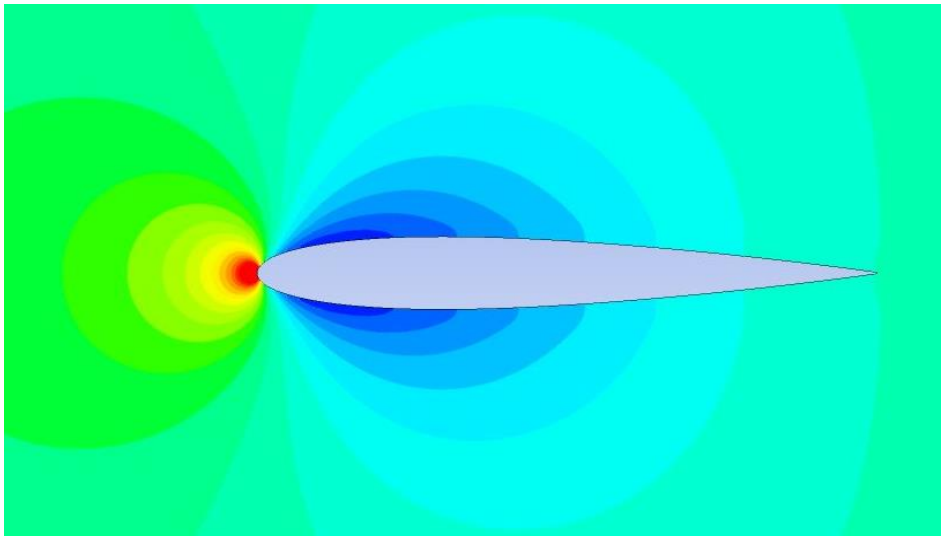

(b) Mean pressure coefficient contour of NACA 0012

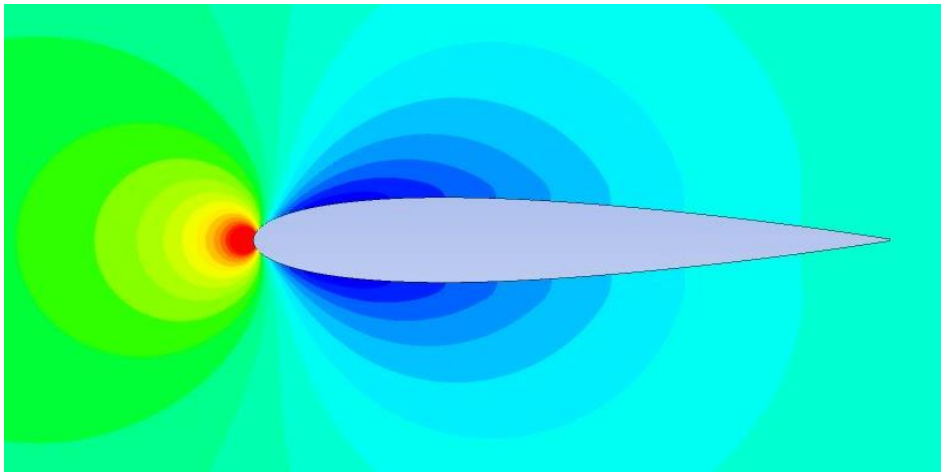

(c) Mean pressure coefficient contour of NACA 0014

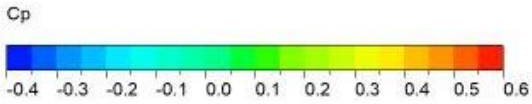

Figure 4. 4: Mean pressure coefficient distribution of NACA 0012 and NACA 0014 at $\alpha = 0^{\circ}$, $Re = 1 \times 10^{4}$

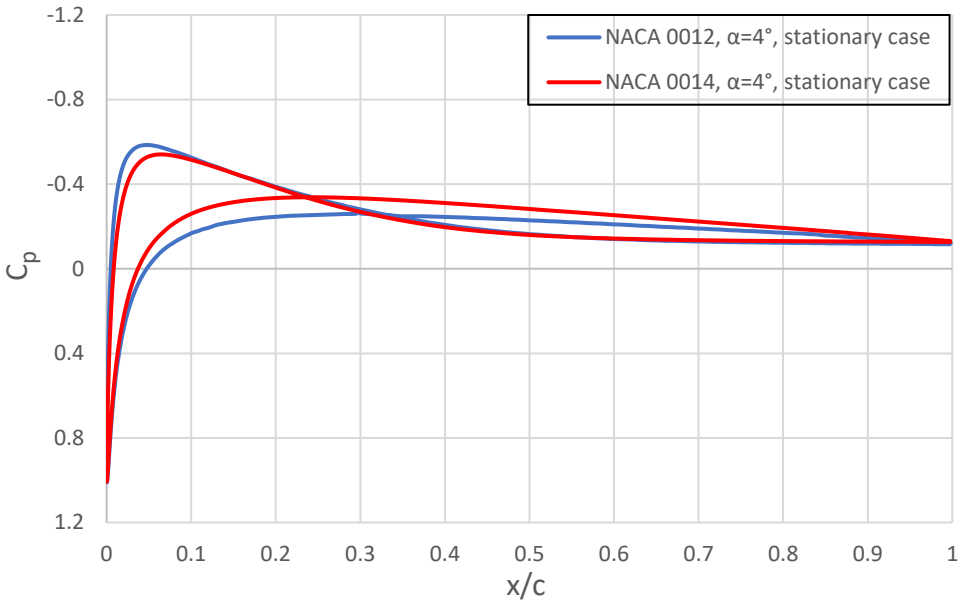

(a) Mean pressure coefficient distribution

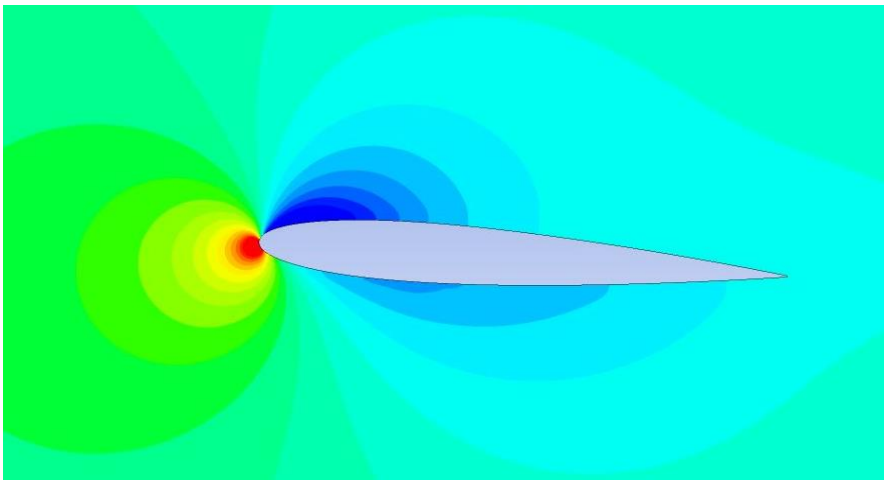

(b) Mean pressure coefficient contour of NACA 0012

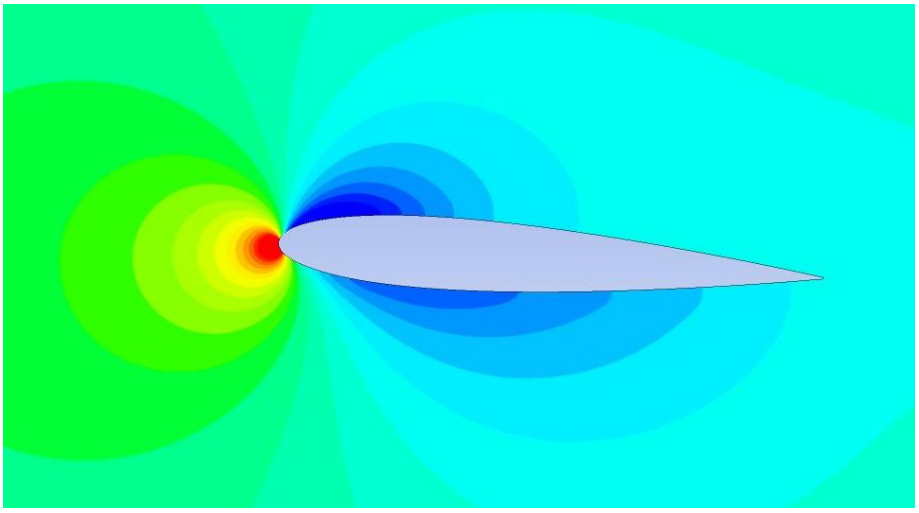

(c) Mean pressure coefficient contour of NACA 0014

(d)

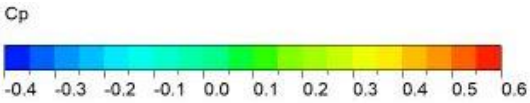

Figure 4. 5: Mean pressure coefficient distribution of NACA 0012 and NACA 0014 at $\alpha = 4^{\circ}$, $Re = 1 \times 10^{4}$

The upper surface of NACA 0012 at $\alpha = 0^{\circ}$ has a slightly higher mean skin friction coefficient than the lower surface as illustrated in Figure 4.6 (a). While NACA 0012 and NACA 0014 do have slightly different mean skin friction coefficient distributions, overall, the distributions are similar. According to the obtained results, the separation point on the airfoil's upper surface is close to 0.7 x/c in both cases. [Fig 4.6 (b) and (c)].

For NACA 0012, the mean skin friction coefficient is slightly higher at the leading and trailing edges of the lower surface at $\alpha = 4^{\circ}$ as shown in Figure 4.7 (a). Despite this, the mean skin friction distribution trend is nearly the same for both airfoil configurations. It appears from the results that the separation point is approximately 0.4 x/c at the airfoil's upper surface in both cases. [Fig 4.7 (b) and (c)].

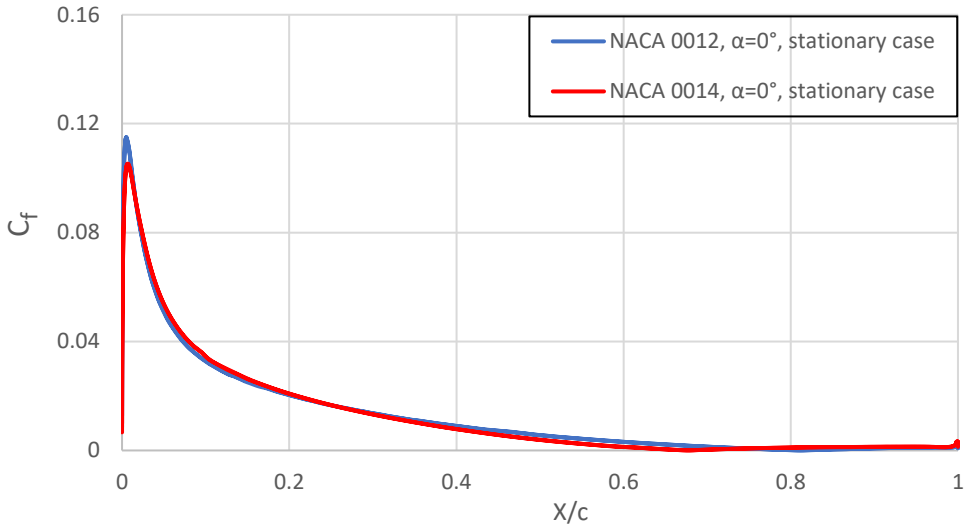

(a) Mean skin friction coefficient distribution

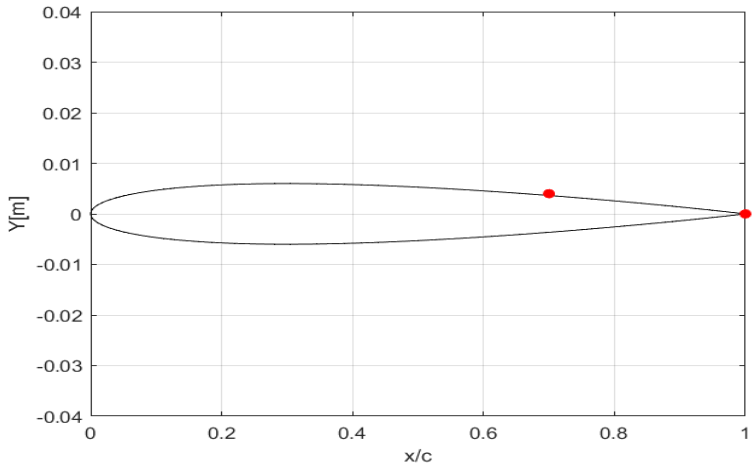

(b) Flow Separation point for NACA 0012, $\alpha = 0^{\circ}$

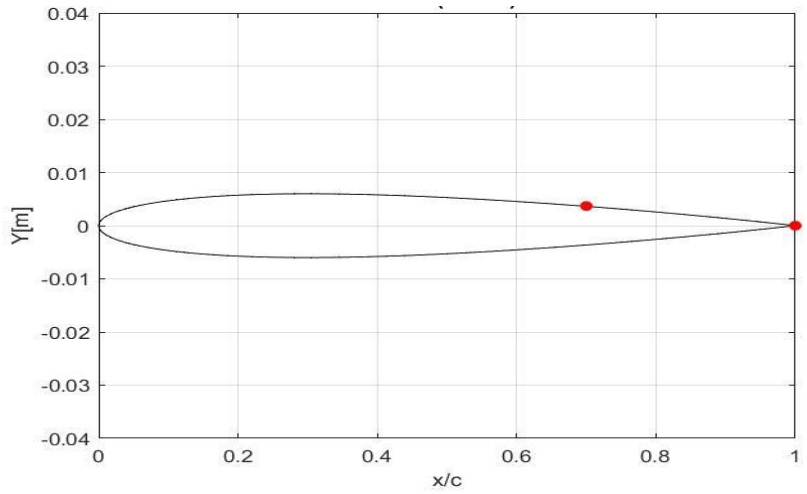

(c) Flow Separation point for NACA 0014, $\alpha = 0^{\circ}$

Figure 4. 6: Mean skin friction coefficient distribution of NACA 0012 and NACA 0014 at $\alpha = 0^{\circ}$, $Re = 1 \times 10^{4}$

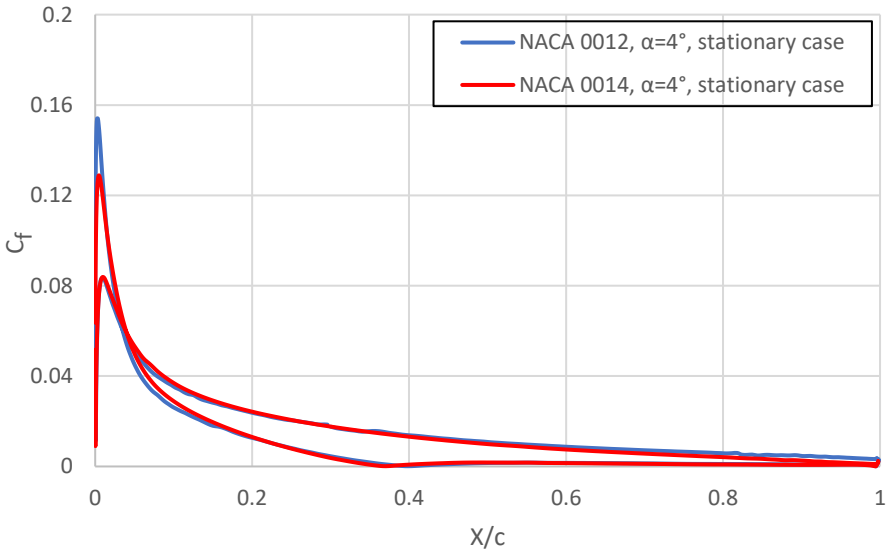

(a) Mean skin friction coefficient distribution

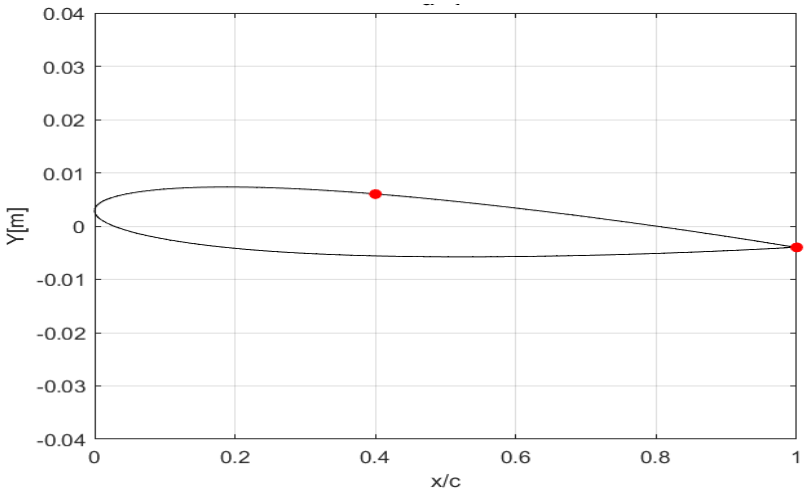

(b) Flow Separation point for NACA 0012, $\alpha = 4^{\circ}$

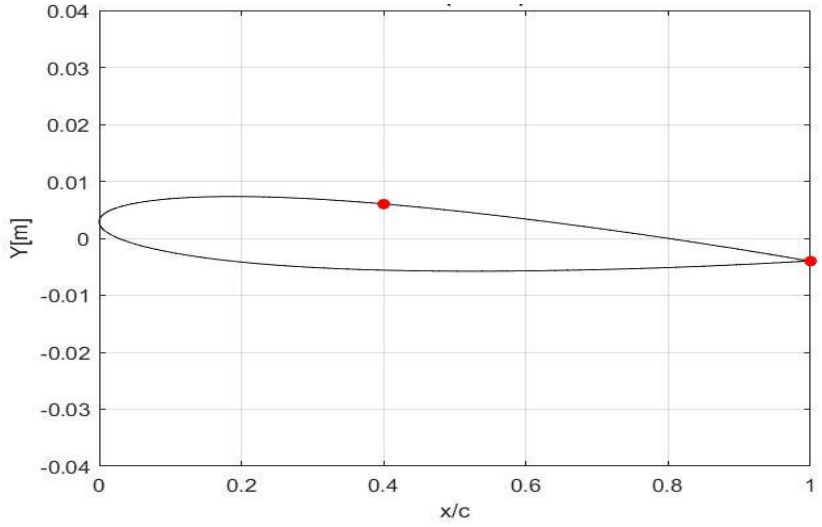

(c) Flow Separation point for NACA 0014, $\alpha = 4^{\circ}$

Figure 4. 7: Mean skin friction coefficient distribution and separation point for NACA 0012 and NACA 0014 at $\alpha = 4^{\circ}, Re = 1 \times 10^{4}$

4.2 Effect of angle of attack (α)

This section has been intended to present a concise summary of the effects that angle of attack has on certain parameters. C_l, C_d and velocity streamlines are the parameters discussed in this section. The analysis of these parameters is done for NACA 0014 in both steady-state and plunging state conditions. Additionally, effect of angle of attack is also analyzed for NACA 0012 at $\mathrm{Re} = 10^3 \& 10^4$

Based on Figure 4.8, it appears that an increasing angle of attack leads to an increase in drag coefficient at stationary state and Reynolds number, $Re = 1 \times 10^4$. Increasing the angle of attack from $0^\circ \; to \; 4^\circ$ causes the drag coefficient to rise steadily.

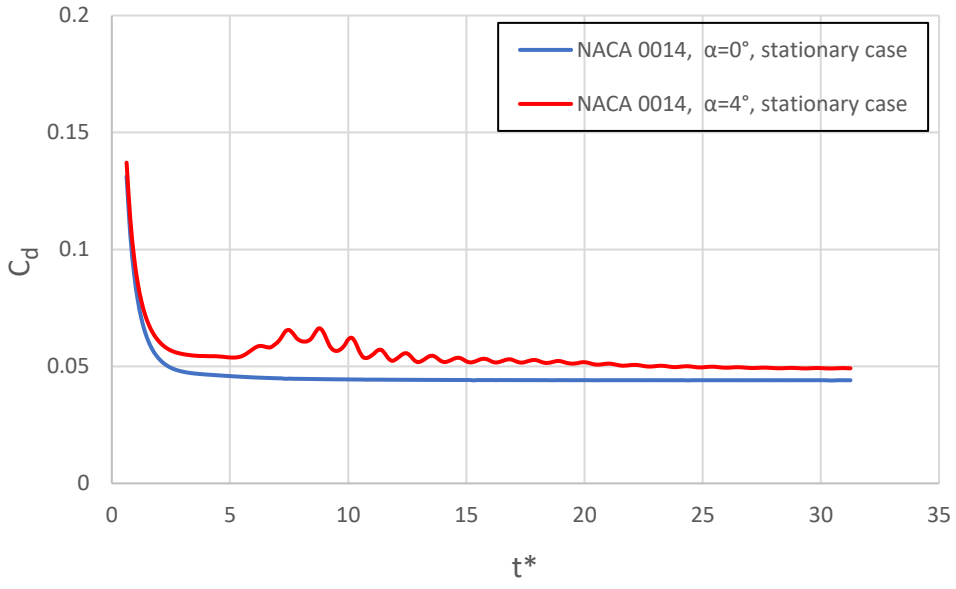

Figure 4. 8: Instantaneous drag coefficient of NACA 0014 at $\alpha = 0^\circ \& 4^\circ$, $Re = 1 \times 10^4$

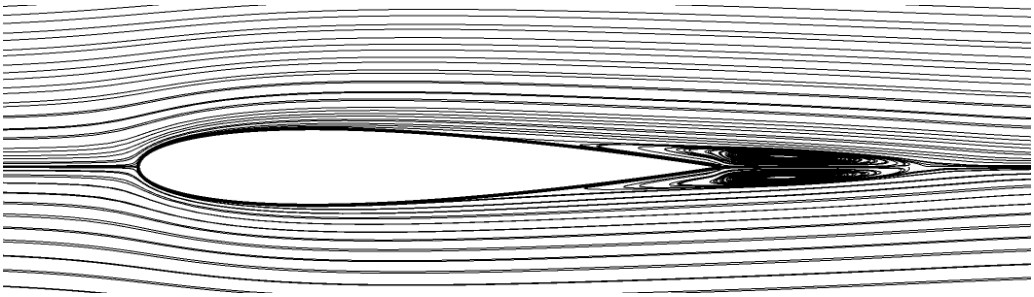

(a) $\alpha = 0^{\circ}$

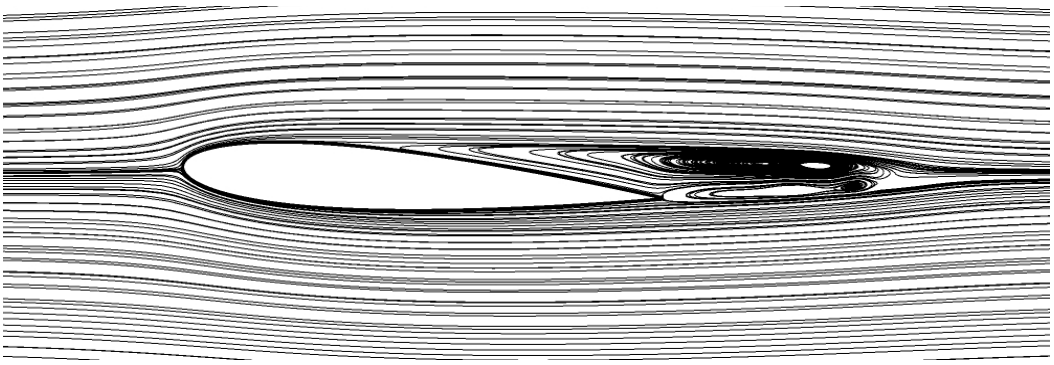

(b) $\alpha = 4^{\circ}$

Figure 4. 9: Streamlines of velocity field for angles of attack 0°& 4° for NACA 0014, $Re = 1 \times 10^{4}$

According to the Karman vortex street theory, periodic vortex shedding, a prominent feature of flow flowing past bluff bodies, characterizes flow past bluff bodies. An airfoil's flow field is characterized by a vortex structure that is determined by angle of attack. To understand these patterns, instantaneous streamlines are assessed for airfoils at $\alpha = 0^{\circ}$ and $\alpha = 4^{\circ}$ for Re = 10000 (Figure 4.9). The airfoil's trailing edge shows two counter-rotating vortices, and these vortices become more evident as you approach higher angles of attack. An increased angle of attack results in a clockwise vortex covering the upper surface of the airfoil. The separation point advances from the trailing edge towards the upper surface of the airfoil. As the angle of attack rises, the separation point shifts closer to the airfoil's leading edge. This causes an increase

in suction pressure across the upper surface both at the leading edge and trailing edge.

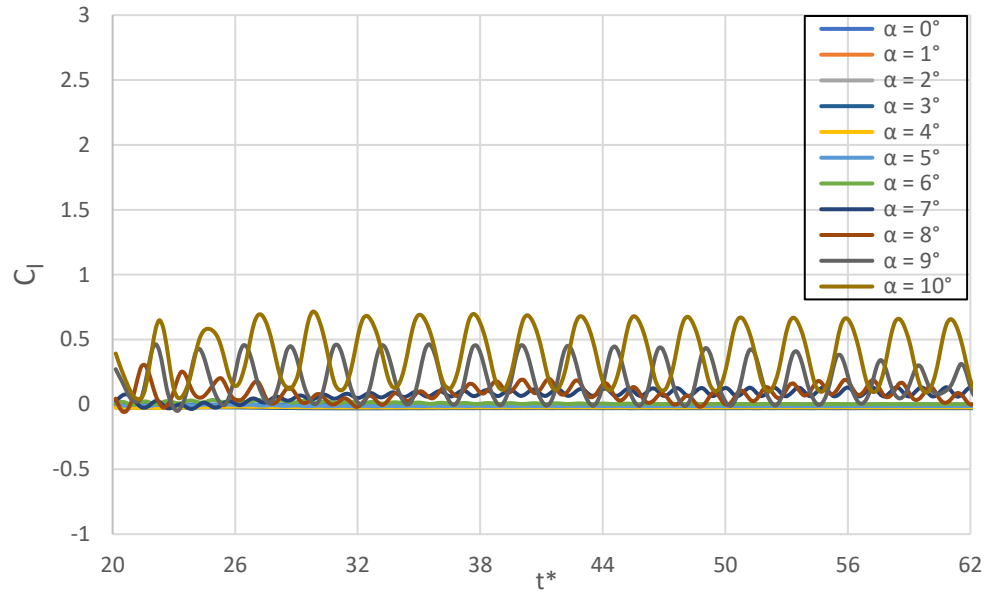

(a) Instantaneous lift coefficient

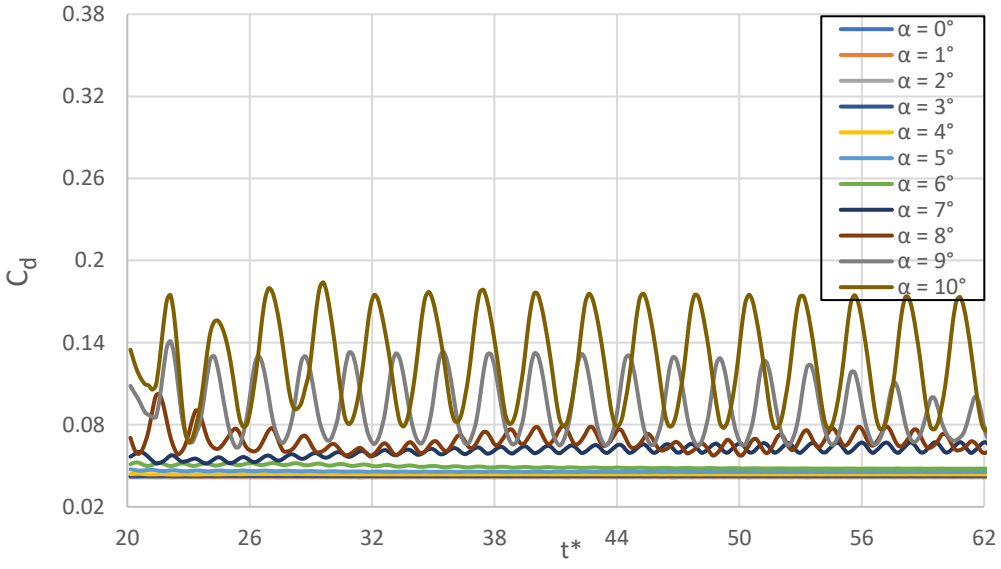

(b) Instantaneous drag coefficient

Figure 4. 10: Instantaneous aerodynamic coefficients of NACA 0014 (stationary case) at different angles of attack, $Re = 1 \times 10^4$

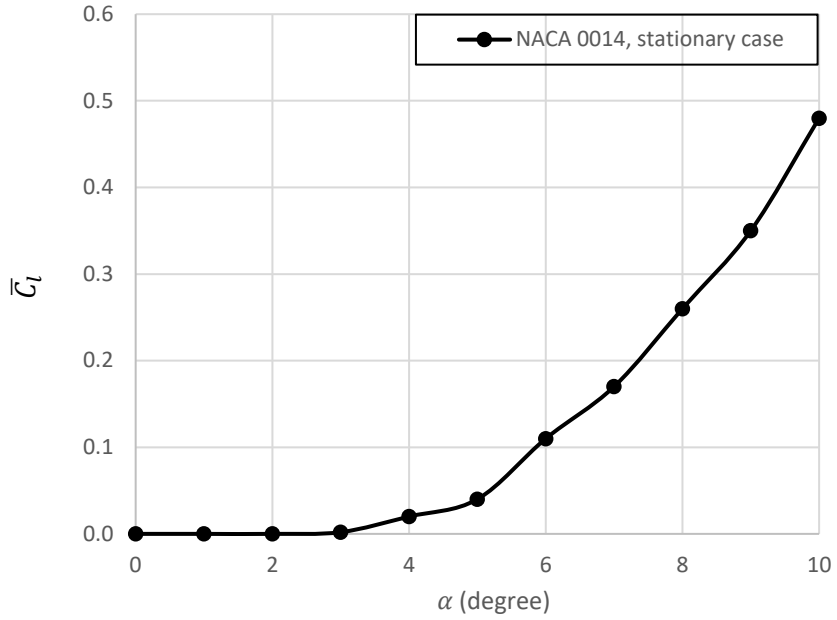

(a) Mean lift coefficient

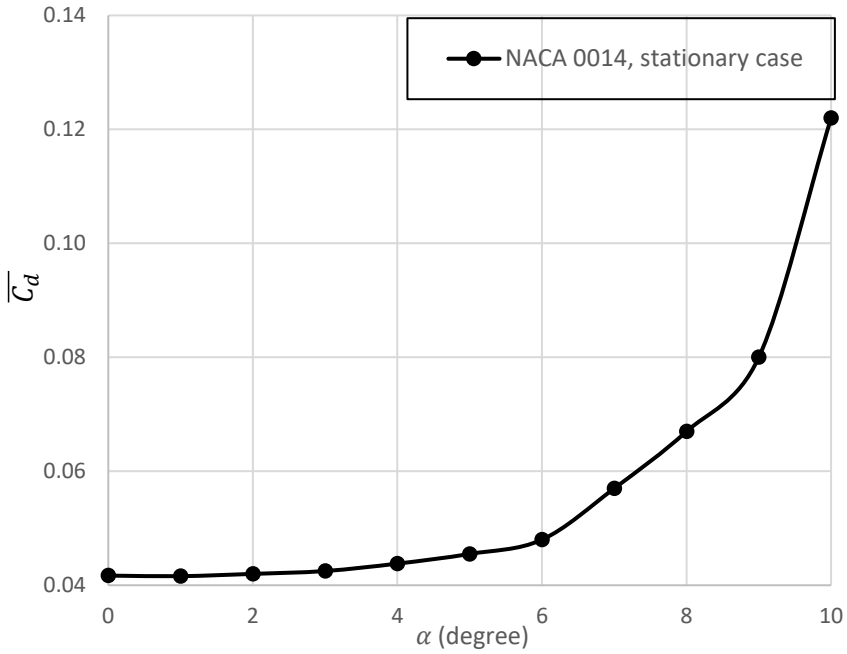

(b) Mean drag coefficient

Figure 4. 11: Mean aerodynamic coefficients of NACA 0014 (stationary case) at different angles of attack, $Re = 1 \times 10^4$

The instantaneous lift and drag coefficients versus the non-dimensional time step (t^*) for angles of attack in the range of 0° to 10° incremented by 1° are presented in Figure 4.10 for NACA 0014 (stationary case). Figure 4.10 (a) shows instantaneous lift coefficients with respect to non-dimensional time step (t^*). Solution convergence starts at t^*= 32 and continues to converge gradually thereafter. The instantaneous Cl values for angles of attack higher than 7° to 10° exhibit oscillatory dynamics. As a result, the continuous vortex shedding mode transforms into an alternate vortex shedding mode.

Furthermore, Figure 4.10 (b) presents the instantaneous Cd distribution at angles of attack in the range of 0° to 10°. A convergence is observed at t^*=32. However, oscillations are evident for angles of attack that have values above 7° to 10°.

In figure 4.11, the mean lift coefficient ($\overline{C_l}$) and mean drag coefficient ($\overline{C_d}$) are plotted at angles of attack incrementing from 0° to 10° for Re = 10000 for NACA 0014 (stationary case). An increase in angle of attack between 0° and 10° is accompanied by a progressive rise in the lift curve. It can be observed from Figure 4.11(a) with increasing angle of attack, mean lift coefficient increases too. The increase is gradual till 5˚ and from 6˚ onwards the increase is quite sharp. As $\alpha = 10^{\circ}$ approaches, the mean lift coefficient increases rapidly.

It can be observed from Figure 4.11(b) that as the angle of attack rises, the value of mean drag coefficient also rises. The increase is gradual till 5˚ and from 6˚ onwards the increase is quite sharp. As $\alpha = 10^{\circ}$ approaches, the mean drag coefficient increases rapidly.

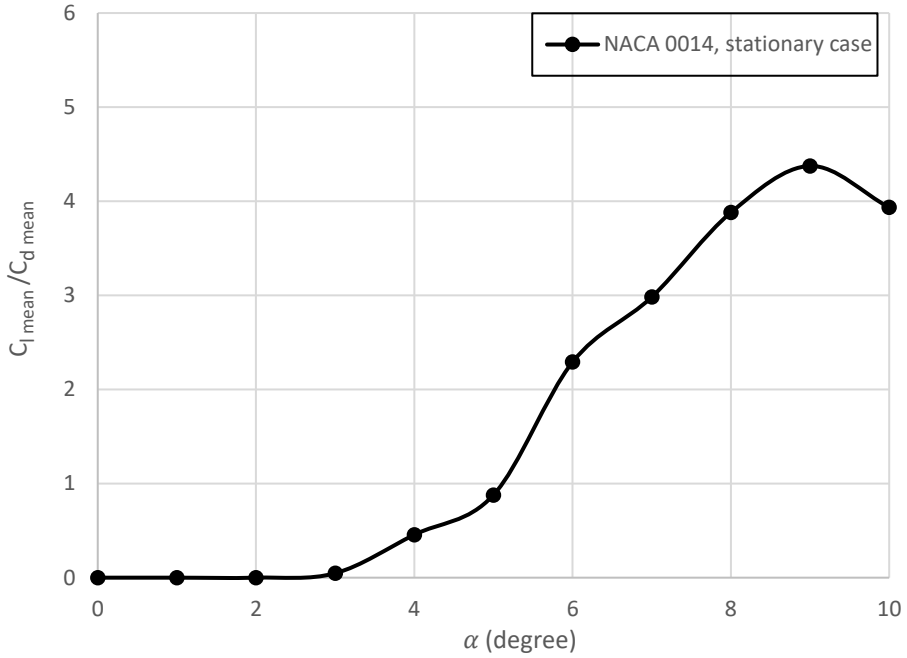

Figure 4. 12: Comparison of mean of C_l/C_d value for NACA 0014 (stationary case) at different angles of attack, $Re = 1 \times 10^4$

Considering Figure 4.12, it is easy to observe how $\bar{C}_l/\bar{C}_d$values change as the angle of attack increases. With the rise in angle of attack, mean C_l/C_d also increases gradually. The increase is quite significant from 5 degree onwards till 9 degrees. It is quite evident that the mean C_l/C_d somewhat drops at 10 degrees. Despite the fact that airfoils are subject to flow separation at higher angles of attack, this is insignificant due to a higher lift-to-drag ratio compensating for these effects.

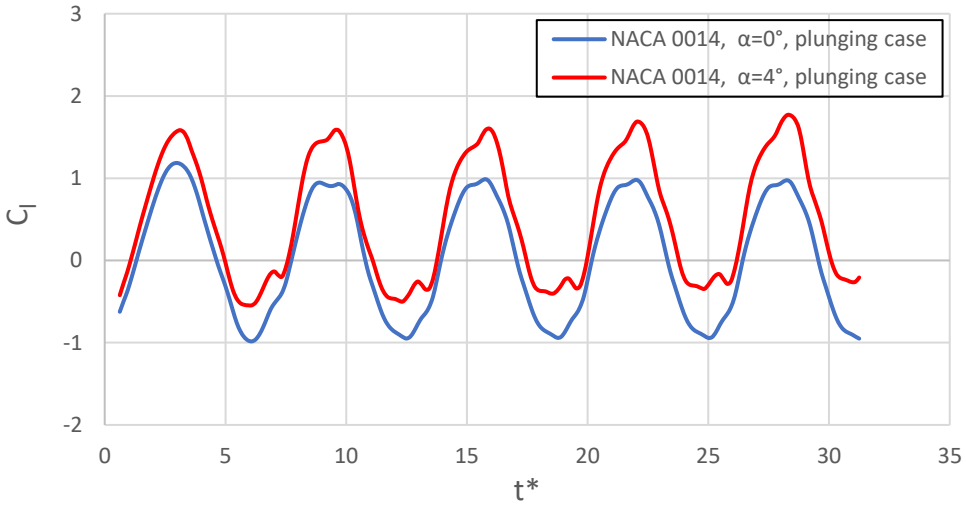

(a) Instantaneous lift coefficient

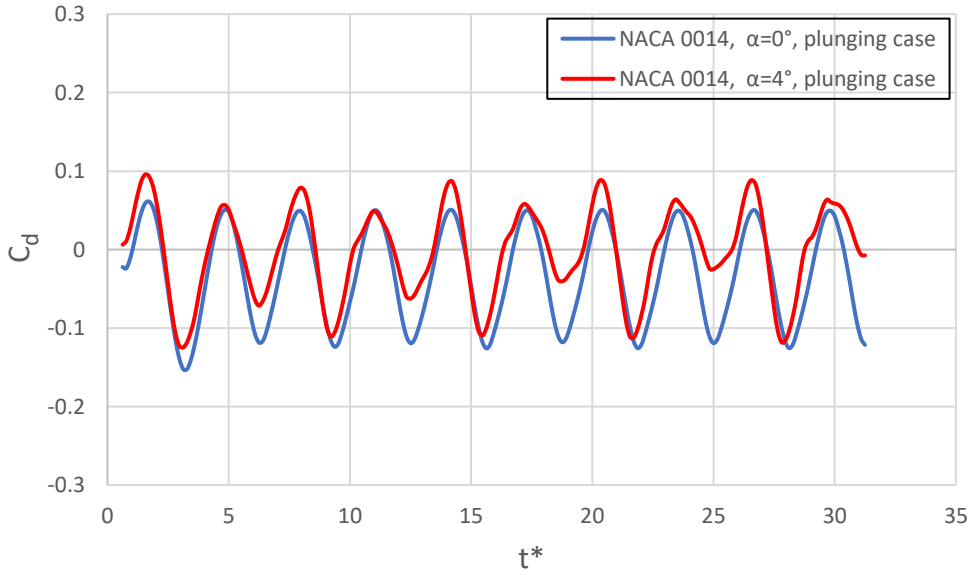

(b) Instantaneous drag coefficient

Figure 4. 13: Instantaneous aerodynamic coefficients of NACA 0014 (plunging case) at $\alpha = 0^{\circ} \& 4^{\circ}$, $Re = 1 \times 10^4$

In case of plunging motion, the instantaneous lift and drag coefficients are compared at $\alpha = 0^{\circ} and\ 4^{\circ}$, $Re = 1 \times 10^{4}$. Considering the results illustrated in Figure 4.13, it appears that the lift and drag coefficients gradually increase with increasing angle of attack from $0^{\circ} to\ 4^{\circ}$. The lift coefficient appears to rise considerably higher than the drag coefficient.

It is generally understood that thrust generation is triggered by plunging motion due to the fact that plunging produces a relative velocity that is normal to the free stream velocity. This induced velocity of an airfoil as a function of time generates an effective angle of attack, regardless of the angle of attack created by velocity. For pure plunge motion, Equation 4 shows the effective angle of attack of an airfoil with respect to time.

$$\alpha_{eff}(t) = \alpha(t) - tan^{-1}\left(\frac{h(t)}{U_{\infty}}\right) \qquad (4)$$

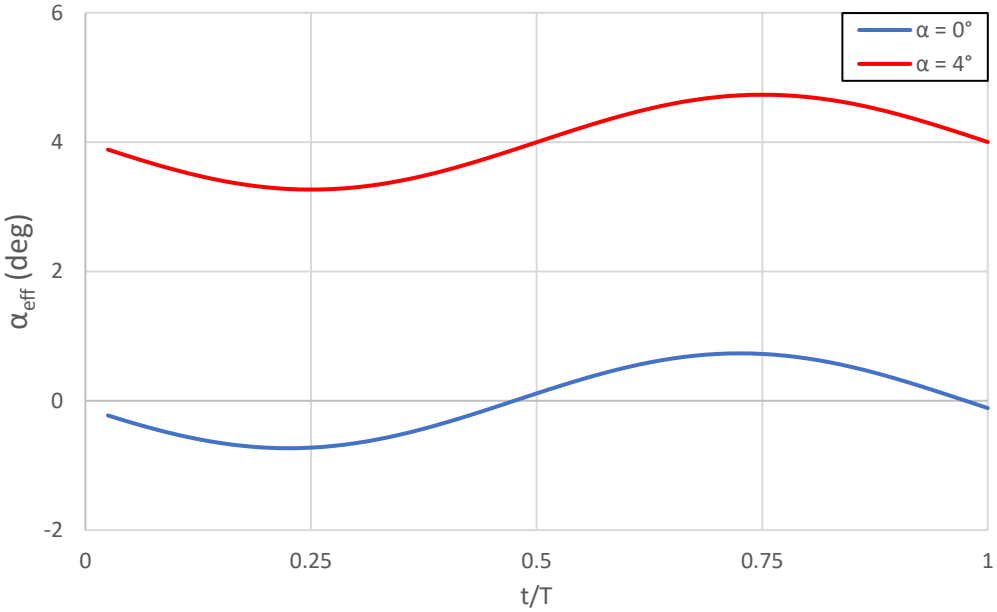

Figure 4. 14: Time histories of effective angle of attack over one period of NACA 0014 (plunging case) at $\alpha = 0^{\circ} \& 4^{\circ}$, $Re = 1 \times 10^{4}$ and $k = 1$

Figure 4.14 shows the instantaneous effective angle of attack with respect to time for the pure plunge motion of NACA 0014 at f = 5 Hz, k = 1 and Re = 10^4. The red curve represents the effective angle of attack over one time period for angle of attack, $\alpha = 4^{\circ}$. The blue curve represents the effective angle of attack over one time period for angle of attack, $\alpha = 0^{\circ}$.

In order to understand if the same path is followed by different time periods, it is necessary to look at the curves obatined by plotting mean aerodynamic coefficients as a function of effective angle of attack. The time interval taken into account is the same as considered for calculating the mean values. The curves obtained for time interval of [2s 3s] are periodic and converged.

It can be concluded that perodicity is obatined after 2s as can be seen from mean lift coefficient versus effective angle of attack curve in Figure 4.15 (a) &(c) at $\alpha = 0^{\circ}\& 4^{\circ}$. In a similar way, it can be observed that periodicity is achieved for mean drag coefficient versus effective angle of attack curve in Figure 4.15 (b) &(d) at $\alpha = 0^{\circ}\& 4^{\circ}$.

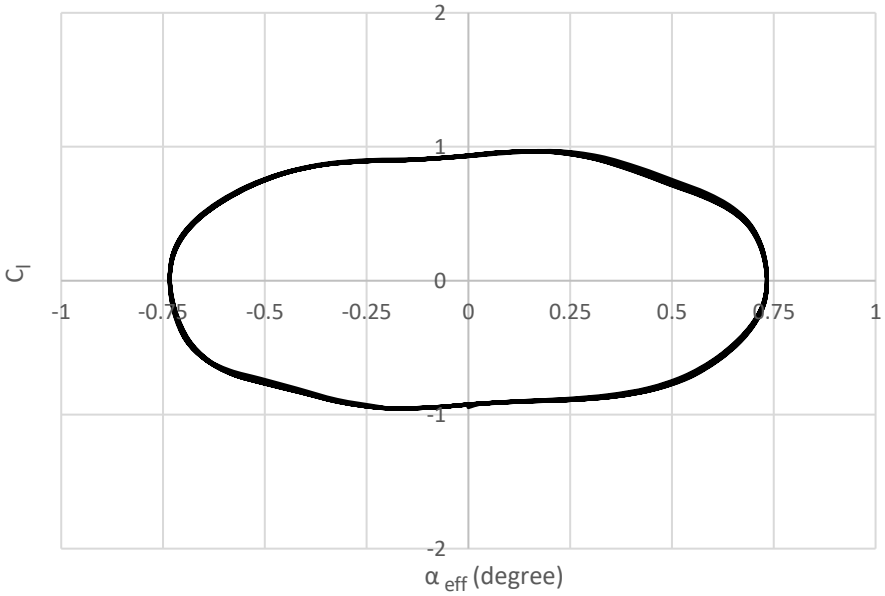

(a) Instantaneous lift coefficient vs effective angle of attack, $\alpha = 0^{\circ}$

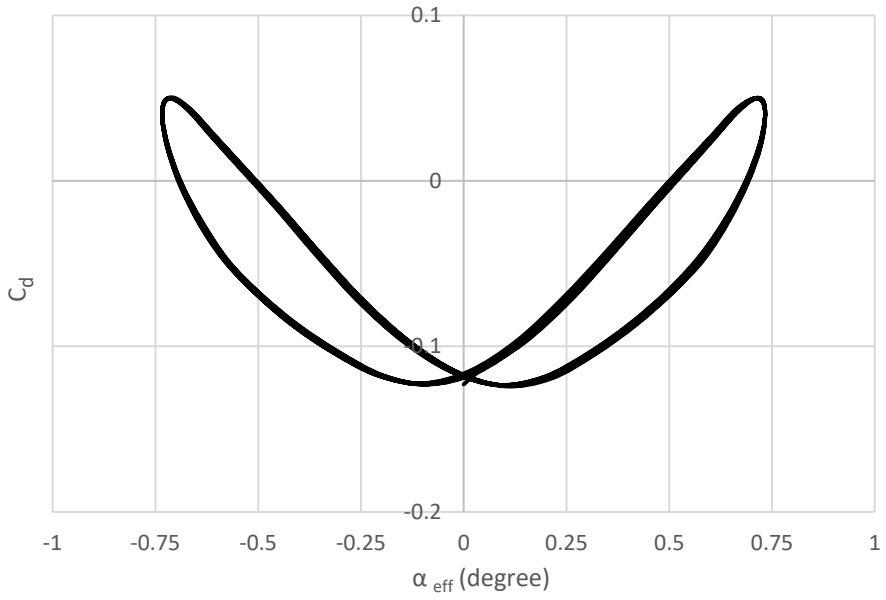

(b) Instantaneous drag coefficient vs effective angle of attack, $\alpha = 0^{\circ}$

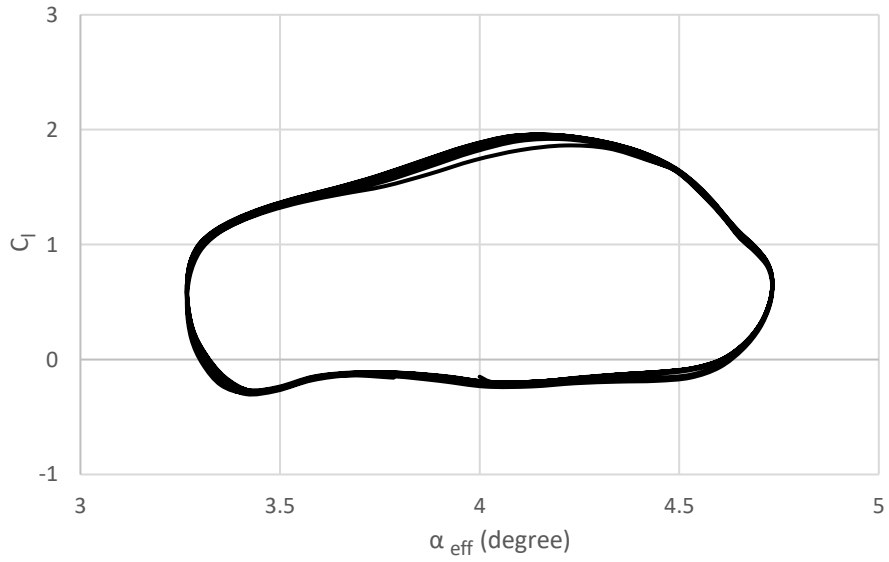

(c) Instantaneous lift coefficient vs effective angle of attack, $\alpha = 4^{\circ}$

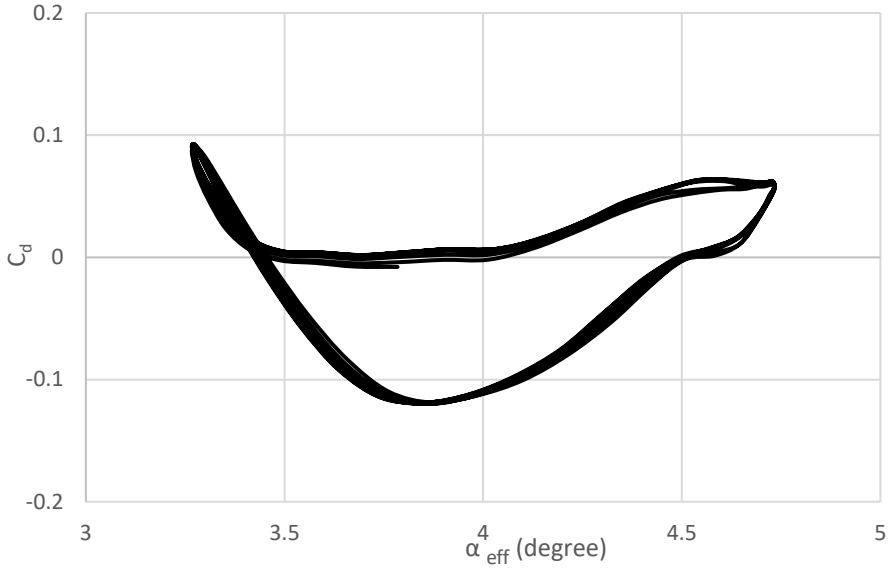

(d) Instantaneous drag coefficient vs effective angle of attack, $\alpha = 4^{\circ}$

Figure 4. 15: Instantaneous aerodynamic coefficients vs effective angle of attack of NACA 0014 (plunging case) at $\alpha = 0^{\circ}$ & 4°, $Re = 1 \times 10^4$ and $k = 1$

The comparison of mean lift and drag coefficients with respect to angle of attack can be seen in Figures 4.16 and 4.17. It is quite apparent from Figure 4.14, as the angle attack rises beginning at $\alpha = 0^{\circ}$ to $\alpha = 4^{\circ}$, the value of mean lift coefficient increases quite significantly. A closer look at Figure 4.15 leads to the observation that the trend exhibited here in this case of mean drag coefficient is comparable to the trend as observed for mean lift coefficient versus angle of attack. In case of mean drag coefficient plotted against angle of attack, the mean drag coefficient rises considerably as the angle of attack surges from $\alpha = 0^{\circ}$ to $\alpha = 4^{\circ}$.

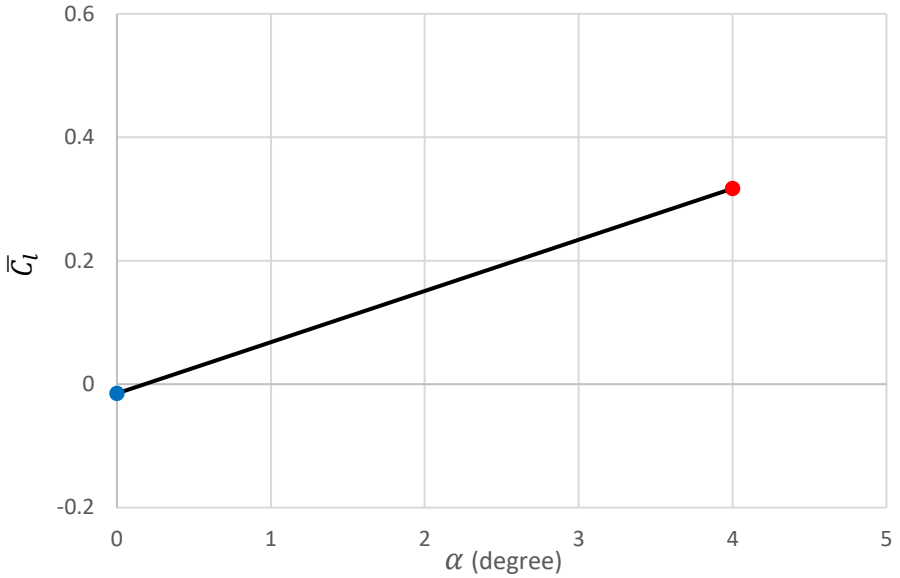

Figure 4. 16: Mean lift coefficient (C_l) for NACA 0014 (plunging case) at $\alpha = 0^{\circ}\ \&\ 4^{\circ}$, $Re = 1 \times 10^4$

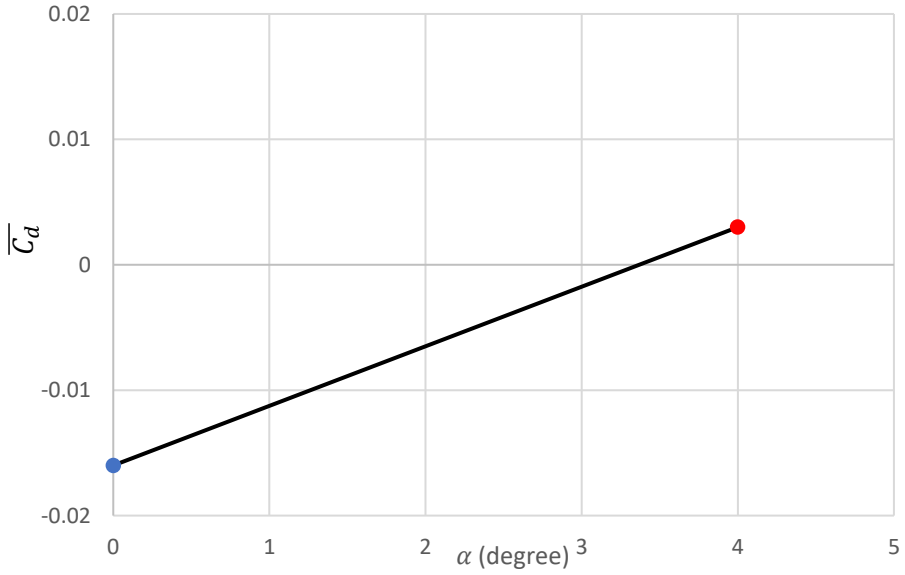

Figure 4. 17: Mean drag coefficient (C_d) for NACA 0014 (plunging case) at $\alpha = 0^{\circ}\ \&\ 4^{\circ}$, $Re = 1 \times 10^4$

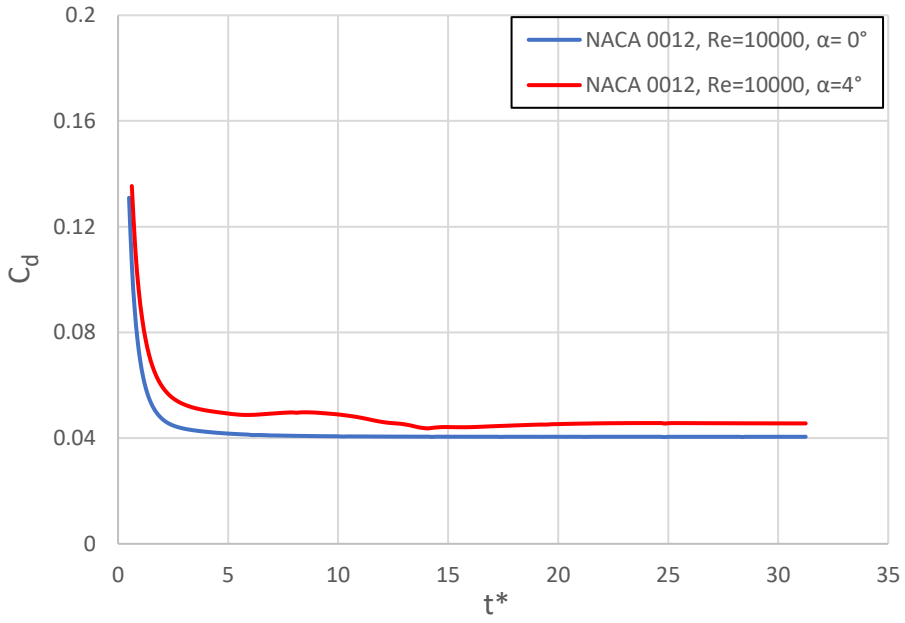

Figure 4. 18: Instantaneous drag coefficient of NACA 0012 at $\alpha = 0^{\circ}\& 4^{\circ}$, $Re = 1 \times 10^{4}$

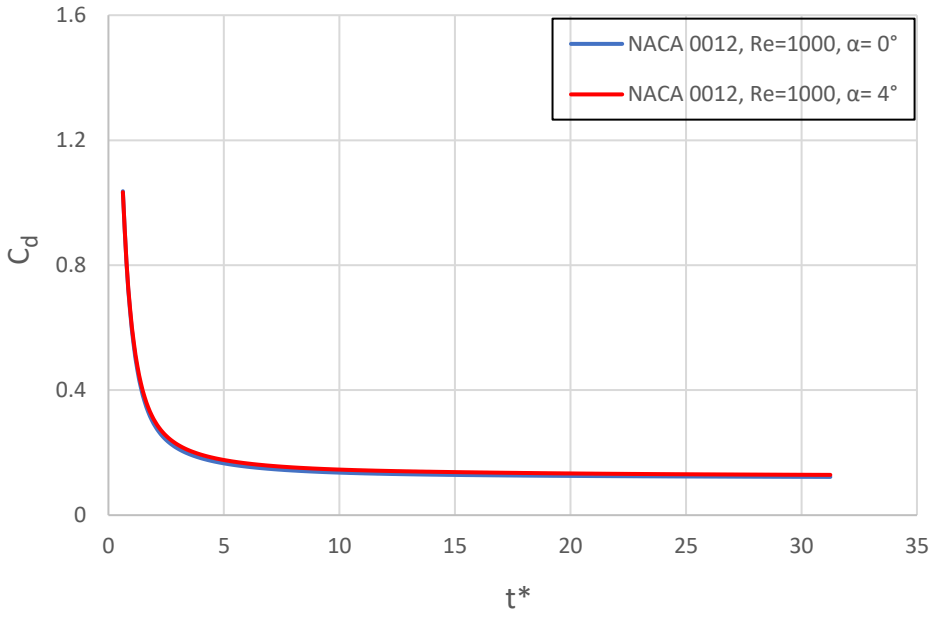

Figure 4. 19: Instantaneous drag coefficient of NACA 0012 at $\alpha = 0^{\circ}\& 4^{\circ}$, $Re = 1 \times 10^{3}$

Based on Figure 4.18, it is evident that as the angle of attack escalates, so does the drag coefficient in case of NACA 0012, stationary case and Reynolds number, $Re = 1 \times 10^4$. A steady surge in drag coefficient is observed with the elevation in angle of attack from $0^\circ \; to \; 4^\circ$.

It is clear from Figure 4.19, that the drag coefficient distribution is almost the same with the increase in angle of attack increases from $0^\circ \; to \; 4^\circ$ for NACA 0012 at steady-stationary condition and Reynolds number, $Re = 1 \times 10^3$. Nonetheless, the drag coefficient is slightly higher for $\alpha = 4^\circ$ than for $\alpha = 0^\circ$.

4.3 Effect of Reynolds number

The results obtained using two separate Reynolds numbers, namely 1000 and 10000, are presented in this section for comparison and discussion. For the two Reynolds numbers discussed above, the coefficients of mean pressure and mean skin friction are discussed for two distinct angles of attack ($\alpha = 0^{\circ}$ & 4°) at two different Reynolds numbers.

Figure 4.20 shows that the pressure coefficient decreases significantly as Reynolds number increases $(Re = 10000)$ compared to $Re = 1000$ as Reynolds number increases. As can also be observed, the difference between the pressure coefficient distribution at $Re = 1000$ and $Re = 10000$ and is pretty low at $\alpha = 0^{\circ}$ However, the difference is significant and visible at $\alpha = 4^{\circ}$ between $Re = 1000$ and $Re = 10000$.

It can be observed for $\alpha = 0^{\circ}$ that the negative pressure is slighlty higher for Re = 10000 in the vicinity of the leading edge but the the negative pressure is higher for Re = 1000 towards the trailing edge. In case of $\alpha = 4^{\circ}$, it can be observed for Re = 1000 that the upper surface has higher negative pressure distribution and the lower surface has higher positive pressure distribution. However, for Re = 10000 the upper surface has lower negative pressure distribution when compared to Re = 1000. The lower surface has lower positive pressure distribution for Re = 10000.

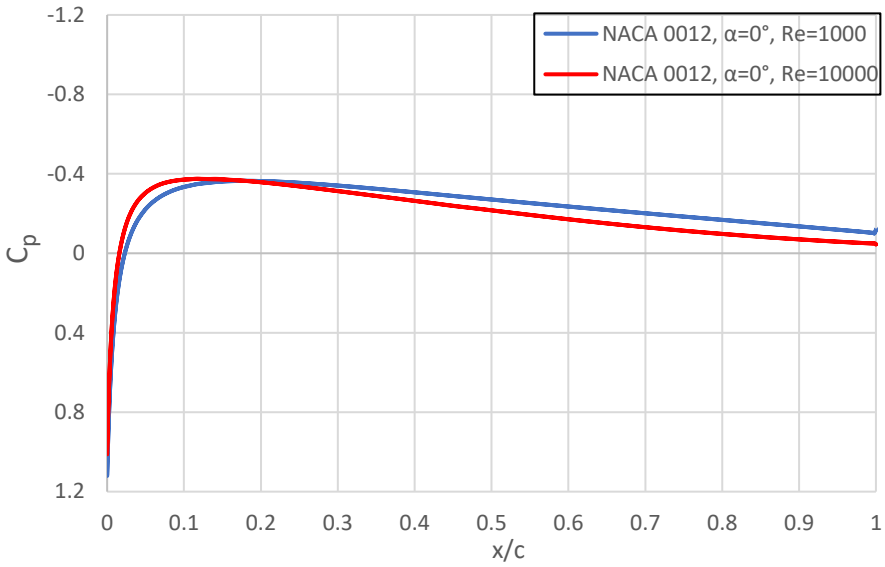

(a) $\alpha = 0^{\circ}$

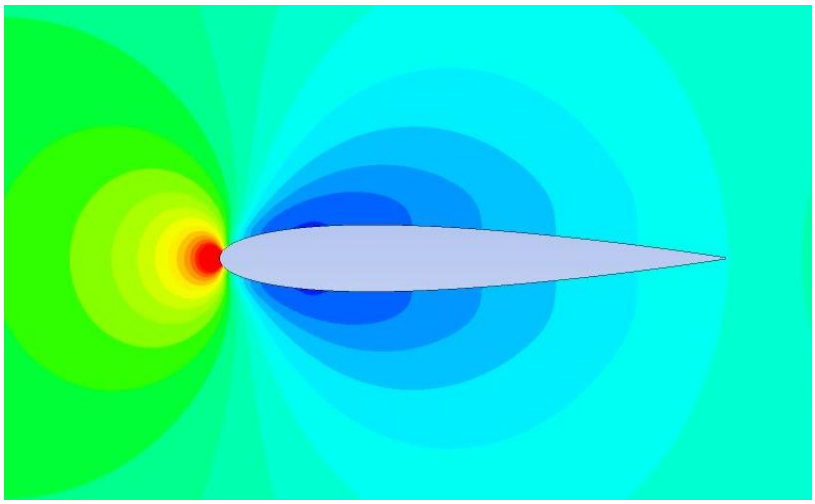

(b) Mean pressure coefficient contour of NACA 0012, Re = 1000

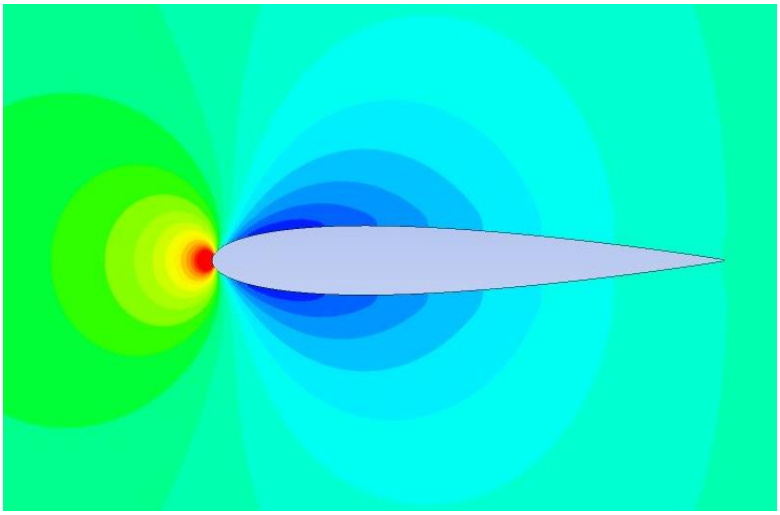

(c) Mean pressure coefficient contour of NACA 0012, Re = 10000

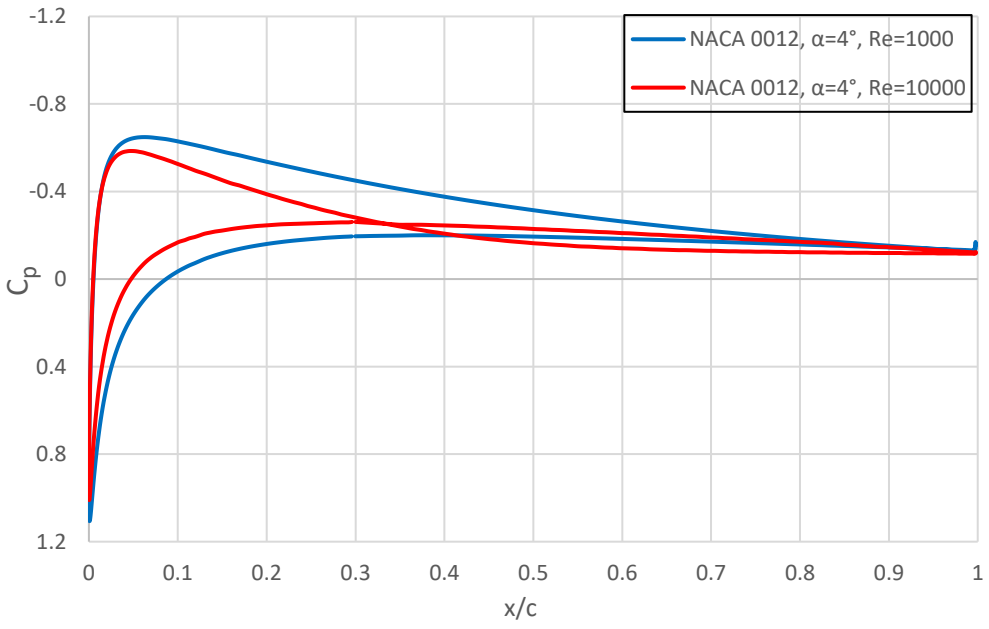

(d) $\alpha = 4^{\circ}$

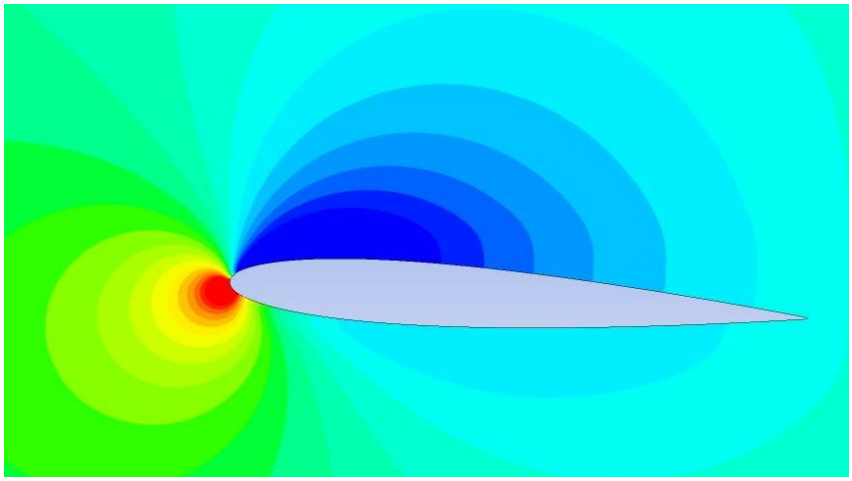

(e) Mean pressure coefficient contour of NACA 0012, Re = 1000

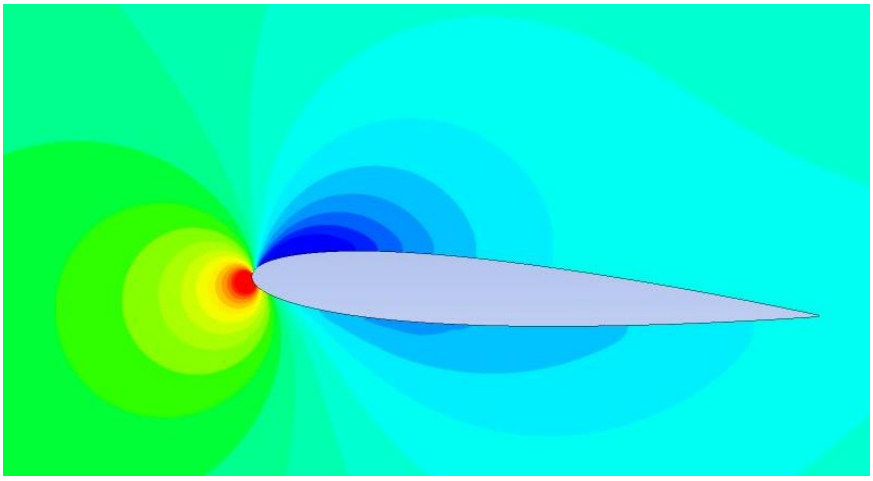

(f) Mean pressure coefficient contour of NACA 0012, Re = 10000

Figure 4. 20: Mean pressure coefficient distribution of NACA 0012 at $\alpha = 0^{\circ}\&\ 4^{\circ}$, $Re = 10^{3}\&10^{4}$

It is apparent that the same trend can be observed when it comes to the distribution of skin friction coefficient distribution. This is comparable to the distribution of the pressure coefficient distribution. According to Figure 4.18 (a), it is quite evident that as the Reynolds number rises, the friction coefficient of the skin reduces quite significantly. This is particularly relevant at higher angles of attack with a larger Reynolds number.

A closer look at Fig 4.21 (b) and (c) leads to the observation that as the Reynolds number rises from Re = 1000 to 10000 for $\alpha = 0^{\circ}$, the separation points shift towards the leading edge. Red points are highlighted on the airfoil to indicate

Also, it can be observed from Fig 4.21 (e) and (f) at $\alpha = 4^{\circ}$, that with the rising Reynolds number the separation points move towards the airfoil's leading edge. The obtained result for C_f demonstrates that the separation point is located on the airfoil's upper surface. This point is roughly 0.85 x/c in case of Re = 1000 and 0.4 x/c for Re = 10000.

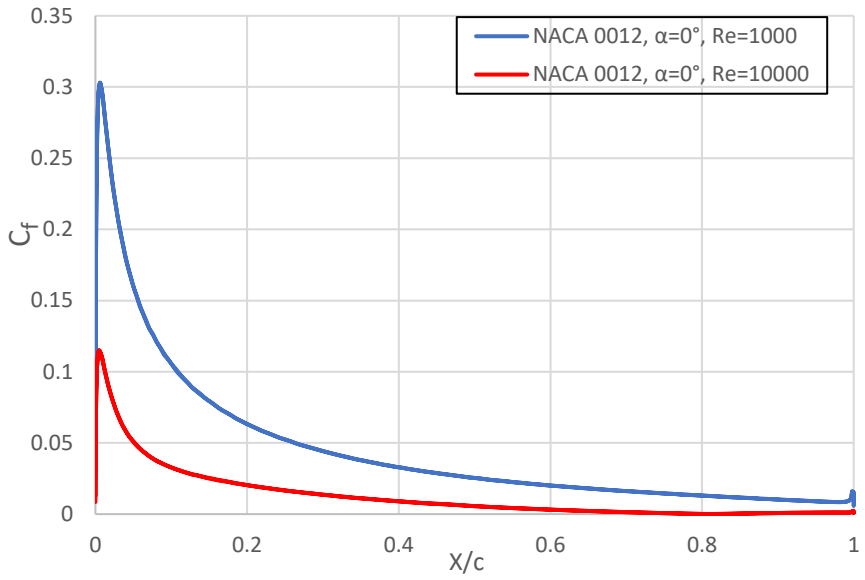

(a) $\alpha = 0^{\circ}$

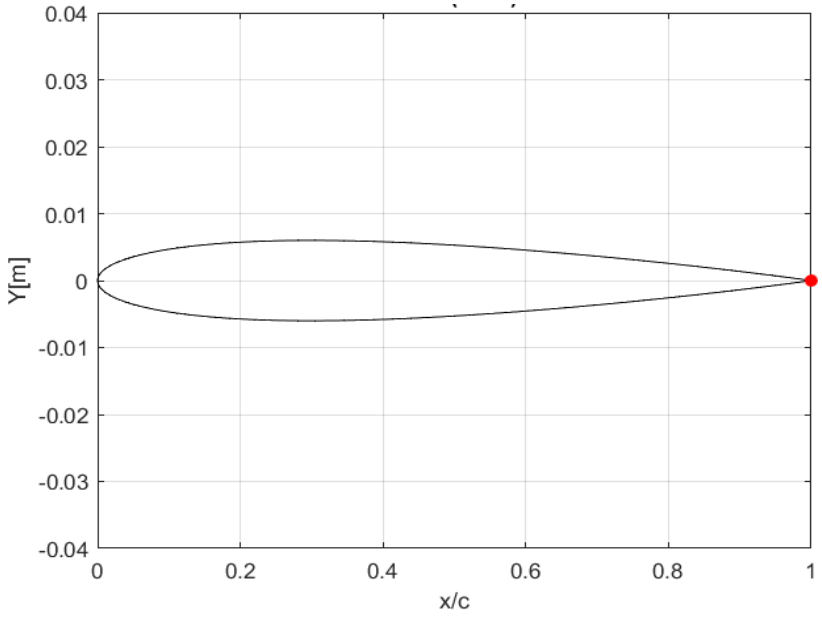

(b) Flow Separation point for NACA 0012 at $\alpha = 0^{\circ}$, $Re = 10^{3}$

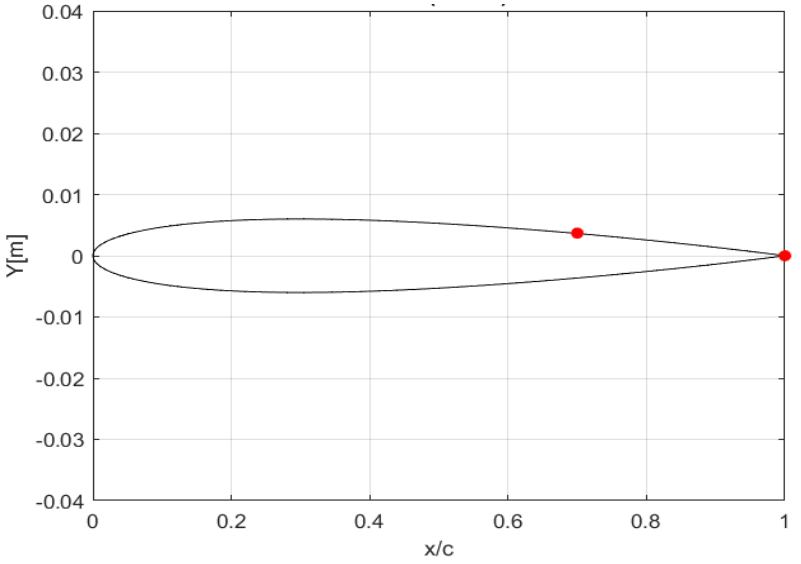

(c) Flow Separation point for NACA 0012 at $\alpha = 0^{\circ}$, $Re = 10^{4}$

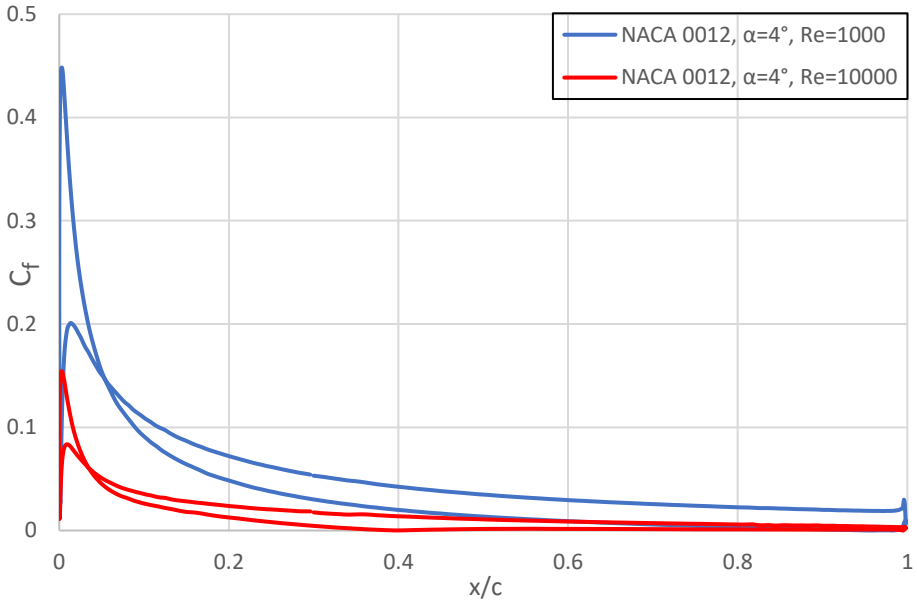

(d) $\alpha = 4^{\circ}$

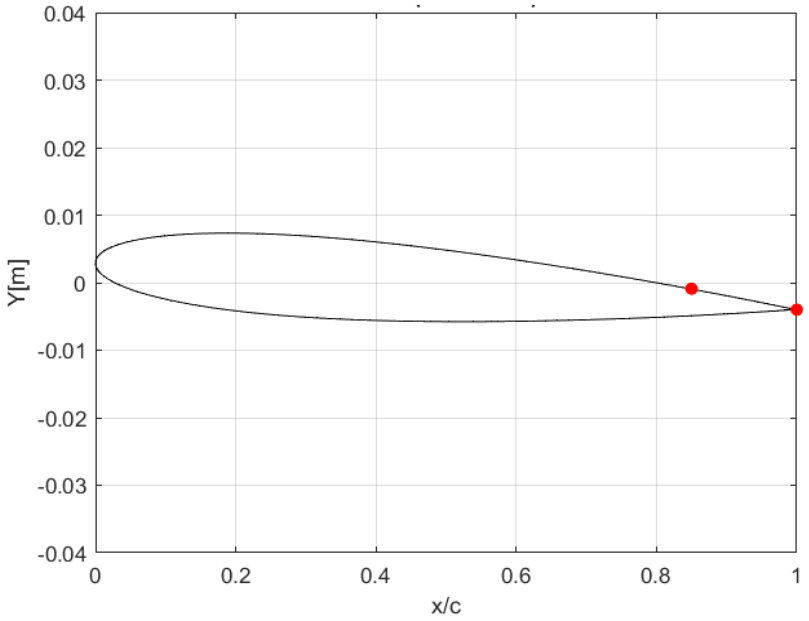

(e) Flow Separation point for NACA 0012 at $\alpha = 4^{\circ}$, $Re = 10^3$

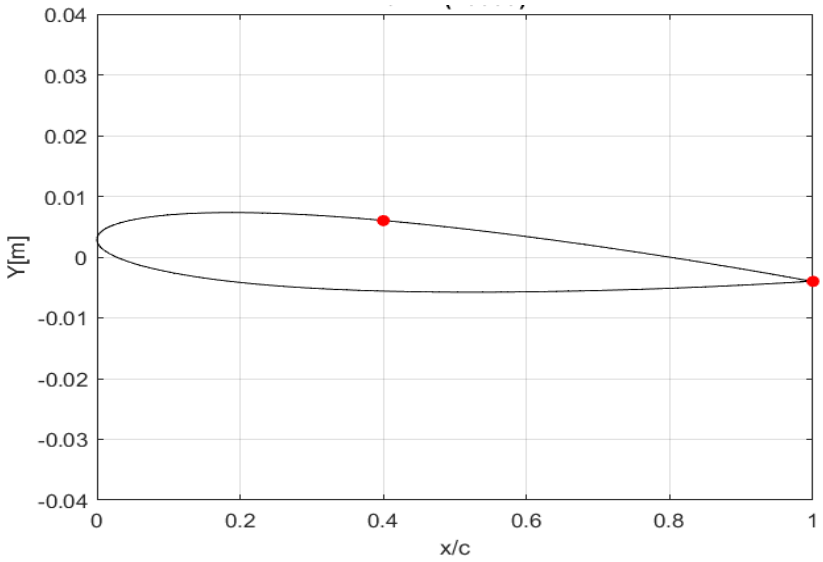

(f) Flow Separation point for NACA 0012 at $\alpha = 4^{\circ}$, $Re = 10^4$

Figure 4. 21: Mean skin friction coefficient distribution and separation point for NACA 0012 at $\alpha = 0^{\circ}$& 4°, $Re = 10^3$&10^4

Figure 4.22 illustrates how the Reynolds number impacts the mean drag coefficient. It is observed that with the rise in Reynolds number from Re = 1000 to Re = 10000, the value of mean drag coefficient decreases substantially. Furthermore, it is noted as angle of attack increase, values of mean drag coefficient also increase slightly for both the Reynolds numbers mentioned above. The mean drag coefficient is much higher at Re = 1000 in comparison to the values obatined at other Reynolds numbers. The decrease is drastic when the Reynolds number increases (Re = 1000 to Re = 5000). However, the decrease is comparatively much less when Reynolds number rises from Re = 7500 to Re = 10000. Additionally, it appears that the mean drag coefficient values are relatively higher at $\alpha = 4^{\circ}$ that the values obtained at $\alpha = 0^{\circ}$.

As a result, we can conclude that at low Reynolds numbers, the drag coefficient decreases with increasing Reynolds numbers. However, at moderate Reynolds numbers, there tends to be relatively little change in drag coefficient.

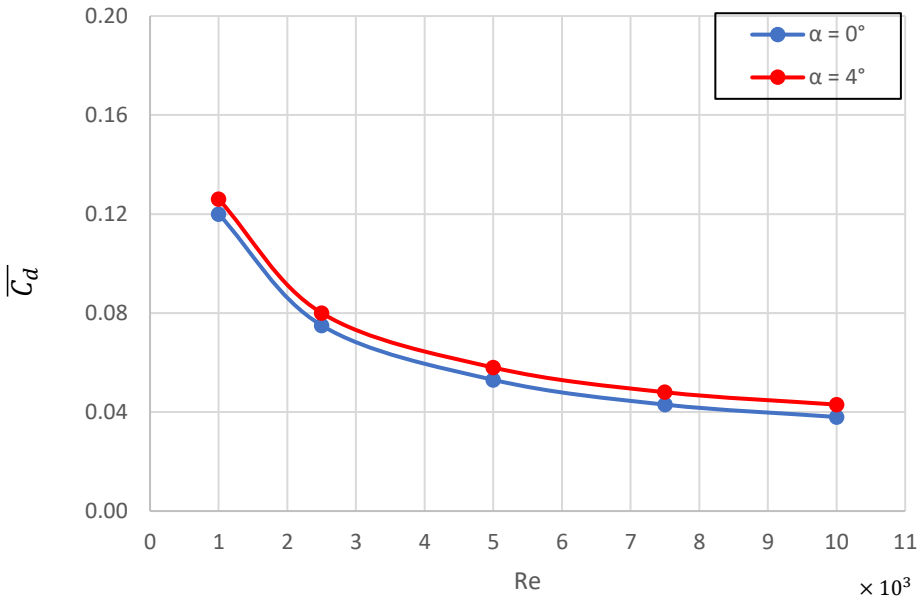

Figure 4. 22: Mean drag coefficient (C_d) for NACA 0012 at different Reynolds numbers (Re) , $\alpha = 0^{\circ} \& 4^{\circ}$

The trend observed is the same for both NACA 0012 and NACA 0014 stationary cases. The only difference is that NACA 0014 has slightly higher values than NACA 0012 and this can be attributed to the effect of thickness to chord ratio (t/c). Therefore,we can conclude that at low Reynolds numbers, the drag coefficient decreases with increasing Reynolds numbers. However, at moderate Reynolds numbers, there tends to be relatively little change in drag coefficient.

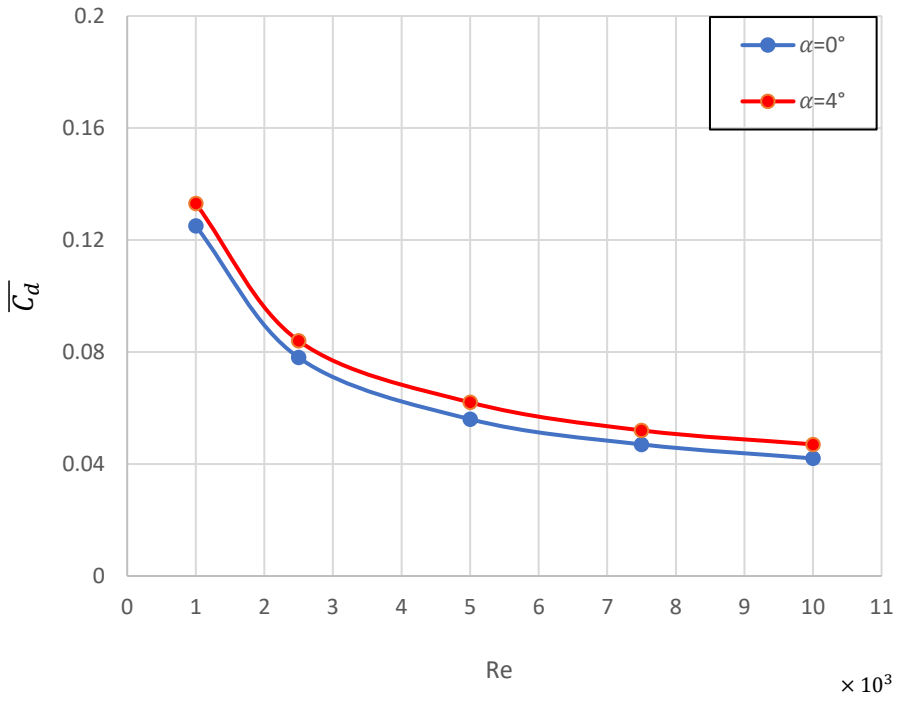

Figure 4. 23: Mean drag coefficient (C_d) for NACA 0014 (stationary case) at different Reynolds numbers (Re) , $\alpha = 0^{\circ}$ & 4°

It can be observed from figure 4.24 that as the Reynolds number rises, the value of mean drag coefficient grows in case of NACA 0014 plunging case. The mean drag coefficient grows significantly as the Reynolds number surges from 1000 to 5000. However, the increases in drag coefficient is comparatively much less as the Reynolds number surges 7500 to 10000. Additionally, it appears that the mean drag coefficient values are relatively higher at $\alpha = 4^{\circ}$ that the values obtained at $\alpha = 0^{\circ}$.

The trend observed in case of NACA 0014 plunging case is the opposite as observed in case of NACA 0014 stationary case and also for NACA 0012 stationary case. Therefore, in case of NACA 0014 plunging case we can conclude that at small Reynolds numbers, drag coefficient grows with the surge in Reynolds numbers. However, at moderate Reynolds numbers, there tends to be relatively little change in drag coefficient. In pure-plunge case, thrust is boserved whcih implies the negative

drag. The thrust is higher at low Reynolds numbers. In the current study, maximum thrust is obtained at low Reynolds number (Re = 1000) and the value decrease as the value of Reynolds number increases.

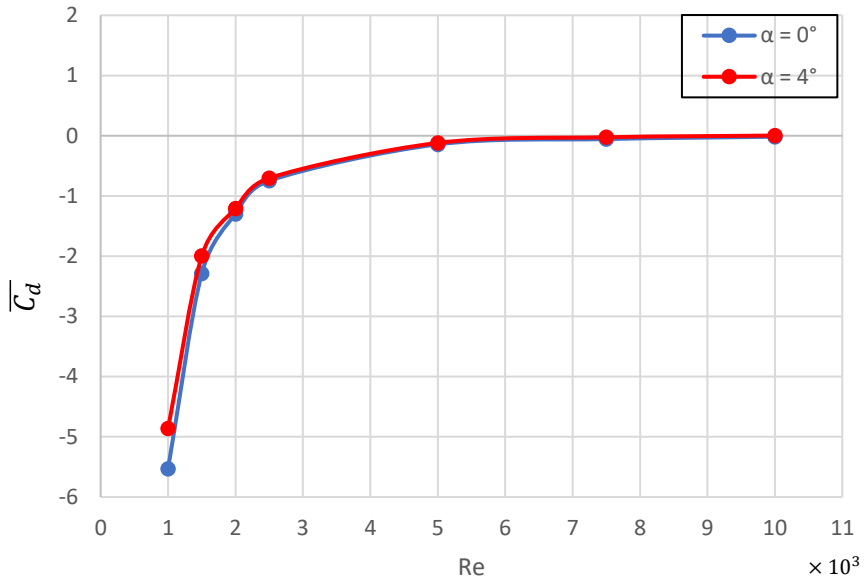

Figure 4. 24: Mean drag coefficient (C_d) for NACA 0014 (pure-plunge case) at different Reynolds numbers (Re) , $\alpha = 0^{\circ} \& 4^{\circ}$

The instantaneous lift and drag coefficients versus non-dimensional time step at various Reynolds number are presented in Figure 4.25 for NACA 0012 at $\alpha = 4^{\circ}$. Figure 4.25 (a) demonstrates that as the Reynolds number rises, the lift coefficient decreases for $\alpha = 4^{\circ}$. At the starting point (t^*= 0 to 10), the simulation begins with an assumption that is fundamentally unstable, resulting in a spike in performance. Once the solutions start to converge at time t^*= 30, then there is a gradual convergence after that point.

The instantaneous drag coefficient is found to diminish with the rise of the Reynolds number for the angle of attack equal to 4°. The values begin to converge at t* = 30. (Figure 4.25 (b))

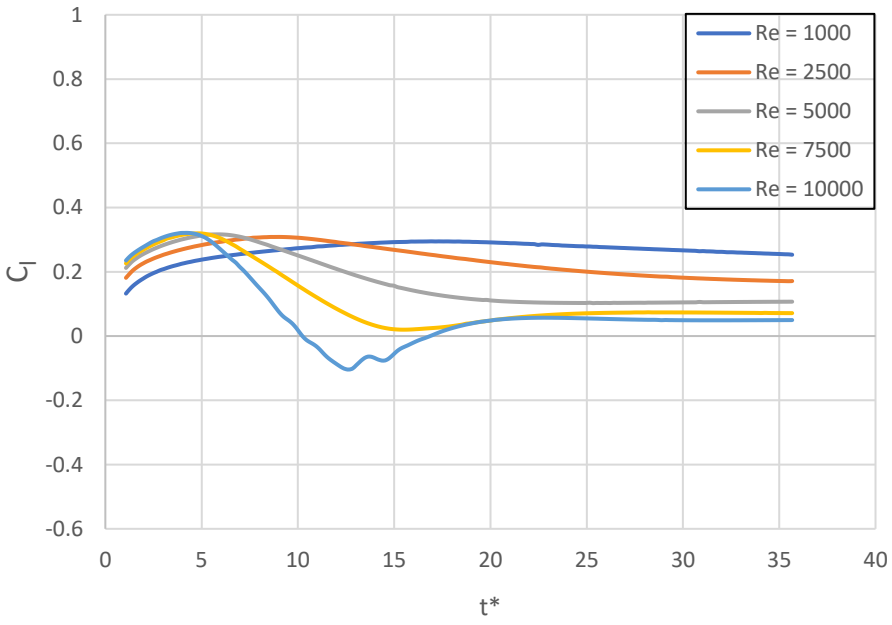

(a) Instantaneous lift coefficient

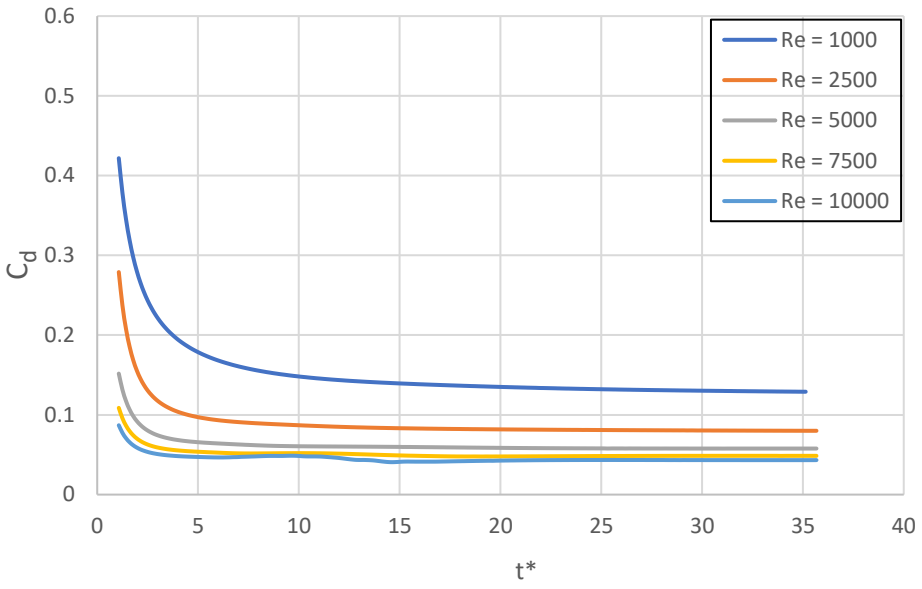

(b) Instantaneous drag coefficient

Figure 4. 25: Instantaneous aerodynamic coefficients of NACA 0012 at different Reynolds numbers (Re) , $\alpha = 4^{\circ}$

The instantaneous lift and drag coefficients versus non-dimensional time step at various Reynolds number are presented in Figure 4.26 for NACA 0014 (stationary case) at $\alpha = 4^{\circ}$. Figure 4.25 (a) demonstrates that as the Reynolds number rises, the lift coefficient decreases for $\alpha = 4^{\circ}$. At the starting point (t*= 0 to 10), the simulation begins with an assumption that is fundamentally unstable, resulting in a spike in performance. Once the solutions start to converge at time t*= 30, then there is a gradual convergence after that point. An oscillatory behaviour is detected for higher Reynolds number and thus alternating vortices begin to develop at the airfoil's trailing edge.

The instantaneous drag coefficient is found to diminish with the rise of the Reynolds number for angle of attack equal to 4°. The values begin to converge at t^* = 30. The oscillations are detected for higher Reynolds numbers. (Figure 4.26 (b))

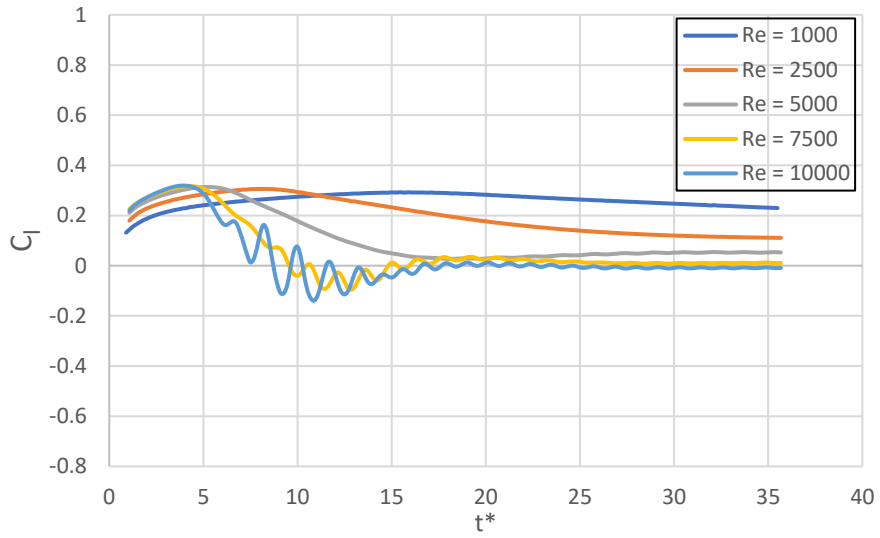

(a) Instantaneous lift coefficient

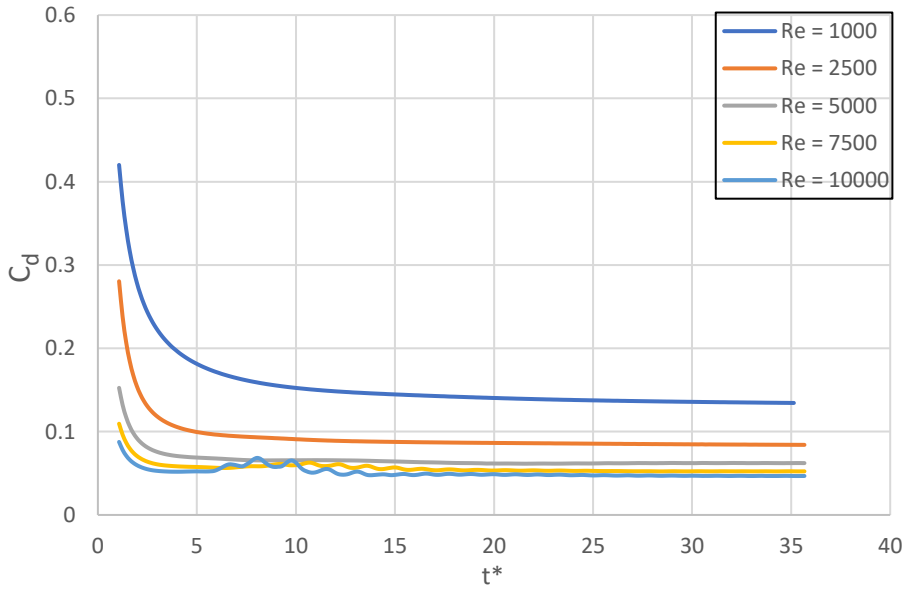

(b) Instantaneous drag coefficent

Figure 4. 26: Instantaneous aerodynamic coefficients of NACA 0014 (stationary case) at different Reynolds numbers (Re) , $\alpha = 4^{\circ}$

4.4 Effect of reduced frequency (k)

Using two separate values of angles of attack ($\alpha = 0^{\circ}\&4^{\circ}$) and two different reduced frequencies ($k = 1\ \&2$), this section discusses the effect of reduced frequency on aerodynamic coefficients at $Re = 10000$. An analysis of the results obtained for each case that has been mentioned above is presented and discussed.

It is quite apparent from Figure 4.27 (a) that as the reduced frequency increases, we see a substantial increase in the the maximum amplitude and a a similar decrase in the minimum value of lift coefficient. A significant increase in frequency is observed. It is also worth noting that there is a phase shift present as well. The reason for this can be attributed to the fact that reduced frequency has been increasing, which in turn means increased frequency as well.

A substantial decrease in drag coefficient occurs because of an increase in reduced frequency as shown in Figure 4.27 (b). As far as amplitude is concerned, the maximum amplitude is almost the same for both the cases. However, the minimum values for amplitude are significantly lower for the higher reduced frequency when compared to the lower value of reduced frequency. In addition, there is also a phase shift that occurs as well.

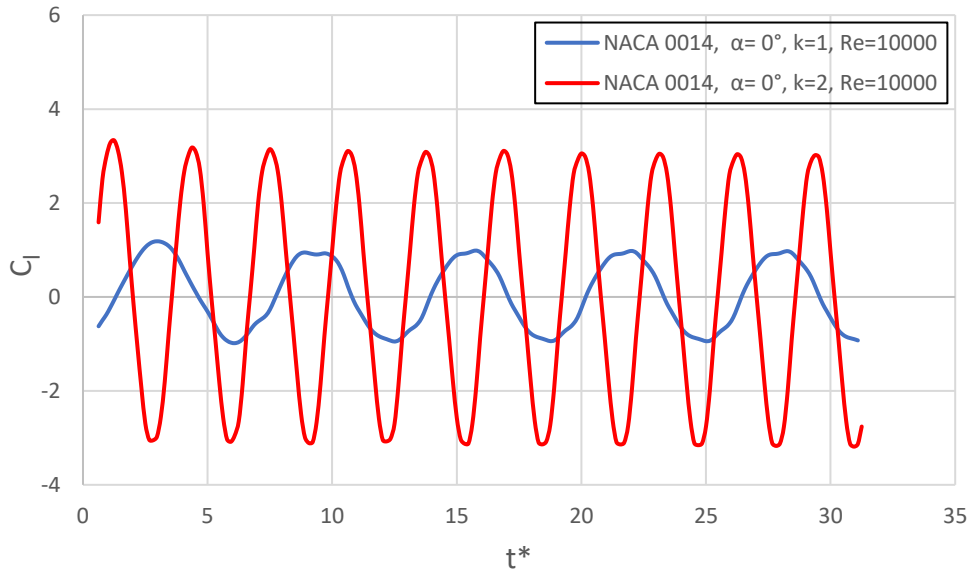

(a) Instantaneous lift coefficient

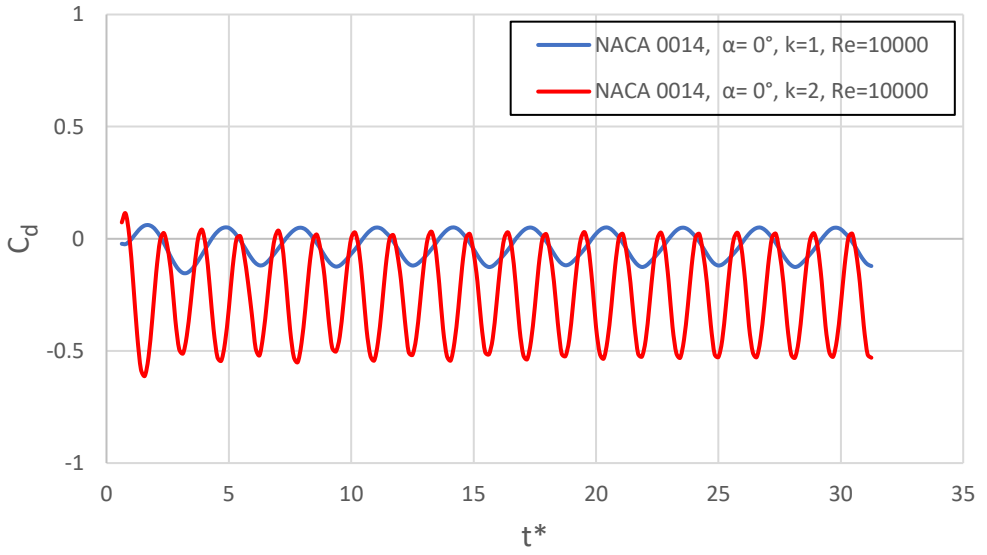

(b) Instantaneous drag coefficient

Figure 4. 27 : Instantaneous aerodynamic coefficients of NACA 0014 (pure-plunge case) for different values of k at $\alpha = 0^{\circ}$, $Re = 10^4$

4.5 Vortex shedding pattern

In order to distinguish unsteady flow behaviour as well as vortex shedding patterns, it is pertinent to observe the vortex shedding pattern. Apparently, there is a continuous vortex pattern in the wake of the airfoil. There is no alternating vortex shedding pattern in the wake of NACA 0012 airfoil at both $\alpha = 0^{\circ}$ and $\alpha = 4^{\circ}$ (Figure 4.28).

From Figure 4.29, it can be seen that for NACA 0014 at $\alpha = 0^{\circ}$ the vortices are continuous without any vortex shedding pattern at the wake. However, at $\alpha = 4^{\circ}$, it is observed that alternating vortices begin to develop in the wake of the airfoil.

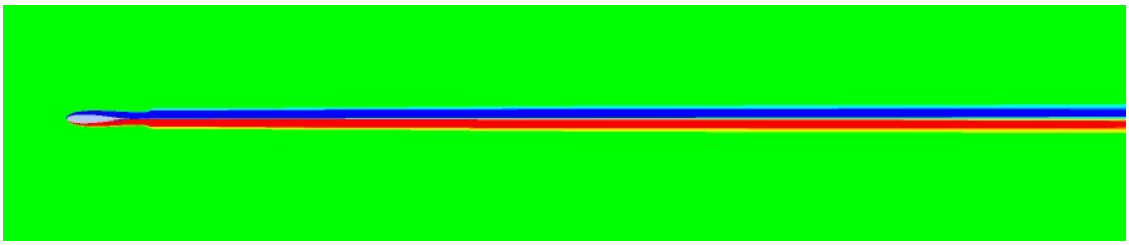

(a) $\alpha = 0^{\circ}$

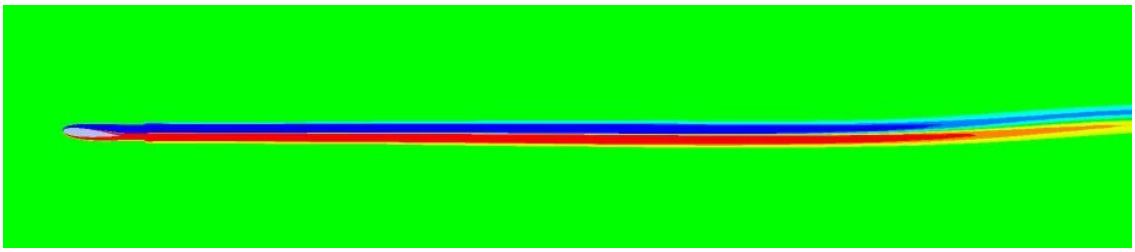

(b) $\alpha = 4^{\circ}$

Figure 4. 28: Instantaneous vorticity patterns of NACA 0012, stationary condition at $Re = 10^4$

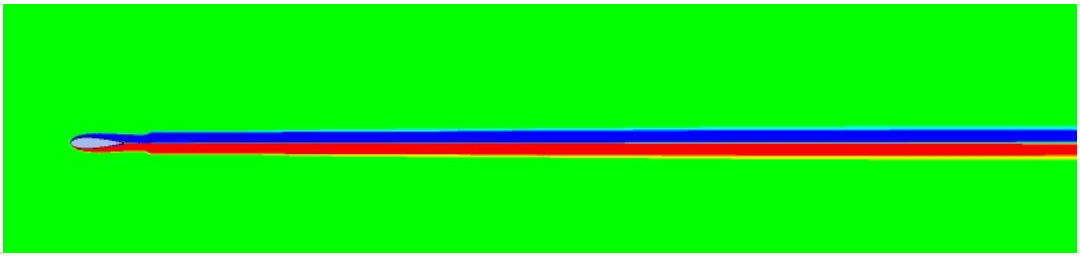

(a) $\alpha = 0^{\circ}$

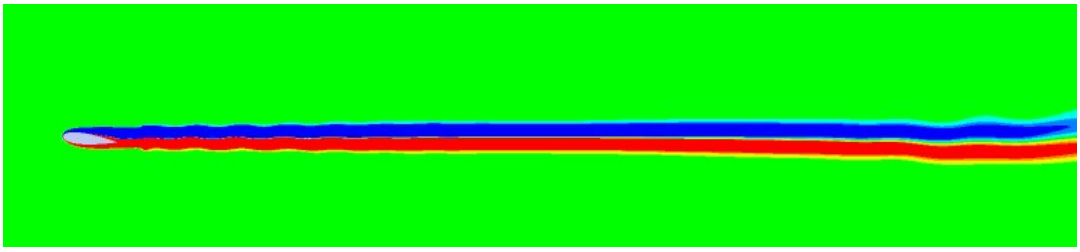

(b) $\alpha = 4^{\circ}$

Figure 4. 29: Instantaneous vorticity patterns for NACA 0014, stationary condition at $Re = 10^4$

As shown in Figure 4.30, the upper and lower surfaces do not shed vorticies alternately one at a time. In contrast, two vortices with the same sign are shed per half cycle from the same side, followed by another two vortices from the opposite side of the sign. There is also a slight shift in the direction of the mushroom-like vortices, so that they are now oriented slightly down-stream. Essentially, a drag producing wake begins to transition into a neutral wake based on these patterns [59].

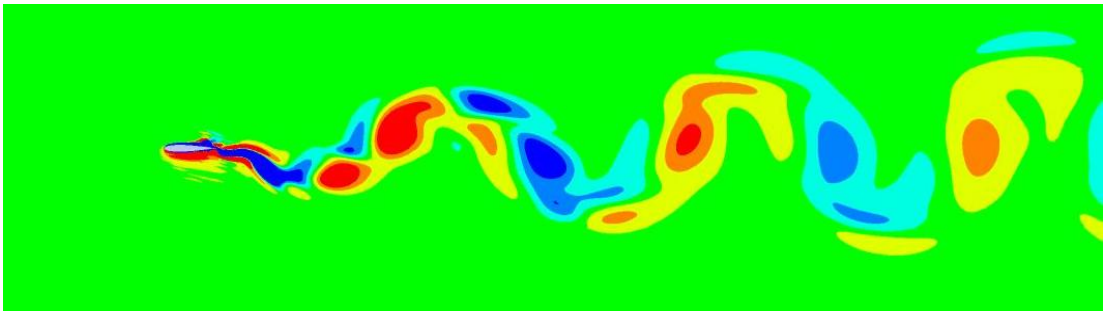

(a) $\alpha = 0^{\circ}$

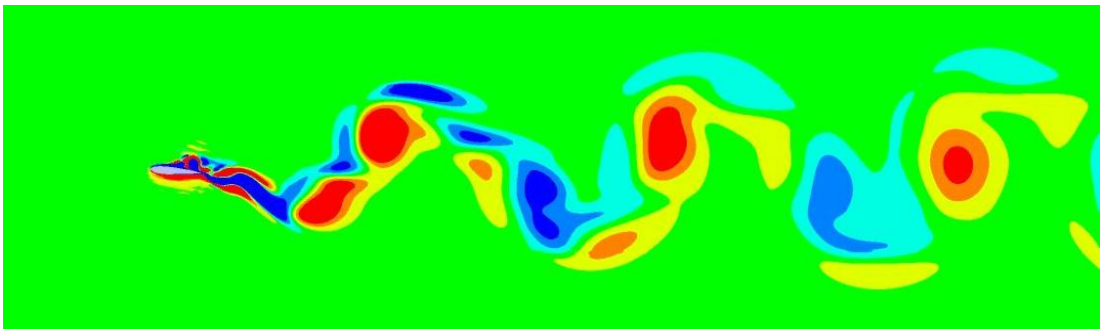

(b) $\alpha = 4^{\circ}$

Figure 4. 30: Instantaneous vorticity patterns for NACA 0014 plunging-state condition at $Re = 10^4$, $k = 1$

It can be observed from Figure 4.31 that the vortex consists of multiple layers. The upper and lower surfaces shed vortices alternately one at a time. There are two dominant vortex pairs in the wake, and they appear as "arms" either higher up the wake, or lower down the wake. Consequently, it produces a supplementary set of vortices, which are mostly deformed downstream of the airfoil. In addition, it is observed that the wake width varies from its initially narrow width in the vicinity of the airfoil to its final width downstream of the airfoil [45].

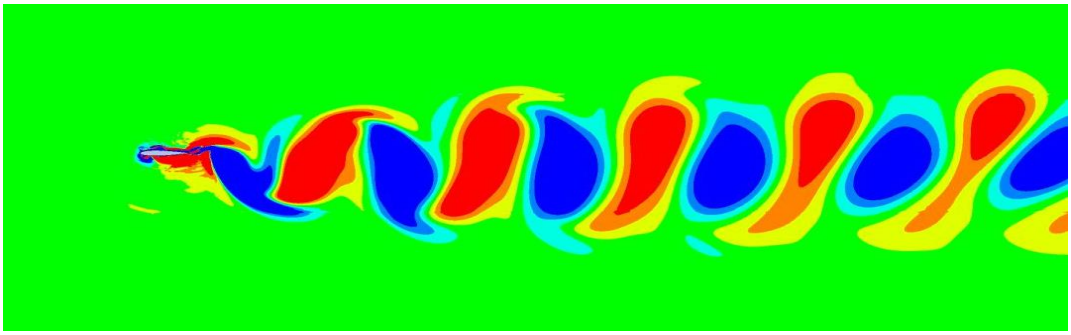

(a) $\alpha = 0^{\circ}$

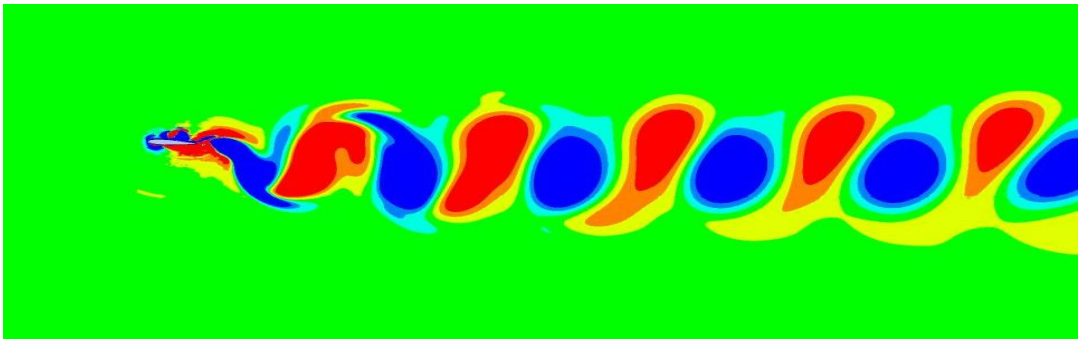

(b) $\alpha = 4^{\circ}$

Figure 4. 31: Instantaneous vorticity patterns for NACA 0014 plunging-state condition at $Re = 10^4$, $k = 2$

CHAPTER 5

CONCLUSION

The unsteady behavior of the flow around a symmetric NACA 0014 airfoil is analyzed taking into consideration an oscillating motion in a sinusoidal pure-plunge mode as well as the stationary condition. Numerical simulations are performed by incorporating the two-dimensional unsteady, incompressible Navier-Stokes equation at Reynolds number (Re) = 10^4. The flow is visualized at the following two angle of attacks: 0° and 4°. The flow is assumed to be laminar at this Reynolds number.

Several aspects of aerodynamics are discussed, including instantaneous and mean aerodynamic coefficients, pressure distributions, vorticity distributions, velocity magnitude distributions, and streamlines. It is apparent that the lift coefficients and drag coefficients increase gradually with the increasing angle of attack as it increases from $0^\circ to\ 4^\circ$ for NACA 0014 for both pure-plunge and stationary condition.

The analysis of thickness to chord ratio (t/c) in terms of aerodynamic coefficients is also presented. It can be observed that as the thickness to chord ratio increase, the drag coefficient also increases slightly. For both $\alpha = 0^\circ$ and $\alpha = 4^\circ$, the value of drag coefficient (C_d) is slightly higher for NACA 0014 as compared to NACA 0012.

The mean pressure coefficient distribution trend for NACA 0012 and NACA 0014 at $\alpha = 0^\circ$ is quite similar as is quite evident that the trends for both the cases are quite similar. Although, as far as the leading edge and the trailing edge of the NACA 0014 are concerned, the negative pressure at both ends of the NACA 0014 is slightly higher than that observed at the leading edge of NACA 0012. Moreover, it has been observed in the case of NACA 0012 at $\alpha = 4^\circ$, negative pressure at the upper surface of the leading edge and positive pressure at lower surface of the leading edge have a

relatively higher value when compared to the value of NACA 0014 in terms of pressure at the airfoil's upper and lower surface, respectively.

The upper surface of NACA 0012 at $\alpha = 0^{\circ}$ has a slightly higher mean skin friction coefficient than the lower surface. While NACA 0012 and NACA 0014 do have slightly different mean skin friction coefficient distributions, overall, the distributions are similar. According to the obtained results, the separation point on the airfoil's upper surface is roughly 0.7 x/c in both cases. For NACA 0012, the mean skin friction coefficient is slightly higher at the leading and trailing edges of the lower surface at $\alpha = 4^{\circ}$. Despite this, the mean skin friction distribution trend is nearly the same for both airfoil configurations. It appears from the results that the separation point is roughly 0.4 x/c on the airfoil's upper surface in both the cases.

It is also observed that as the Reynolds number increases, the instantaneous lift and drag coefficients decrease in case of NACA 0012 and NACA 0014 stationary case. The decrease is drastic when the reynolds number increases from Re = 1000 to Re = 5000. However, the decrease is comparatively much less as the Reynolds number increases from Re = 7500 to Re = 10000. Additionally, it can also be observed that the mean drag coefficient values are relatively higher at $\alpha = 4^{\circ}$ that the values obtained at $\alpha = 0^{\circ}$. As a result, we can conclude that at low Reynolds numbers, the drag coefficient decreases with increasing Reynolds numbers. However, at moderate Reynolds numbers, the drag coefficient tends to remain relatively constant. However, the trend seems to be opposite in case of NACA 0014 pure-plunge case. The mean drag coefficient increases as the Reynolds number increases in case of NACA 0014 plunging case. The trend observed is the same for both NACA 0012 and NACA 0014 stationary cases. The only difference is that NACA 0014 has slightly higher values than NACA 0012 and this can be attributed to the effect of thickness to chord ratio (t/c).

The flow behavior is also analyzed for NACA 0012 at $Re = 10^3$ and $Re = 10^4$. The flow is visualized at the following two angle of attacks: 0° and 4° for stationary condition. The coefficients of mean pressure and mean skin friction are discussed for

two distinct angles of attack ($\alpha = 0^{\circ}$ and $\alpha = 4^{\circ}$) at two different Reynolds numbers ($Re = 10^3$ and $Re = 10^4$).

It is observed that the pressure coefficient decreases significantly as Reynolds number increases ($Re = 10000$) compared to $Re = 1000$ as Reynolds number increases. As can also be observed, the difference between the pressure coefficient distribution at $Re = 1000$ and $Re = 10000$ and is pretty low at $\alpha = 0^{\circ}$. However, the difference is significant and visible at $\alpha = 4^{\circ}$ between $Re = 1000$ and $Re = 10000$. It is apparent that the same trend can be observed when it comes to the distribution of skin friction coefficient distribution. This is similar to the distribution of the pressure coefficient distribution. This is particularly relevant at higher angles of attack with a larger Reynolds number.

It can be observed for NACA 0014 (pure-plunge case) that as the reduced frequency increases, we see a substantial increment in the maximum amplitude and an equally substantial decrease in the minimum value of the lift coefficient. However, a substantial decrease in drag coefficient occurs with an increase in reduced frequency. As far as amplitude is concerned, the maximum amplitude is almost the same for both the cases. The minimum values for amplitude are significantly lower for the higher reduced frequency when compared to the lower value of reduced frequency. In addition, there is also a phase shift that occurs as well.

REFERENCES

[1] Shyy W., Lian W., Tang J., and Liu H., *«Computational Aerodynamics of Low Reynolds Number Plunging, Pitching and Flexible Wings for MAV Applications,»* 2008.

[2] Triantafyllou M.S., Techet A.H., and Hover F.S., *«Review of Experimental Work in Biomimetic» IEEE Journal of Oceanic Engineering,* Vol 29, no. 3, 2004.

[3] Kang C-k, and Shyy W., «Scaling law and enhancement of liftgeneration of an insect-size hovering flexiblewing.,» *Jounal of the Royal Society*, no. R Soc Interface 10: 20130361, 2013.

[4] Dong H., Mittal, R. and Najjar, F. M., «Wake topology and hydrodynamic performance of low-aspect-ratio flapping foils,» *Cambridge University Press*, Vol 566, pp. 309-343, 2006.

[5] Akhtar I, Mittal R, Lauder G V and Drucker E.G «Hydrodynamics of a Biologically Inspired Tandem Flapping Foil Configuration,» *Theoretical and Computational Fluid Dynamics*, Vol 21, no. 3, pp. 155-170, 2007.

[6] Wang, Z.J., Birch, J.M and Dickinson, M.H., «Unsteady Forces and Flows in Low Reynolds Number H overing Flight : Two Dimensional Computations vs Robotic Wing E xperiments,» *The Journal of Experimental Biology*, Vol 207, no. 3, pp. 449-460, 2003.

[7] Windte, J., Radespiel, R. and Scholz, U., «RANS Simulation of the Transitional Flow Around Airfoils at Low Reynolds Numbers for Steady and Unsteady Onset Conditions,» RTO AVT Specialists Meeting on "Enhancement of NATO Military Flight Vehicle Performance by Management of Interacting Boundary Layer Transition and Separation, 2005.

[8] Platzer, M. F., Jones, K.D., Young, J., and Lai J.C.S., «Flapping Wing Aerodynamics: Progress and Challenges,» *AIAA Journal*, Vol 46, no. 9, 2008.

[9] Kurtulus, D.F., Farcy,A. and Alemdaroglu, N., «Unsteady Aerodynamics of Flapping Airfoil in Hovering Flight at Low Reynolds Numbers,» 43rd *AIAA Aerospace Sciences Meeting and Exhibit,* 2005.

[10] Betz A., «Ein beitrag zur erklarung des segelfluges,» *Zeitschrift fur Flugtechnik und Motorluftschiffahrt*, Vol 3, pp. 269-272, 1912.

[11] Knoller R., «Die gesetze des luftwiderstandes,» *Flug-und Motortechnik Wien*, Vol 3, no. 21, pp. 1-7, 1909.

[12] Jones, K.D., Duggan, S.J. and Platzer, M.F., «Flapping-Wing Propulsion for a Micro Air Vehicle,» AIAA Paper No. 2001-0126, 39th *AIAA Aerospace Sciences Meeting,* Reno, Nevada, 2001.

[13] Jones, K.D. and Platzer, M.F.,, «An Experimental and Numerical Investigation of Flapping-Wing Propulsion,» *AIAA* Paper No. 99-0995, 37th *AIAA Aerospace Sciences Meeting,* Reno, Nevada, 2001.

[14] Katzymayer R., «Effect of Periodic Changes of Angle of Attack on Behavior of Airfoils,» *National Advisory Committee for Aeronautics,* 1922.

[15] Birnbaum W., «Das ebene problem des schlagenden fluels,» *Zeitschrift fur Angewandte Mathematik und Mechanik,* Vol 4, no. 4, pp. 277-292, 1924.

[16] Theodorsen T., «General theory of aerodynamic instability and the mechanism of flutter,» *Technical Report* 496, NACA,, 1935.

[17] Garrick, I. E. «Propulsion of a Flapping and Oscillating Airfoil,» *Technical Report* 567, NACA, 1936.

[18] Kunz, P. and Kroo, I, «Analysis and Design of Airfoils for Use at Ultra-Low Reynolds Numbers,» Proc. *AIAA Fixed, flapping and rotating wing aerodynamics at very low Reynolds numbers conference*, edited by T. J. Mueller, Notre Dam, pp. 35-60, 2007.

[19] Mateescu, D and Abdo, M, «Analysis of flows past airfoils at very low Reynolds numbers,» *Proc. IMechE Part G: J. Aerospace Engineering*, Vol 224, pp. 757-775, July 2010.

[20] Ol, M.V., Eldredge, J.D ., and Wang, C., «High-Amplitude Pitch of a Flat Plate: An Abstraction of Perching and Flapping,» *International Journal of Micro Air Vehicles*, Vol 1, no. 3, pp. 203-216, 2009.

[21] Shyy, W., Aono H., Kang, C.K., and Liu,H., «An Introduction to Flapping Wing Aerodynamics,» *Cambridge University Press*, 2013.

[22] Tuncer, I.H., and Platzer, M.F., «Computational study of flapping airfoil aerodynamics,» *Journal of aircraft*, Vol 37, no. 3, pp. 514-520, 2000.

[23] Tuncer I.H., Walz, R., and Platzer, M.F., «A computational study on the dynamic stall of a flapping airfoil.,» AIAA paper 98-2519, 16th *Applied Aerodynamics Conference*, Albuquerque, New Mexico, *AIAA paper*, June, 15-18 1998.

[24] Tuncer, I.H., and Platzer, M.F., «Thrust generation due to airfoil flapping,» *AIAA Journal*, Vol 34, no. 2, pp. 324-331, 1996.

[25] Isogai, K., Shinmoto, Y., and Watanabe, Y., « Effects of dynamic stall on propulsive efficiency and thrust of flapping airfoil,» *AIAA Journal*, Vol 37, no. 10, pp. 1145-1151, 1999.

[26] Kurtulus, D.F., «On the Unsteady Behavior of the Flow around NACA 0012 Airfoil with Steady External Conditions at Re=1000,» *International Journal of Micro Air Vehicles*, Vol 7, no. 3, pp. 301-326, 2015.

[27] «ANSYS Fluent Userguide,» ANSYS Inc, 2013.

[28] Kurtulus, D.F., «On the wake pattern of symmetric airfoils for different incidence angles at Re = 1000,» *International Journal of Micro Air Vehicles* , Vol 8, no. 2, pp. 109-139, 2016.

[29] Kurtulus, D.F., «On the unsteady behavior of the flow around NACA 0012 airfoil with steady external conditions at Re=1000,» *International Journal of Micro Air Vehicles*, Vol 7, no. 3, pp. 301-326, 2015.

[30] Khalid, M.S., Akhtar, I., and Durrani, N.I., «Analysis of Strouhal Number based Equivalence of Pitching and Plunging Airfoils and Wake Deflection,» *Proceedings of the Institution of Mechanical Engineers Part G Journal of Aerospace Engineering*, Vol 229, no. 8, 2014.

[31] Ahmed, T., and Kurtulus, D.F., «Unsteady Aerodynamıcs of Cambered Aırfoıls at Low Reynolds Number,» *11th Ankara International Aerospace Conference*, Ankara, 2021.

[32] Castro, B.M., «Multi-Block Parallel Navier-Stockes Simulation of Unsteady Wind Tunnel and Ground Interference Effects,» *PhD thesis*, Naval Postgraduate School, 2001.

[33] Johnson, Susan R., «Computatıonal Aerodynamıc Analysıs of Aırfoıls FOR Energy-Producıng Sailing Ships,» *Master's thesis*, Naval Postgraduate School, 2020.

[34] Lund, T.C., «Experimental and computational investigation of flapping-wing propulsion for micro-air vehicles.,» *Master's thesis*, Naval Postgraduate School, 2000.

[35] Jones, K.D., Platzer, M.F., «Flapping-Wing Propulsion for a Micro Air Vehicle,» AIAA Paper No. 2000-0897, 38th *AIAA Aerospace Sciences Meeting*, Reno, Nevada., 2000.

[36] Hamdani, H.R., and Zareen, H., «Systematic Investigation of Thrust Production during Plunging Motion of the Airfoil,» *Journal of Applied Fluid Mechanics*, Vol 11, no. 4, pp. 1073-1088, 2018.

[37] Young, J., and Lai, J. C. S., «Oscillation Frequency and Amplitude Effects on the Wake of a Plunging Airfoil,» *AIAA Journal*, Vol 42, no. 10, 2012.

[38] Lianga, C., Miyaji, K., and Zhang, B., «An efficient correction procedure via reconstruction for simulation of viscous flow on moving and deforming domains,» *Journal of Computational Physics,* Vol 256, pp. 55-68, 2014.

[39] Kunz, P.J., «Aerodynamıcs and Desıgn for Ultra-low Reynolds Number Flıght,» *Phd thesis*, 2003.

[40] Mahmoud, Osama Mohamed Kamal Mohamed, «Experimental investigation of low speed flow over flapping airfoils and airfoil combinations,» *Phd thesis*, Naval Postgraduate School, 2001.

[41] Ilio, G.D., Chiappini, D., Ubertini, S., Bella, G., and Succi, S., «Fluid flow around NACA 0012 airfoil at low-Reynolds numbers with hybrid lattice Boltzmann method,» *Computers & Fluids,* Vol 166, pp. 200-2008, 2018.

[42] Pranesh, C., Sivapragasam, M., Deshpande, M.D., and Narahari, H.K., «Negative lift characteristics of NACA 0012 aerofoil at low Reynolds numbers,» *Indian Academy of Sciences*, 2019.

[43] Naeem, N., Fouda, M., Guney, M., Kurtulus, D. F., «Wake patterns and mode switching at low Reynolds numbers,» *Progress in Computational Fluid Dynamics, An International Journal* (in press), 2023.

[44] Kurtulus, D.F., «Critical Angle and Fundamental Frequency of Symmetric Airfoils at Low Reynolds Numbers,» *Journal of Applied Fluid Mechanics*, Vol 15, no 3, pp.723-735, May 2022 10.47176/JAFM.15.03.33099

[45] Kurtulus, D. F., «Vortex flow aerodynamics behind a symmetric airfoil at low angles of attack and Reynolds Numbers, » *International Journal of Micro Air Vehicles,* Vol 13: 1–18, 2021, doi: 10.1177/17568293211055653.

[46] Gunaydinoglu, E., Kurtulus, D.F., «Pressure–velocity coupling algorithm-based pressure reconstruction from PIV for laminar flows, » *Experiments in Fluids*, Vol 61: 5, 2022, https://doi.org/10.1007/s00348-019-2831-1.

[47] Kurtulus, D.F., Ability to forecast unsteady aerodynamic forces of flapping airfoils by Artificial Neural Network, » *Neural Computing & Applications*, Vol. 18, Issue 4, pp.359-368, 2009.

[48] Beker, C., Turgut, A.E., Arıkan, K.B., K«urtulus, D.F., «Fluıd-structure ınteractıon analysıs of a four-bar flapping wing mechanism, » *IX Eccomas Thematic Conference on Smart Structures and Materials Smart* 2019 A. Benjeddou, N. Mechbal and J.F. Deü (Eds), pp.1637-1647, Paris, France, 8-11 July 2019, ISBN: 978-84-949194-6-6.

[49] Senol, G., Arıkan, K.B., Kurtulus, D.F., «Experimental and Numerical Results of a Flapping Wing Four Bar Mechanism, » 55th *AIAA Aerospace Sciences Meeting, AIAA Scitech Forum*, AIAA 2017-0498, 9-13 January, 2017.

[50] Comez Y.F., Senol M.G., Kurtulus D.F., Arikan K.B., «Unsteady Aerodynamic Analysis of a Flapping Wing Actuated with PZT Material, » *Workshop on Non-Intrusive Measurements of Unsteady Flows and Aerodynamics*, Poitiers, France, 27-29 October, 2015.

[51] Hizli, H., Kurtulus, D. F., «Numerical and Experimental Analysis of Purely Pitching and Purely Plunging Airfoils in Hover, » *International Micro Air Vehicle Conference and Flight Competition*, 03-06 July, 2012 – Braunschweig, Germany.

[52] Gunaydinoglu, E., Kurtulus, D.F., «Effect of Vertical Translation on Unsteady Aerodynamics of a Hovering Airfoil, » *Fifth European Conference on Computational Fluid Dynamics* ECCOMAS CFD 2010, June 14th - 17th, 2010 Lisbon, Portugal.

[53] Kurtulus, D.F., David, L., Farcy, A., Alemdaroglu, N., «Aerodynamic Characteristics of Flapping Motion in Hover, » *13th Int Symp on Applications of Laser Techniques to Fluid Mechanics*, 1130, Lisbon, Portugal, 26-29 June 2006 (The paper is selected by the symposium jury for an invitation to submit the paper to Experiments in Fluids).

[54] Kurtulus, D.F., Farcy, A., Alemdaroglu, N., «Unsteady Aerodynamics of Flapping Airfoil in Hovering Flight at Low Reynolds Numbers, » AIAA-2005-1356, 43rd *AIAA Aerospace Sciences Meeting and Exhibit*, Reno, Nevada, USA, 10 - 13 Jan, 2005.

[55] Kurtulus, D.F., « Numerical and Experimental Analysis of Flapping Motion in Hover, » *Application to Micro Air Vehicles*, Joint Ph.D. thesis Poitiers University/ENSMA (Poitiers-France) and METU (Ankara-Turkey), 17 June 2005, Poitiers, France.

[56] «ANSYS Fluent User's Guide,» ANSYS, Inc, 2013.

[57] «Computer Program To Obtain Ordinates for NACA Airfoils,» *National Aeronautics and Space Administration*, 1996.

[58] Tuncer, I.H., and Kaya, M., «Thrust Generation Caused by Flapping Airfoils in a Biplane Configuration,» *Journal of Aircraft*, Vol 40, no. 3, 2003.

[59] Lai, J.C.S., and Platzer, M.F., «Jet Characteristics of a Plunging Airfoil,» *AIAA Journal*, Vol 37, no. 12, 1999

APPENDICES

A. UDF code for pure-plunge motion

```
#include "udf.h"
#define   freq  5
#define   pi  3.1415926
#define   chord   0.064
#define   hoverc   0.4


DEFINE_CG_MOTION(Y05, dt, vel, omega, time, dtime)

{


        real v ;


        v           = 2*pi*freq*hoverc*chord*cos(2*pi*freq*time);


      vel[0] = 0.0;
```

```
    vel[1] = v;
    vel[2] = 0.0;


omega[0] = 0.0;
omega[1] = 0.0;
omega[2] = 0.
```